Zhaochuan Fan

Molecular Simulations of Nanoscale Transformations in Ionic Semiconductor Nanocrystals

Delft University of Technology

Molecular Simulations of Nanoscale Transformations in Ionic Semiconductor Nanocrystals

Proefschrift

ter verkrijging van de graad van doctor
aan de Technische Universiteit Delft,
op gezag van de Rector Magnificus prof. ir. K.C.A.M. Luyben,
voorzitter van het College voor Promoties,
in het openbaar te verdedigen op maandag, 11 januari, 2016 om 12:30 uur

door Zhaochuan Fan
Master of Science, Nankai University
geboren te Beijing, China.

Dit proefschrift is goedgekeurd door de promotoren:
Prof. Dr. Ir. T.J.H. Vlugt
Dr. Ir. M.A. van Huis

Samenstelling promotiecommissie:

Rector Magnificus	voorzitter
Prof. Dr. Ir. T.J.H. Vlugt	Promotor, Technische Universiteit Delft
Dr. Ir. M.A. van Huis	Co-Promotor, Universiteit Utrecht
Independent members:	
Prof. Dr. C. Dellago	University of Vienna
Prof. Dr. Ir. J.G.E.M. Fraaije	Universiteit Leiden
Prof. Dr. E.J.R Sudhölter	Technische Universiteit Delft
Prof. Dr. G.C.A.M. Janssen	Technische Universiteit Delft
Prof. Dr. H.W. Zandbergen	Technische Universiteit Delft

The research reported in this thesis was carried out with financial support by the Foundation for Fundamental Research on Matter (FOM), which is part of the Netherlands Organisation for Scientific Research (NWO). In addition, this work was supported by NWO Exacte Wetenschappen (Physical Sciences) for the use of supercomputing facilities, with financial support from the Nederlandse Organisatie voor Wetenschappelijk Onderzoek (Netherlands Organization for Scientific Research, NWO).

ISBN: 978-94-6186-574-8
Printed by CPI-Wöhrmann Print Service – Zutphen

> *The problems of chemistry and biology can be greatly helped if our ability to see what we are doing, and to do things on an atomic level, is ultimately developed – a development which I think cannot be avoided.*
>
> Richard P. Feynman

Contents

1 Introduction 1

1.1 Nanocrystals and Heteronanocrystals with Diverse Morphologies . . . 1

1.2 Molecular Simulation . . . 5

1.2.1 First Principles Density Functional Theory . . . 5

1.2.2 Molecular Dynamics . . . 6

1.3 Linking Molecular Dynamics simulations and HRTEM Experiments . . . 8

1.4 Scope and Outline of this Thesis . . . 13

2 Deriving Ab-Initio-Based Pair Potentials for ZnO Solid Systems 17

2.1 Introduction . . . 17

2.2 Derivation of Potentials . . . 21

2.2.1 Density Functional Theory Calculations . . . 21

2.2.2 Lattice Inversion Method . . . 22

2.2.3 Fitting Methodology . . . 26

2.3 Physical Properties of ZnO . . . 29

2.3.1 Lattice Parameters, Elastic Properties and Structural Stabilities . . . 29

2.3.2 Phonon Dispersion and DOS . . . 31

2.3.3 High-Temperature Simulations . . . 31

2.3.4 High-Pressure Simulations . . . 34

2.3.5 Surface Energy Calculations 38
2.4 Conclusions 40

3 Deriving a Transferable Force Field for CdS-CdSe-PbS-PbSe Solid Systems 43
3.1 Introduction 43
3.2 Methods 48
3.2.1 Density Functional Theory Calculations 48
3.2.2 Fitting Methodology 50
3.2.3 Molecular Dynamics Simulations 51
3.3 Physical Properties of CdS, CdSe, PbS, and PbSe 52
3.4 Physical Properties of Mixed Phases 61
3.5 Surface Energy Calculations 67
3.6 Conclusions 69

4 Thermally Induced Transformation of CdSe Nanocrystals 71
4.1 Introduction 71
4.2 Methods 73
4.2.1 Molecular Dynamics Simulation 73
4.2.2 Synthesis of CdSe Nanocrystals 74
4.2.3 TEM In-situ Heating Experiments 74
4.3 Results and Discussion 75
4.3.1 Sphere-to-Tetrapod Transformation 75
4.3.2 Atomic-Scale Transition Mechanism 80
4.3.3 Experimental HR-TEM Results 83
4.3.4 Temperature and Size Effects 85
4.4 Conclusions 88

5 Cation Exchange in CdSe-PbSe Nanodumbbells 91
5.1 Introduction 91
5.2 Methods 92
5.2.1 In Situ Transmission Electron Microscopy 92
5.2.2 Scanning Transmission Electron Microscopy Energy-Dispersive X-ray Spectroscopy Experiments 93

5.2.3 Molecular Dynamics Simulations 93
5.2.4 Density Functional Theory Calculations 93
5.3 Results 94
5.3.1 In Situ TEM and STEM EDS Experiments 94
5.3.2 MD Simulations and DFT Calculations 99
5.4 Discussion 101
5.5 Conclusions 103

6 Cation Exchange in PbS-CdS Nanocrystals 105
6.1 Introduction 105
6.2 Methods 108
6.2.1 Coarse-Grained Pseudoligand Model 108
6.2.2 Construction of Colloidal PbS and CdS NCs 110
6.2.3 Molecular Dynamics Simulation 111
6.2.4 Volume Scaled Exchange Rate 111
6.2.5 Root Mean Square Motion 112
6.2.6 PbS/CdS Interfacial Energy Calculations 112
6.2.7 Energy Barriers for Cation to Migrate at the PbS/CdS Interface 114
6.2.8 Simulations of CE at High-Temperature-High-Pressure Conditions 115
6.3 Results 115
6.3.1 Thermodynamic Driving Force 115
6.3.2 Self-Limiting Exchange 120
6.3.3 Kinetics: A Revised Vacancy-Mediated Mechanism . 122
6.4 Discussion 129
6.5 Conclusions 133

References 135

Summary 167

Samenvatting 171

Curriculum Vitae **175**

Publications by the Author **177**

Acknowledgement **179**

Chapter 1

Introduction

1.1 Nanocrystals and Heteronanocrystals with Diverse Morphologies

Nanotechnology, inspired by Feynman's lecture [1] 'There is plenty of room at the bottom', has rapidly developed as one of the most advanced topics in science and technology in the 21^{th} century. Nanostructured materials have been used by scientists in almost every research field in physics and chemistry, and are increasingly studied in geology, biology, and the health sciences as well. If materials have a size at the nanoscale ($1 \sim 100 \cdot 10^{-9}$ m), they can easily enter living organisms and can be used in drug delivery and bio-sensing [2]. Compared to macroscopic materials, nanosized materials usually have special size- or shape-dependent mechanical, optical, and electronic properties [3, 4]. Nanomaterials have been used in the development of superhard materials, solar cells, and high-performance electronic devices [3–6]. The large surface-to-volume ratio enhances surface properties of nanomaterials, enabling broad application of nanomaterials in surface catalysis, surface gas adsorption, and cation exchange process. [7–9]. Due to these special and novel properties of nanomaterials, it is not difficult to understand the scientists' enthusiasm for developing and improving high-yield fine-controlled synthesis and postsynthsis methods [10–12].

In this thesis, we focus on several II-VI and IV-VI semiconductors, including ZnO, CdS, CdSe, PbS, and PbSe. These materials are all ionic crystals and popular candidates for the synthesis and design of nanostructures. Here, we briefly introduce several most commonly used synthesis and postsynthesis methods for these semiconductor nanocrystals. The hot injection (HI) method [13] being capable of yielding nearly monodisperse particles, is one of the most efficient and well-known synthesis methods for metal, semiconductor, and oxide NCs. In a HI process, precursors containing cations and anions are injected into a reactor at high temperature [13] (see Figs. 1.1 a-b). The fast mixing and high reaction temperature enable instantaneous formation of nuclei which further grow at the expense of the excess cations and anions in solution [14]. The size, shape and crystal structure of the produced NCs can be controlled by the types of ligand and solvent, and the reaction temperature and reaction time [14] (see Figs. 1.1 f-g).

Seeded growth (SG) is similar to the HI method, whereby new layers of material grow on top of existing NCs (seeds) by a multi-injection process [15]. Since seeds are required in a SG experiment, the SG method is often combined with a HI process. The morphology of heteronanocrystals (HNCs) is controlled by the structure and morphology of the seed NCs [15, 17]. For example, Manthiram *et al.* [15] report that a CdSe/CdS dot-in-rod nanostructure is synthesized using CdSe seeds with the wurtzite (WZ) structure, while CdSe/CdS branched nanostructures are synthesized if the CdSe seed NCs have the zinc blende (ZB) structure. Using the SG method, a number of HNCs with novel morphologies can be successfully synthesized, including teardrop-like NCs (Fig. 1.1 h), dumbbell-like HNCs (Fig. 1.1 i), and multipod HNCs (Figs. 1.1 j-k).

Synthesized nanocrystals can also be used as building blocks and can be connected in a controlled manner [29]. This technique has been first named "oriented attachment" (OA) by Penn and Banfield [30]. Annealing is often used to remove the ligands on the NC surface and activate the OA process [29]. The preferential attachment is often determined by the size and shape of the NCs and the different surfaces as well as ligands [23, 31, 32]. Several novel 0-D (*e.g.*, Figs. 1.1 m, p), 1-D (*e.g.*, Figs. 1.1 l, o), and 2-D

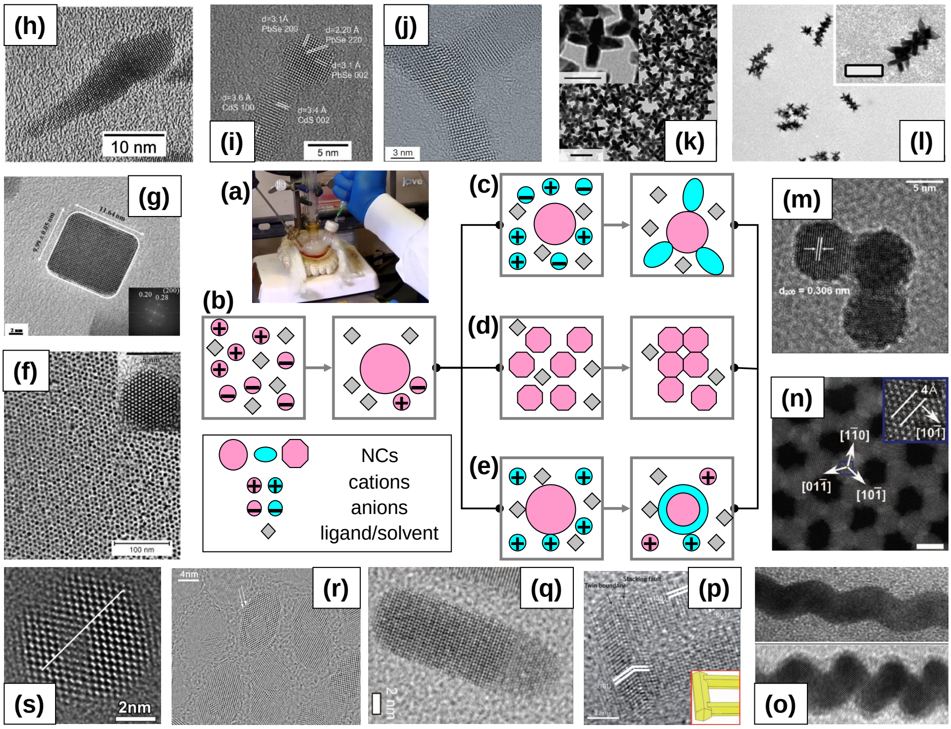
(h)
10 nm
d=3.1 Å PbSe 200
d=2.20 Å PbSe 220
d=3.1 Å PbSe 002
d=3.6 Å CdS 100
d=3.4 Å CdS 002
(i)
5 nm
(j)
3 nm
(k)
(l)
(g)
11.64 nm
9.99 ± 0.05 nm
0.20
0.28
(200)
2 nm
(a)
(b)
(c)
(d)
(e)
(m)
5 nm
d200 = 0.306 nm
(f)
5 nm
100 nm
(n)
4Å
[1$\bar{1}$0]
[10$\bar{1}$]
[01$\bar{1}$]
[10$\bar{1}$]
NCs
cations
anions
ligand/solvent
(s)
2nm
4nm
(r)
(q)
2 nm
Twin boundary
Stacking fault
(p)
2nm
(o)

Figure 1.1: (a) Illustration of a hot injection (HI) experiment, image adapted with permission from Ref. [15] (copyright MyJoVE Corporation 2013). (b-d) Schematic representation of synthesis and postsynthesis of nanostructures: (b) HI; (c) seeded growth (SG); (d) oriented attachment (OA); (e) cation exchange (CE). The black lines show the possible combinations of these methods. (f-s) TEM/HRTEM images of ionic nanocrystals with diverse morphology synthesized using these methods: (f) CdSe nanospheres (HI), image adapted with permission from Ref. [14] (copyright Wiley Online Library 2005); (g) A PbS nanocube (HI), image adapted with permission from Ref. [16] (copyright Royal Society of Chemistry 2012); (h) A CdSe teardrop (HI+SG), image adapted with permission from Ref. [17] (copyright American Chemical Society 2000); (i) A PbS/CdS nanodumbbell (HI+SG), image adapted with permission from Ref. [18] (copyright American Chemical Society 2005); (j) CdTe/CdSe tetrapod (HI+SG), image adapted with permission from Ref. [19] (copyright Nature Publishing Group 2004); (k) CdSe/CdS octapods (HI+CE+SG), image adapted with permission from Ref. [20] (copyright American Chemical Society 2010); (l) Interlocked octapods (HI+SG+OA), image adapted with permission from Ref. [21] (copyright American Chemical Society 2014); (m) Attached PbSe NCs (HI+OA), image adapted with permission from Ref. [22] (copyright Royal Society of Chemistry 2011); (n) Honeycomb superlattices (HI+OA+CE), image adapted with permission from Ref. [23] (copyright American Association for the Advancement of Science 2014); (o) Helical PbSe nanowires (HI+OA), image adapted with permission from Ref. [24] (copyright American Chemical Society 2005); (p) Nanorod couples (HI+OA+CE), image adapted with permission from Ref. [25] (copyright Nature Publishing Group 2014); (q) A CdS/Cu_2S binary rod (HI+SG+CE), image adapted with permission from Ref. [26] (copyright American Chemical Society 2009); (r) PbSe/CdSe dot-in-rod HNCs (HI+OA+CE), image adapted with permission from Ref. [27] (copyright American Chemical Society 2011); (s) A PbTe/CdTe core/shell HNC (HI+CE), image adapted with permission from Ref. [28] (copyright American Chemical Society 2009).

(*e.g.*, Fig. 1.1 n) nanosctructures can be synthesized using the OA method.

A third postsynthesis technique, besides the SG and OA methods, is cation exchange (CE) [33, 34]. In a CE process, cations in the nanocrystals are (partially) replaced by another type of cations from the surrounding solution or vapour [33–35]. Typical CE processes include the Pb→Cd exchange in PbE (E = S, Se, Te) NCs [27, 28, 36, 37], Cd→Zn exchange in CdE NCs [38], and Cd→Ag/Cu exchange in CdE NCs [9, 39–41]. The first two types of CE processes are relatively slow and require high temperatures to overcome the activation barriers, while the third type is relatively fast and takes place spontaneously under ambient conditions [33, 34, 42]. The morphologies and structures of the productive NCs/HNCs and the exchange mechanisms also vary among different CE processes. For example, PbE/CdE core-shell structures formed by Pb→Cd CE have sharp PbE/CdE boundaries [37], while CdE/ZnE core-shell structures formed by Cd→Zn CE have wide $Cd_xZn_{1-x}E$ mixed phase layers [38]. For Cd→Ag exchange, CE takes place from the sides of the CdE rods, whereas, in the Cd→Cu exchange, CE starts from the tips of the CdE rods [26]. CE is often combined with OA and SG to synthesize nanostructures with designed structures, shapes, and materials (see Figs. 1.1 q-s).

There are many experimental characterization techniques that can probe and measure the physical properties of the NCs. One of the most remarkable techniques is high resolution transmission electron microscopy (HRTEM) that enables direct observation of the nanocrystals at the atomic level [43] (see Figs. 1.1 f-s). The continuous development of TEM methodology prompts experimentalists to perform more sophisticated experiments. For example, the innovation of microelectronic mechanical system technology and low-drift heating holders enables the observation of phase transitions of NCs during *in situ* heating experiments [44]. For visualizing heteronanostructures, high-angle annular dark field scanning transmission electron microscopy (HAADF-STEM) enables one to distinguish different components in a HNC by Z contrast, which is based on the different atomic numbers of the constituent atoms [35]. The chemical composition of a NC in a particular domain can be quantitatively measured by chemical mapping energy-dispersive X-ray spectrometry (Chemi-STEM EDX) [35].

There are also limitations to HRTEM experiments. Due to the fast motion of atoms, the time resolution of HRTEM is not sufficiently high to trace individual atom, and although nanoscale transformations can be observed at the atomic level in HRTEM experiments, a fundamental understanding of the microscopic mechanisms is still missing. Molecular simulations are needed to obtain this understanding.

1.2 Molecular Simulation

1.2.1 First Principles Density Functional Theory

First principles calculations (also called ab initio calculations) is a method to investigate materials properties based on quantum mechanics. The term "first principles" indicates that no empirical parameters enter the calculations, and all physical properties can be calculated solely from information on atom types and positions. For a system consisting of many electrons and nuclei with many-body interactions, the state of the system can be described by the Schrödinger equation [45]:

$$H\Psi = E\Psi \tag{1.1}$$

where H is the Hamiltonian operator, Ψ is the wave function of the system and E is the energy of the system. Under the Born-Oppenheimer approximation [45], the Hamiltonian H can be further written as:

$$H = T + U_{\mathrm{ei}} + U_{\mathrm{ee}} \tag{1.2}$$

where T is the kinetic operator, U_{ei} is the interaction potential due to the nuclei, and U_{ee} is the electron-electron interaction operator. While it is very difficult to solve Eq. 1.1 directly, density functional theory (DFT) transforms the problem of solving full wave functions into solving the electron density function $\rho(r)$. It has been mathematically proven [46] that the physical properties of materials in their ground states are uniquely determined by the ground state electron density, and the density that minimises the total energy is the exact ground state density. In 1965, Kohn and Sham [47] devised a formalism, now called the Kohn-Sham equations, for carrying-out DFT calculations. In 1998, Kohn was awarded the Nobel Prize in Chemistry for his contribution to the Kohn–Sham equations and other work related to DFT [48]. For a detailed introduction and derivation of DFT, we refer to several classical review articles and textbooks [45, 49].

As mentioned, DFT can be adopted to calculate many physical properties including those that can be experimentally measured and those that cannot be obtained by experiments [50, 51]. An interesting and important example is the calculation of the effective atomic charges (charge density population analyses) in solid materials [52, 53]. Given the electron density of a material, "effective" charges of the ions can be calculated by integrating the electron cloud over space. However, there is no unique definition of the effective charges as different values of effective charges may be obtained by integrating electron density with different boundaries [54, 55]. The Bader charge analysis [56] (also called atoms in molecules, AIM) has a clear physical meaning. It defines the boundary of two atoms as the place where flux of the electron density perpendicular to the surface is zero, and the effective charge of an atom is the integration of the electron density within these surfaces [56].

The most significant advantages of DFT calculations are its reliability and versatility. However, its disadvantage is also obvious: the high computational cost. To date, DFT can deal with systems that contain up to roughly 1000 atoms [57, 58]. Only a few of the fastest computer facilitates in the world are able to perform DFT calculations on such a system [57, 58]. The longest time scale that can be reached in DFT-based MD simulations is also very short, typically a few tens of ps [59, 60]. Therefore, if we want to model a large system (*e.g.*, a NC containing 10,000 atoms) or to model a system for a long simulation time (*e.g.*, 100 ns), performing DFT calculations is currently not feasible.

1.2.2 Molecular Dynamics

Molecular Dynamics (MD) is a method to obtain a representative trajectory of a set of interacting particles by time integration of their equations of motions. The particles can be atoms, molecules or groups consisting atoms with fixed relative positions (rigid models), molecules with a reduced resolution (coarse-grained models), or macroscopic materials (*e.g.*, granular materials). For atomistic MD simulations, the interatomic interactions can also be treated at different levels: They can be expressed by empirical analytic functions (the force fields), or obtained by semi-empirical methods such as the tight-binding method (tight-binding Molecular Dynamics) and ab-initio DFT calculations (ab initio Molecular Dynamics (AIMD)). The equations of motions obey Newton's second law,

$$f_i = m_i a_i \tag{1.3}$$

where f_i is the force applied on atom or particle i; m_i and a_i are the mass and acceleration of atom i, respectively. The force on atom i can also be calculated by differentiating the potential surface U with respect to the coordinates of atom i, $f_i = -\partial U/\partial x$. The time evolution of the system can obtained by different time integration schemes, such as Verlet, velocity Verlet, or frog leap [61, 62].

When performing a MD simulation, an appropriate thermodynamic ensemble needs to be selected. A microcanonical NVE (the number of atoms (N), volume (V), and the total energy (E) of the system are conserved) ensemble is often used, since the energy is always conserved and there is no artificial thermodynamic operation in an NVE ensemble. However, the total energy of a system in the NVE ensemble is determined by the total energy of its initial configuration, therefore, the temperature and pressure of the system are difficult to control. For realistic systems, the pressure and temperature can be easily controlled. For this reason, the canonical (NVT) or isothermal–isobaric (NPT) ensembles are sometimes selected. The Nosé-Hoover thermostat [63] is one of the most frequently used methods to control the temperature, where one or more virtual heat baths are used to control the temperature of the system. This extended Lagrangian method does not affect the results of thermodynamic sampling, but may affect the dynamics of the system. The time evolution of a system will be affected by the period and amplitude of the coupling between the thermostat and the system. For a more detailed introduction and of MD simulations, we refer readers to classical textbooks [61, 62, 64–66].

Classical MD simulations can be used to investigate physical properties related to potential energy surfaces (*e.g.*, crystal structures, phase transitions, and diffusion), but not those related to electronic structures. Classical MD simulations with empirical force fields allow the investigation of large systems and at long time scales. An impressive example is a 425-ns MD simulation with an all-atom model for a HIV-1 virus capsid consisting of 13 million atoms to investigate its stability [67]. Considering the computational capacity of current computers, these large-sized and long-timescale simulations can only be carried out by classical molecular simulations with empirical force fields.

1.3 Linking Molecular Dynamics simulations and HRTEM Experiments

Molecular simulation provides the opportunity to obtain understanding of the mechanism underlying the nanoscale transformations of NCs observed in experiments, especially HRTEM experiments in which the transformations can be directly observed at the atomic level [31, 68]. For systems containing more than a few hundred of atoms or for physical processes having a time scale longer than a few hundreds of picoseconds, performing classical molecular simulations (MD or MC) with empirical force fields is more practical than performing DFT calculations or AIMD. However, accurately reproducing experimental observations by simulations is always difficult, whereby the results of both simulations and experiments are determined by many factors (*e.g.*, the choice of simulation method, the accuracy of the simulation, the techniques used in the experiment, the accuracy of the experimental measurements). Here, we use two examples to discuss the key factors linking MD simulations and HRTEM experiments.

In Ref. [69], Hu *et al.* investigated the crystallization process of ZnO NCs in liquids using MD simulations with a PCRIM model [70]. ZnO is a typical (wurtzite) WZ semiconductor. Like in other WZ materials, a wurtzite-to-rocksalt (WZ-to-RS) structure transition takes place in ZnO bulk materials at large external hydrostatic pressures [71]. For ZnO nanocyrstals, this phase transition requires a high transition pressure of about 15 GPa [72, 73]. However, Hu *et al.* [69] claimed that ZnO nanocrystals with the RS structure were found after recrystallization even at zero pressure conditions. These results clearly contradict the experimental observations that RS is not a stable phase for ZnO crystals under ambient pressures [71].

The reason of this unanticipated result can be traced back to the force field used by Hu *et al.* [69]: a transferable pairwise model [70] including a few tens of oxides and silicates. Apparently, this model focusses on transferability but not on accuracy for individual materials. During parameterization, the stability of the RS phase of ZnO was not included in the training set nor in the validation set [70]. We calculated the lattice energy of the WZ and RS phases of ZnO with this force field, and found that energy of the RS phase at zero pressure condition calculated with this force field is even lower than that of the WZ phase (simulation details can be found in Chapter 2 of this thesis). Therefore, it is not surprising that a WZ ZnO nanocrystal will transform to the RS structure only by heating in the MD simulations [69]. Here, we conclude that using an inappropriate force field may lead to erroneous and unphysical results.

In another example, Wang *et al.* [74] performed a virtual simulation experiment where a single ZnO nanowire was stretched until fracture. In these MD simulations, a novel body-centered-tetragonal (BCT) structure and a WZ-to-BCT structural transition have been observed before fracture [74]. This new structural transition and the BCT structure had not been experimentally observed in ZnO, and therefore this study has attracted the interests of theorists and experimentalists [57, 75–80]. Remarkably, stretching experiments [75] have been conducted on single ZnO nanowires together with large-scale DFT calculations [57] performed for ZnO nanowire models containing about 800 atoms. Unfortunately, the structural transition of Ref. [74] has neither been found in the experiments nor in the large-scaled DFT calculations [57, 75].

Do MD simulations truly predict a novel phase transition of ZnO nanowires or is the simulation result unphysical? In the original MD paper [74], DFT calculations have also been used to calculated the stability of the BCT phase. According to the DFT calculations, the relative energy of the BCT phase with respect to the WZ phase is 0.07 eV/f.u. [74]. The force field used in the MD simulations [81] overestimated the stability of the BCT phase of ZnO, whereby the relative energy calculated with the force field is about one tenth of the value found using DFT calculations [82]). However, the efforts on looking for the BCT structure in ZnO has not weakened. Morgan [78] has proven that, using DFT calculations, the BCT structure has a lower energy than the WZ structure and becomes the most stable structure in thin ZnO films. BCT domains have even been directly observed on the edges of ZnO nanoislands as observed by HRTEM [77]. An empirical force field is an approximation, so it cannot precisely reproduce all physical properties of materials. The inaccuracy of a force field leads to simulation results that deviate from reality. However, new findings from simulation are still very interesting. We sometimes need to tolerate some inaccuracy (but not the limitations) of a force field and focus on capturing the physics of the "new findings" from the simulations. First principles DFT calculations and experiments can be subsequently used to validate or amend the findings.

Classical molecular simulations are not first principles methods. The accuracy of the results directly depends on the "quality" of the empirical force fields. Unfortunately, there is no universal standard to evaluate the quality of the force fields. Very often, for the same material, different force fields may provide very different results because of the different aims, functional forms, and parameterization schemes used when they are developed. The capabilities as well as the limitations of a force field published in literature requires attention. Additional tests for a force field may be required before performing simulations.

Sometimes, there are no force fields developed for a particular system or the reported force fields in literature are not accurate enough in describing particular physical properties. In this case, one needs to develop a new force field. To develop an empirical force field [83], one should basically follow three steps: (1) choose an appropriate functional form; (2) obtain force field parameters by fitting to the training set (a training set is a set of data obtained by experiments and/or DFT calculations which is used to fit the force field to reproduce these properties); (3) test the model using validation set (a validation set is a set of data different from the training set to test the accuracy of the force field in reproducing other properties). Step 1 is crucial for a successful development of an empirical force field. Based on extensive previous development of force fields [84], the use of different functional forms is generally classified by the type of solid materials. For example, the shell model and the partial charge rigid ion model are often used for (partial) ionic crystals (*e.g.*, NaCl, ZnO, and CdSe) [85]; Models including many-body interactions such as Tersoff or SW potentials are often used for covalent crystals (*e.g.*, C, Si, and Ge) [86]; The embedded atom model (EAM) is often used for metals (*e.g.*, Au, Ag, and Cu) [87]. The choice of functional forms is not fixed, and some models with complex functional forms and higher degrees of freedom (*e.g.*, reactive force fields (ReaxFF) [88, 89]) can be used to describe different types of materials. However, parameterizing a complicated model such as ReaxFF will be much more difficult than parameterizing simple models with fewer parameters [90].

It is often stated that each term of the force fields should have a clear physical meaning [83, 91]. If terms in a force field have clear physical meanings, the number of parameters may be reduced and the fitting procedure could be easier. For example, Rabani [92] has developed a force field for CdSe solids. Despite the fact that the functional form of this force field [92] is quite simple (a long-range Coulombic term and a short-range Lennerd-Jones potential) and the number of the force field parameters is only five, this force field is able to reproduce several physical properties of CdSe, including the crystal structures, polymorphic stability, elastic properties, pressure-induced phase transitions, and vibrational properties [68, 92, 93]. Using the same functional form, Grünwald *et al.* [94] have extended the CdSe force field to a transferable force field including CdS and ZnS solids. Schapotschnikow *et al.* [31] has developed a new force field for PbSe solids. These force fields have similar accuracy and the success of these force fields is not surprising as their functional form captures the essential physics of ionic crystals (Coulombic interactions + repulsive short-ranged interactions). In addition, full integer charges in traditional models for ionic crystals [81, 91] are abandoned, and instead partial charges are used. This is particularly appropriate for materials like CdS, CdSe, ZnS, or PbSe which have a half-ionic-half-covalent nature [95]. It is not always necessary that each term in a force field has a physical meaning. The aim of deriving a force field is to find a set of functions that is able to reproduce the potential energy surface (more precisely, the gradient of the potential energy surface) of materials [96]. If this is the case, the force field should be able to describe many physical properties of the materials and predict the behaviours of the material under external perturbations, even if the functional form may has no physical meaning [96]. One of the examples is the well-known Lennard-Jones potential that has been widely used in describing the interatomic dipole-dipole and short-ranged repulsive interactions. The former interactions are theoretically based whereas the latter are purely empirical. Another interesting example is a Tersoff model developed for GaN [97]. One may question the choice of Tersoff model for GaN, which is a typical ionic crystal [98], as no charge and no Coulombic term is included. However, this force field is fairly accurate and has been widely used in the MD simulations for GaN materials [99–101]. This is because the carefully parameterized Tersoff model is able to reproduce the potential energy surface of GaN solid, and the effect of the Coulombic interactions is included in the total energy of the Tersoff model [97].

We now summarize our answer to the question of how to link MD simulations and HRTEM experiments, which is illustrated in Fig. 1.2. First, using classical MD simulations to investigate transformations in nanocrystals observed in HRTEM experiments is direct and efficient (see the lines linking classical MD simulations and HRTEM experiments in Fig. 1.2) since the size of the nanocrystal systems and the time scales that can be reached by classical MD simulation are a few orders of magnitudes larger than those in DFT calculations. Note that the time-scales on HRTEM experiments and MD simulations still often have a few orders difference, but the difference is much small than that between DFT and HRTEM. Sometimes the system size and the time scales in MD simulations can directly match those in atomic-resolution experiments [102]. As shown in Fig. 1.2, an accurate force field is the “bridge” linking the classical MD simulations and HRTEM

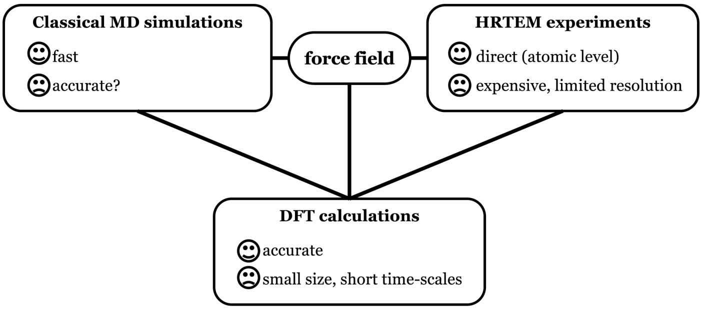
Classical MD simulations
☺ fast
☹ accurate?
force field
HRTEM experiments
☺ direct (atomic level)
☹ expensive, limited resolution
DFT calculations
☺ accurate
☹ small size, short time-scales

Figure 1.2: Flowchart showing the relation between the MD simulations, HRTEM experiments, and DFT calculations. The typical advantages (happy emoticons) and disadvantages (sad emoticons) of these methods for studying nanostructures are also listed.

experiments. Using accurate force fields is the prerequisite to obtaining meaningful simulation results, whereas less accurate or inappropriate force fields only lead to inaccurate or even unphysical simulation results. Second, to test or to derive a force field for moleculars simulations, first principles DFT calculations are needed to provide the information that can not be measured in experiments (the line linking DFT calculations and force field in Fig. 1.2). Finally, DFT calculations may also be used to validate and to further explain the phenomena found in classical MD simulations (the line linking DFT calculations and classical MD simulations in Fig. 1.2). In particular cases, DFT calculations can, obviously, be directly used in explaining the experiments (the line linking DFT calculations and HRTEM experiments in Fig. 1.2), however, this linkage is not in the scope of this thesis.

1.4 Scope and Outline of this Thesis

Although many methods and techniques have been developed for the syntheses of novel nanostructures, fundamental understanding of their microscopic mechanisms is still limited. Understanding of transformations of nanocrystals at the atomic level will improve synthesis methods and fine control of the nanocrystals with tailor-made structures and shapes. The aim of this thesis is to investigate structural and morphological transformations and cation exchange processes of nanocrystals using classical molecular simulations. Research questions are divided into the following subissues:

- How to appropriately choose a force field and perform molecular dynamics simulations, in order to reproduce transformations of nanocrystals observed in HRTEM experiments?
- How to develop (transferable) force fields with simple functional forms and adequate accuracy for ionic crystals for the simulations of transformations of nanostructures, with the aid of first principles DFT calculations?
- How to simplify ligand-solvent solutions of colloidal nanocrystals for molecular simulations of CE processes?

In Chapter 2, ZnO is taken as an example for the development of a force field for accurate simulations of phase transitions. We emphasize the accurate description of stability of several ZnO polymorphs and the phase transitions between them.. This is achieved with the aid of DFT calculations. The ZnO force field is developed using the partially charged rigid ion model approach. This model contains only eight parameters. It is able to accurately reproduce several physical properties of ZnO, including the crystal structures, elastic constants, phonon dispersion, polymorphic stability, phase transitions, and melting points. This new force field can be used in simulation studies of phase transitions of ZnO bulk and nanostructural materials.

Chapter 3 treats the development of a transferable force field for CdS-CdSe-PbS-PbSe solid systems. Similar to the work in Chapter 2, a number of DFT data is included in the training set during the fitting procedure, especially for the mixed phases which are not available from experimental data. MS_xSe_{1-x} (M = Cd or Pb) mixed phases simulated with the new force field show the formation of a solid solution while the $Cd_xPb_{1-x}E$ (E

= S or Se) mixed phases show phase separation. This force field is the first to date developed for CdS-CdSe-PbS-PbSe systems and will be used in molecular simulations of the CdE/PbE HNCs.

In Chapter 4, MD simulations are performed to investigate a morphological and structural transformation in CdSe NC upon heating. In MD simulations, a CdSe nanosphere with ZB structure is transformed to a tetrapod with four WZ legs attached to a tetrahedral ZB core. This nanoscale transformation of CdSe NCs has also been observed in HRTEM *in situ* heating experiments. Simulations reveal that the ZB-to-WZ structural transition is mediated by the vacancy formation and high mobility of the Cd atoms.

In Chapter 5, MD simulations are used to reveal the mechanism of a cation exchange process in PbSe/CdSe HNCs observed in HRTEM *in situ* heating experiments. In the experiments, PbSe/CdSe nanodumbbells (a CdSe nanorod with two PbSe tips) transform to PbSe nanodumbbells by a cation exchange process upon heating. MD simulations with our newly developed force field for CdS-CdSe-PbS-PbSe systems reveal that Cd-to-Pb cation exchange is initiated by the structural distortions near the CdSe/PbSe interface.

In Chapter 6, a coarse-grained psuedoligand model is introduced to study CE processes in colloidal PbS nanocrystals. MD simulations combined with a coarse-grained psuedoligand model and the all-atom CdS-PbS force field accurately reproduce the Pb-to-Cd cation exchange process in PbS NC-solution systems. It is shown that the exchange rate and the equilibrium can be controlled by the temperature and the type of ligands. The microscopic mechanism of the Pb-to-Cd cation exchange revealed by our MD simulations is consistent with the vacancy-mediated mechanism that was previously proposed in the literature.

Chapter 2

Deriving Ab-Initio-Based Pair Potentials for ZnO Solid Systems

This chapter is based on the paper: S. Wang, Z. Fan, R. S. Koster, C. Fang, M. A. van Huis, A. O. Yalcin, F. D. Tichelaar, H. W. Zandbergen, and T. J. H. Vlugt, 'New Ab Initio Based Pair Potential for Accurate Simulation of Phase Transitions in ZnO', J. Phys. Chem. C, 2014, ***118****, pp 11050–11061.*

2.1 Introduction

Zinc Oxide (ZnO) is an II-VI group semiconductor with a very wide range of applications, which covers the fields of rubber, ceramic and food industries, paint, pharmaceutics, and electronic devices [71, 103]. The first use of ZnO can be traced back thousands of years ago and elaborate studies on ZnO materials have been carried out for more than seven decades [71, 103]. In recent years, due to the development of the synthesis of low-dimensional ZnO and its potential application in optoelectronic devices [71, 103–107], the interest in ZnO has reached a new peak. In nature, ZnO is stable in the wurtzite (WZ) structure at ambient conditions. Many different methods have been developed to synthesize high-quality bulk and thin-film WZ-ZnO [108–110]. ZnO with the zinc blende (ZB) structure has a relatively higher cohesive energy compared to the WZ structure which is therefore energetically unfavorable at zero temperature and zero pressure conditions [111]. The synthesis of ZB-ZnO can be achieved by growing thin films on specific substrates [112, 113]. A pressure-induced wurtzite-to-rocksalt (WZ-to-RS) phase transition can be observed at a transition pressure of about 10 GPa [114–117]. A further RS-to-CsCl transition was predicted by DFT calculations at 260 GPa [111], which has not yet been observed in experiments. ZnO nanostructures can be synthesized with diverse morphologies, including nanoparticles and nanorods [118, 119], nanowires and nanobelts [120, 121], nanohelices [122], nanorings and nanotubes [123, 124], nanomultipods and nanoflowers [125–127]. The diversity of the ZnO nanostructures enables the potential application of ZnO materials in transparent electronics, photodetecters, and solar cells, and for nanomotion and biosensing [105–107, 128].

Theoretical studies on ZnO have been mainly first-principles calculations [57, 74, 78–80, 111, 117, 129–142] and molecular simulations using empirical or semi-empirical potentials [74–76, 143–156]. Density Functional Theory (DFT) calculations have been widely used for the studies of the physical properties of ZnO, including the crystal structures and mechanical properties [111, 129, 130], electronic structure [131, 132], vibrational properties [117, 133–135], structural stability and phase transitions [78–80, 111, 129, 133, 136–142]. Although proven to be accurate, DFT calculations were often restricted to static calculations and to small systems containing few atoms. Moreover, temperature effects were usually treated within the quasi-harmonic approximation, whereby anharmonicities were neglected. Alternatively, using classical force fields, not only many physical properties can be studied easily by lattice statics (LS) and lattice dynamics (LD) simulations, but also temperature effects with full consideration of anharmonicities, and larger systems such as nanostructures consisting of thousands or even a few million atoms [156] can be studied by Molecular Dynamics (MD) or Monte Carlo (MC) simulations. However, the accuracies of MD or MC simulations directly depend on the accuracy of the potentials used.

There have been several attempts to develop interaction potentials for ZnO, including shell models (SM) by Lewis and Catlow [91] and by Binks *et al.* [81], an analytic bond-order potential (ABOP) by Erhart *et al.* [157], and a reactive force field (ReaxFF) by Raymand *et al.* [88, 147]. The SM derived by Binks *et al.* [81] is one of the most frequently used potential models for ZnO. This potential set reproduces several physical properties of ZnO in the WZ, ZB and RS structures with considerable accuracy. Unfortunately, it fails to precisely reproduce the stabilities of the intermediate states in the WZ-to-RS phase transition and the phonon dispersion curves of WZ-ZnO. The SM derived by Lewis and Catlow [91] yields a transition pressure of 3.7 GPa for the WZ-to-RS phase transition, which differs from the experimental one by about 60%. In 2002 and 2008, the same research group proposed a more complicated SM [153] for ZnO with piecewise functions and a modified version [154]. These new SMs accurately predicts several physical properties of ZnO in multi-structures [155] as well as the stable and metastable structures of $(\mathrm{ZnO})_\mathrm{n}$ (n=1-32) clusters [154]. These SMs contain more than 30 parameters, whose functional forms are complex. Potentials with a very complex functional form may suffer from difficult and turbulent fitting procedures in derivations and possible inefficiency in applications. Similar problem also exists in the ABOP [157] (37 parameters) and the ReaxFF [88] (93 parameters) for ZnO. Therefore, to develop a novel interatomic potential model for ZnO which has a simple functional form, is accurate and computationally efficient is important for simulation studies of ZnO and its related materials.

The traditional procedure to develop empirical potentials is that the type of the potential is chosen first, and subsequently the parameters are obtained by directly fitting to experimental data [83]. The potentials derived in this way obviously match some of the experimental results, but are likely to be inaccurate in describing the physical properties of other high-pressure, metastable, or intermediate phases. Although many physical properties of these non-stable phases can be obtained by DFT calculations that can be used for fitting the potentials, the correctness of the potentials derived is not guaranteed directly from the first principles calculations, since the parameters of potentials with respect to the same set of data are non-unique. In contrast to any of the fitting procedures, the lattice inversion (LI) method proposed by Chen [158] directly extracts the information on the interatomic interactions from the first principles calculations. By building multiplicative semigroups and using Möbius inversion, the LI derives the interatomic potentials in crystals from the energy-lattice ($E-a$) curves calculated by DFT. The LI method has been successfully applied to the development of interaction potentials for metals [159], rare earth elements [160], alkali halides [161], and semiconductors [162]. The functional forms of the potentials do not need to be preselected in the LI method but are chosen based on the shapes of the inverted potential curves. Therefore, the potentials derived by LI method incorporate intrinsic accuracy from first principles. However, the LI method has its own limitations. Because three-body and many-body interactions are not taken into consideration, and due to approximations made in the first-principles calculations, some physical properties calculated by the potentials directly derived by the LI method have a relatively large deviation with respect to experimental results.

We combine the LI method with an empirical and ab-initio energy surface fitting procedure, and we developed a set of interatomic pair potentials for ZnO within the Partially Charged Rigid Ion Model [163] (PCRIM) approach. We first used DFT calculations and the LI method to choose appropriate functional forms of the potentials to describe different interatomic interactions and to obtain the parameters. The parameter set was used as an initial guess in the next empirical and energy surfaces fitting procedure. The parameters for the ZnO potential model were adjusted by fitting them to reproduce the lattice parameters and relative energies of ZnO in the WZ, ZB, RS and honeycomb (HC) structures as well as the elastic constants of WZ-ZnO. The potential model with the adjusted parameter set was examined by comparing with the initial guess to avoid any significant change after fitting. In this way, the correctness of the potential model is guaranteed by first-principles calculations and the precision of the potential model is adjusted by fitting to experimental and DFT data. Our new ZnO potential model was validated by its ability to reproduce a variety of physical properties of ZnO in various structures. The ”validation” set includes lattice parameters and structural stabilities of ZnO in the cesium chloride (CsCl) and the body-centered tetragonal (BCT) structures, high-temperature and high-pressure measurements, vibrational properties and surface energies of WZ-ZnO. Our ZnO potential model only contains 8 parameters and can be used in most of the current MD or MC codes. The shortcomings of the ZnO potentials are also discussed to ensure appropriate use in the future.

2.2 Derivation of Potentials

2.2.1 Density Functional Theory Calculations

First principles density functional theory calculations were performed using the VASP code [164]. Within the projected augmented wave (PAW) method [165] the generalized gradient approximation (GGA) functionals by Perdew, Burke and Ernzerhof [166] (PBE) were used. The cut-off energy was set to a relatively high value of 600.0 eV, while the cut-off of the augmentation waves was set to 900.0 eV. Calculations were performed for six phases: WZ, RS, ZB, HC, CsCl and BCT crystal structures. For the conventional unit cells of RS and ZB, a Monkhorst Pack k-mesh [167] of $24 \times 24 \times 24$, was used, while for the CsCl and BCT structures k-meshes of $40 \times 40 \times 40$ and $21 \times 21 \times 35$ were used, respectively. For the hexagonal WZ and HC structures, gamma centered k-point meshes of $30 \times 30 \times 26$ and $30 \times 30 \times 30$ respectively were used. A scan over cut off energies and k-point meshes show that the results are well converged within 0.5 meV/atom.

Bader charge analysis [56] unambiguously defines the effective charges on the atoms. Hereby the boundary between two atoms is defined by the surface at which the derivative of the charge density is equal to zero. The charge in the volume enclosed by that surface then determines the charge of the atoms. For this method the Bader Charge Analysis code written by Arnaldsson *et al.* [168–170] was used. The results shows that the Bader charges on the Zn atoms in the WZ, RS, ZB, HC, CsCl and BCT structures are 1.22, 1.26, 1.23, 1.22, 1.12 and 1.22 electrons, respectively. Differences between the Bader charges of different structures are small, in particular between the ZB, WZ, HC and BCT phases, which is in the line of expectation since ZB, HC and BCT phases are structurally closely related to the WZ phase.

2.2.2 Lattice Inversion Method

The LI method has been described in detail in Refs. [158, 161], here we only briefly present the essential steps of the LI method. Assuming that the interatomic interactions in a system contains only pair-body interaction, the total energy can be expressed as the sum of the pair potentials, $\varphi(x)$:

$$E(x) = \frac{1}{2}\sum_{n=1}^{\infty} r_0(n)\varphi(b_0(n)x) \tag{2.1}$$

Where x is the nearest-neighbor atomic distance, $r_0(n)$ is the coordination number and $b_0(n)x$ is the atomic distance of the n^{th} neighbor. To solve the Eq. 6.1, a multiplicative semigroup $\{b(n)\}$ needs to be extended from the unclosed group $\{b_0(n)\}$ by multiplying any two elements in $\{b_0(n)\}$. Then Eq. 6.1 can be rewritten as:

$$E(x) = \frac{1}{2}\sum_{n=1}^{\infty} r(n)\varphi(b(n)x) \tag{2.2}$$

Where

$$r(n) = \begin{cases} r_0(b_0^{-1}(b(n)), & (b(n) \in b_o(n)) \\ 0, & (b(n) \notin b_o(n)) \end{cases} \tag{2.3}$$

Using the Möbius transformation [158], $\varphi(x)$ can be derived as:

$$\varphi(x) = 2\sum_{n=1}^{\infty} I(n)E(b(n)x) \tag{2.4}$$

Where $I(n)$ is the inversion coefficient which is uniquely determined by the crystal geometrical structure.

Three structures (ZB, RS, and PbO-B10) were chosen to perform the total energy DFT calculations for ZnO. The lattice constant a varied from 3.0 to 12.0 Å. In this work, the PCRIM [163] was used to describe the atomic interactions in ZnO. The PCRIM is one of the simplest models in materials computation which has had great success in the computational studies of binary semiconductors [31, 92, 94, 171]. In this model, the interatomic interaction only contains Coulombic interactions and short-range two-body interactions. The effective charges were initially selected as 1.2 e for our ZnO model based on the Bader analysis. Once the effective charge had been determined, we used Eq. S5-2.4 to invert the short-range pair potentials, $\phi(r_{ij})$. In the RS and ZB structures, both the cation and the anion sublattices are face-centered cubic. The cation sublattice and the anion sublattice have a relative displacement along the body diagonal of (0.5,0.5,0.5)a in the RS structure, and of (0.25,0.25,0.25)a in the ZB structure, where a is the lattice parameter of the conventional unit cell. The energy difference between the ZB and RS structures with the same lattice parameters only contains information about the Zn-O interaction. The cation sublattice in PbO-B10 structure is the same as that in the ZB structure (fcc). The relative displacements of the nearest neighbor cations and anions are the same in PbO-B10 and ZB structures ($a/4$). Therefore, the energy difference between ZB and PbO-B10 only originates from the difference in the anion-anion interactions in these two structures. The short-range interactions in ZnO can be obtained as follows:

$$\Delta E^{\mathrm{RS-ZB}}_{\mathrm{short-range}} = (E^{\mathrm{RS}}_{\mathrm{total}} - E^{\mathrm{RS}}_{\mathrm{Coul}}) - (E^{\mathrm{ZB}}_{\mathrm{total}} - E^{\mathrm{ZB}}_{\mathrm{Coul}}) \Rightarrow \phi_{+-}(r_{ij}), \quad (2.5)$$

$$\Delta E^{\mathrm{ZB-PbO}}_{\mathrm{short-range}} = (E^{\mathrm{ZB}}_{\mathrm{total}} - E^{\mathrm{ZB}}_{\mathrm{Coul}}) - (E^{\mathrm{PbO}}_{\mathrm{total}} - E^{\mathrm{PbO}}_{\mathrm{Coul}}) \Rightarrow \phi_{--}(r_{ij}), \quad (2.6)$$

$$\Delta E^{\mathrm{ZB}}_{\mathrm{short-range}} = E^{\mathrm{ZB}}_{\mathrm{total}} - E^{\mathrm{ZB}}_{\mathrm{Coul}} - E^{\mathrm{ZB}}_{+-} - E^{\mathrm{ZB}}_{--} \Rightarrow \phi_{++}(r_{ij}). \quad (2.7)$$

Where the subscripts, $+-$, $--$ and $++$ represent the cation-anion, anion-anion and cation-cation interactions, respectively. E_{total} is the total energy,

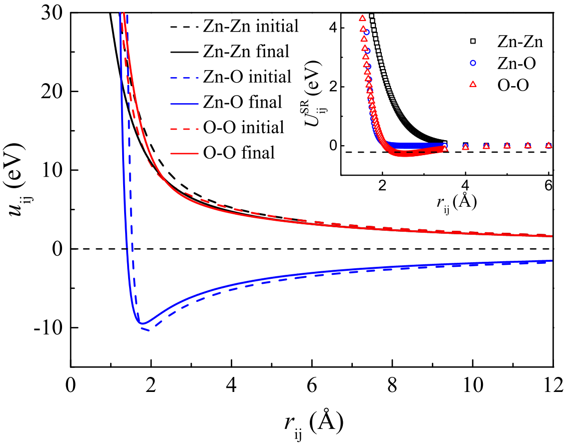

Figure 2.1: Interatomic pair potentials for ZnO. The dashed lines correspond to parameters obtained by the LI method (the initial guess), and the solid lines correspond to the parameters after fitting (final parameters). The upper-right inset shows the inverted short-range potential curves. The inverted Zn-Zn short-range potential curve is shifted 3.0 eV downwards here.

and E_{coul} is the electrostatic energy (Madelung energy). Details of the derivation can be found in Ref [162].

According to Eq. 2.5-2.7, the lattice energy of ZB-ZnO calculated by the potential model should be consistent with the total energy of ZB-ZnO by DFT calculations. However, we chose a very simple PCRIM to describe the interatomic two-body interactions in ZnO. In ZnO solids, bonding is largely ionic and the electrostatic interaction is dominant. Although reliable and accurate Bader analysis was used to determine the values of the effect charge, screening of the electrostatic interaction was omitted and the electron clouds were simplified as point charges in our potential model. These simplifications caused relatively large absolute values of the lattice energies of ZnO solids calculated by this model in comparison to that of the total energies by DFT calculations. The Zn-Zn short-range interaction potential curve derived from Eq. 2.7 needs to be shifted 3.0 eV downwards in order to make it converged to zero at large interatomic distances. This potential model is not able to duplicate the absolute locations of the $E_{\text{total}} - a$ (or $E_{\text{cohesive}} - a$, with a clearer physical meaning) curves in the coordinate. Compared to the DFT calculations, the $E - a$ curves calculated by the potential model have shifts to lower energies, which is essentially caused by the choice of the PCRIM that the ions remain charged as being pulled apart from each others. In consequence, some of the physical properties, *e.g.*, the thermal expansion coefficient, and ZnO in gas phase may not be properly described by the potential model. However, in this work, we aimed to develop a simple model to describe the condensed phases of ZnO. Many physical properties of the condensed phases are determined by the shapes of the $E - a$ curves near the equilibrium interatomic distances, and that of ZnO polymorphs can be correctly described by this potential model which was derived by the LI method.

The upper-right inset in Fig. 2.1 shows the data points of the inverted short-range interactions in ZnO. According to the inverted data points, the non-Coulombic interactions between Zn-O and Zn-Zn are mostly repulsive. Therefore, the potential in the Born-Mayer model [172] was chosen to describe the short-range Zn-O and Zn-Zn interactions:

$$u_{ij} = Ae^{-r_{ij}/\rho} \tag{2.8}$$

The inverted data points of O-O non-Coulombic interaction shows a minimum at the atomic distance of 2.53 Å. The Morse type potential [173] was chosen to describe the short-range O-O interaction:

$$u_{ij} = A[(1 - e^{-C(r_{ij}-\rho)})^2 - 1)] \tag{2.9}$$

All eight potential parameters were listed in Table 2.1. A cut-off radius of 12.0 Å was set for all short-range non-Coulombic interactions, and the Ewald method [61, 174] was used to calculate the long-range Coulombic interactions in both real and reciprocal space.

Before any further improvement was carried out to the parameter set, we had checked the quality of the current version that was directly derived by the LI method. Several physical properties of ZnO polymorphs were

Table 2.1: Parameters of the potentials for ZnO from the LI method (initial guess) and after applying the fitting procedures (final parameters). A is in eV; ρ is in Å; C is in Å^{-1}; and the effective charge, q, is in e.

	short-range interactions					effective charge
	interaction	type	A	ρ	C	q
initial guess	Zn-Zn	Born-Mayer[a]	111.6	0.5372		±1.2
	Zn-O	Born-Mayer[a]	7995000	0.1114		
	O-O	Morse[b]	0.2885	2.529	1.584	
final parameters	Zn-Zn	Born-Mayer[a]	78.91	0.5177		±1.14
	Zn-O	Born-Mayer[a]	257600	0.1396		
	O-O	Morse[b]	0.1567	3.405	1.164	

[a] Eq. 2.8; [b] Eq. 2.9.

calculated by the potential model with parameters derived by the LI method and were listed in Table 2.2 in braces. The current parameter set, which would be used as an initial guess in the fitting procedure, was already able to accurately reproduce the lattice parameters of WZ-, ZB-, and BCT-ZnO, elastic properties of WZ-ZnO, and relative stabilities of the WZ, ZB, and RS phases. However, the equilibrated lattice parameter of RS-ZnO and the relative stability of the HC phase could not be accurately reproduced by the current parameter set. Although the lattice parameters of the BCT-ZnO could be quite accurately reproduced, the calculated stability of the BCT phase was even slightly higher than the WZ phase, which was unreasonable and about to be improved.

2.2.3 Fitting Methodology

The 8-parameter PCRIM obtained from the LI was used as an initial guess in the fitting procedures described below. Since the initial guess from the LI method is considerably reliable, only the relaxed fitting procedure [83] was used to further adjust the parameters. Compared to the conventional fitting procedure, the relaxed fitting procedure is computationally more expensive but a higher quality of fitting is achieved. In the relaxed fitting procedure, the error was defined as the squared residual of the physical properties of the optimized configurations. Empirical fitting based on experimental data and ab-initio energy surface fitting based on DFT data were combined and carried out simultaneously in our fitting procedure. The schemes in the ab-initio energy surface fitting used in this work was slightly different from the conventional ones. Four ZnO polymorphs (WZ, ZB, RS, and HC) were chose as energy surfaces and the relaxed fitting was used. All eight parameters obtained from the LI method, including the effective charge, were set as parameters and were adjusted by fitting the experimental data and the DFT data. The experimental data include the lattice parameters of WZ-ZnO measured by neutron diffractometer at 20 K [175] and the WZ elastic constants measured at 4 K [176]. The DFT data for the ab-initio energy surface fitting include the lattice parameters of the ZnO in the ZB, RS and HC structures and the energy differences of ZnO in these structures with respect to WZ. It is generally known that DFT-GGA calculations systemically show larger lattice parameters in comparison to experimental data. The lattice parameters of ZB-, RS- and HC- ZnO from our DFT-GGA calculations were normalized by rescaling their volumes. The scale factor used for the rescaling was the ratio of the volume of WZ-ZnO from our DFT-GGA calculation over that of the experimental result [175]. The ratio c/a from our DFT calculations remained unchanged. Besides the structures used in the fitting procedure, the lattice parameters of other structures (the CsCl and BCT structures) from our DFT calculations were also normalized for validation. These normalized lattice parameters are listed in Table 2.2 in square brackets and the data used in the fitting procedures are listed in Table 2.2 in bold. All calculations in the fitting procedures were carried out by GULP [177].

Table 2.2: Physical properties of ZnO[a] calculated by LS and MD simulations, compared with experimental data, the shell model (SM), the analytic bond-order potential (ABOP), the reactive force field (ReaxFF), and DFT calculations. Lattice parameters a and c are in Å; u is the internal coordinate; the elastic constant c_{ij} and bulk modulus B are in GPa; energy difference ΔE is in eV/f.u.. The values in parentheses are experimental or MD results at 300 K; the values in square brackets are normalized lattice parameters from DFT calculations (see main text); The values in braces are calculated by the initial guess (unmodified parameters); the values in bold are data used for the fit.

	Expt.[a]	Force Fields				Ab-Initio Calculations	
		PCRIM, this work	SM[b]	ABOP[c]	ReaxFF[d]	this work	literature[e]
wurtzite, Space group $P6_3mc$ (No. 186)							
a	**3.242** (3.250)	{3.254} 3.238 (3.252)	3.271	3.219	3.29	3.287	3.199, 3.292
c	**5.188** (5.204)	{5.175} 5.176 (5.197)	5.138	5.257	5.3	5.306	5.162, 5.292
u	**0.3819**	{0.3823} 0.3814	0.3893	0.375	-	0.3790	0.3790, 0.3802
c_{11}	**222.6** (207)	{237.7} 221.2	232.5	212	222.9	185.8	226
c_{12}	**132.1** (117.7)	{140.8} 119.8	95.2	116	116.3	107.8	139
c_{13}	**122.0** (106.1)	{119.2} 97.2	85.6	109	103.5	94.2	123
c_{33}	**236.8** (209.5)	{221.3} 222.8	210.5	219	212.8	199.7	242
c_{44}	**47.5** (44.8)	{49.5} 51.2	74.6	43	57.1	36.5	40
B	(136-183)	{160.8} 143.5	133.7	144	144	129.3	162.3, 133.7
zinc blende, Space group $F\bar{4}3m$ (No. 216)							
a	(4.47, 4.595)	{4.564} 4.548	4.567	4.552	4.62	4.629 [**4.552**]	4.509, 4.633
ΔE_{ZB-WZ}	-	{0.038} 0.034	0.09	0	0.042	**0.014**	0.015, 0.013
rock salt, Space group $Fm\bar{3}m$ (No. 225)							
a	(4.271, 4.280)	{4.186} 4.262	4.32	4.275	4.44	4.337 [**4.265**]	4.229, 4.345
ΔE_{RS-WZ}	-	{0.331} 0.306	0.283	0.237	0.335	**0.294**	0.158, 0.237
cesium chloride, Space group $Pm\bar{3}m$ (No. 221)							
a	-	{2.605} 2.691	2.662	2.642	2.64	2.691 [2.646]	2.624, 2.705
$\Delta E_{CsCl-WZ}$	-	{1.763} 1.816	1.92	0.976	1.63	1.434	1.307, 1.358
honeycomb, Space group $P6_3/mmc$ (No. 194)							
a	-	{3.484} 3.404	3.393	-	-	3.465 [**3.407**]	-
c	-	{4.117} 4.489	4.634	-	-	4.580 [**4.504**]	-
ΔE_{HC-WZ}	-	{0.084} 0.165	0.091	-	-	**0.138**	0.16
body-centered tetragonal, Space group $P4_2/mnm$ (No. 136)							
a	-	{5.541} 5.482	5.539	-	-	5.624 [5.531]	5.48
c	-	{3.234} 3.256	3.232	-	-	3.285 [3.231]	3.17
u	-	{0.316} 0.320	0.317	-	-	0.319	-
ΔE_{BCT-WZ}	-	{-0.013} 0.056	0.007	-	-	0.048	0.074

[a] Experimental data measured at low temperature: WZ structure at 20 K reported in Ref. [175]; WZ elastic constants at 4 K reported in Ref. [176]. Experimental data measured at room temperature (in parentheses): Ref. [112–117, 175, 176]; [b] Calculated by LS simulations using the SM reported in Ref. [81]; [c] Ref. [157]; [d] Ref. [88]; [e] Ref. [74, 79, 111, 130].

The final parameters are listed in Table 2.1. Lastly, we checked if the potential model with the adjusted parameters did significantly change from those derived by the LI method. The potentials of different interatomic interactions as function of interatomic distance are plotted in Fig. 2.1 for both the parameters obtained from the LI method, and those adjusted by the fitting. The shapes of the potential curves calculated by the two parameter sets were similar. Comparing the physical properties calculated by the two parameter sets (see Table 2.2), no significant change was found, only the aforementioned deficiencies of the initial guess were improved. Obviously, only minor modifications were applied to the potentials by the fitting procedure. The potentials with adjusted parameters is very similar to the initial guess from the LI method. Therefore, the intrinsic correctness of the ab-initio calculations is retained.

2.3 Physical Properties of ZnO

2.3.1 Lattice Parameters, Elastic Properties and Structural Stabilities

The most basic requirement for a potential model is that it should accurately reproduce lattice parameters and elastic properties of the materials that are stable in nature. The elastic properties, including elastic constants and bulk modulus, are related to first-order derivatives of the total free energy with respect to atomic displacements. A potential model should also show considerable accuracy of its description of the high-pressure, meta-stable, or transition phases, in order to ensure that related phase transitions and the mechanism are described accurately as well.

We now verify our ZnO potential model by reproducing several physical properties of ZnO in different crystal structures. The physical properties of ZnO in the CsCl and BCT structures are in the ”validation” set, as those data was not used in the fitting procedure. Physical properties of ZnO at 0 K were calculated by lattice statics (LS) simulations and physical properties of ZnO at finite temperatures were obtained by MD simulations. LS and MD simulations were performed by GULP [177] and LAMMPS [178] codes, respectively. In the MD simulations, a periodic WZ-ZnO matrix containing 4312 atoms is constructed based on the experimental lattice parameters. The equations of motion are integrated using the velocity

Verlet algorithm with a time step of 1 fs. At 300 K and zero pressure, a MD simulation of 0.5 ns was performed on WZ-ZnO in the Isobaric-Isothermal (NPT) ensemble, out of which the first 0.1 ns was used for equilibration. The velocities were rescaled to the target temperature during the equilibration. The temperature and the pressure were controlled by a standard Nosé-Hoover thermostat and barostat [63]. The results from the LS simulations at 0 K and MD simulations at 300 K are listed in Table 2.2, together with available experimental data, DFT calculations and the results calculated using other potentials. In our DFT calculations, the elastic constants were calculated by applying small strains to the unit cell [179]. As with all other DFT calculations in this work, the GGA approach was used, which is known to underestimate the elastic constants. When comparing with the experimental data, it is clear that our potential model is able to accurately reproduce the crystal structure and the elastic properties of WZ-ZnO. The result of our MD simulation at 300 K indicates a volume of the ZnO unit cell of 47.60 Å^3, a ratio of c/a of 1.598, and a u of 0.3814, while the experimental values [175] are 47.63 Å^3, 1.602 and 0.3819, respectively. For the other phases, because they are not stable in nature, the only possible comparison is with DFT calculations. Special emphases should be placed on the relative stabilities of two phases: HC and BCT. HC is a possible intermediate phase in the pressure-induced WZ-to-RS phase transition [136, 143], and the BCT structure, which has been directly observed by HRTEM in ZnO nanoislands recently [77], is predicted to be stable under mild negative pressure [74, 80, 137]. The lattice parameters of all the high-pressure, meta-stable or unstable structures in equilibrium calculated by the potential model have good agreement with the normalized DFT results. The potential model also reproduces the correct order of the stabilities of bulk ZnO in the six structures studied: $E_{\mathrm{WZ}} < E_{\mathrm{ZB}} < E_{\mathrm{BCT}} < E_{\mathrm{HC}} < E_{\mathrm{RS}} < E_{\mathrm{CsCl}}$. The calculated lattice energy differences of the ZB, RS, HC and BCT structures with respect to the WZ structure are in good agreement with DFT calculations (see Table 2.2). In general, our PCRIM shows higher accuracy of reproducing the lattice parameters and relative stabilities of ZnO in comparison with other empirical or semi-empirical potential models [81, 88, 91, 155, 157]. Only the stability of the CsCl structure is underestimated by the potential model (1.816 eV/f.u.) compared to DFT calculations ($\sim$1.4 eV/f.u.). However, the inaccurately described stability of the CsCl structure also exists in other ZnO potentials [81, 88, 91, 155, 157].

2.3.2 Phonon Dispersion and DOS

In order to further test the validity and accuracy of our ZnO potential, we have calculated the vibrational properties of WZ-ZnO. WZ-ZnO belongs to the space group $P6_3mc$ (C_{6v}^4). Four atoms in the primitive cell have 12 degrees of freedom, and those at the Brillouin zone center (Γ) can be classified by group theory as $2A_1 + 2B_1 + 2E_1 + 2E_2$, including 3 acoustic modes $E_1 + A_1$. In all of the optical modes, A_1 and E_2 modes are both Raman and infrared active, E_2 modes are Raman active only, and the B_1 modes are silent modes. Figure. 2.2 shows the calculated phonon dispersion curves in the directions of $\Gamma \rightarrow$A and $\Gamma \rightarrow$M and the normalized partial phonon density of state (DOS). The calculated phonon dispersion curves are in excellent agreement with the DFT, inelastic neutron scattering and Raman data [134, 135]. Note that the ABOP [157] for ZnO whose functional form does not include the long-range Coulombic interactions is not able to describe the splitting of the longitudinal and transverse modes (LO-TO splitting). Our calculated partial phonon DOS also shows similar results as previous DFT calculations [133]. The partial phonon DOS indicates that the Zn atoms contribute mostly in the low frequency phonons and the O atoms contribute mostly in the high-frequency vibration.

2.3.3 High-Temperature Simulations

Using the same periodic WZ-ZnO model as in the previous MD simulation at 300K, a direct heating MD simulation was performed in NPT ensemble to test the thermal expansion and melting point for WZ-ZnO. Here, a relatively short time step of 0.5 fs was used. First, the system was equilibrated at 300 K for 1 ns, then the temperature was elevated by 10 K in every 5 ps, from 300 K to 3300 K. During heating, the Nosé-Hoover thermostat [63] was used to

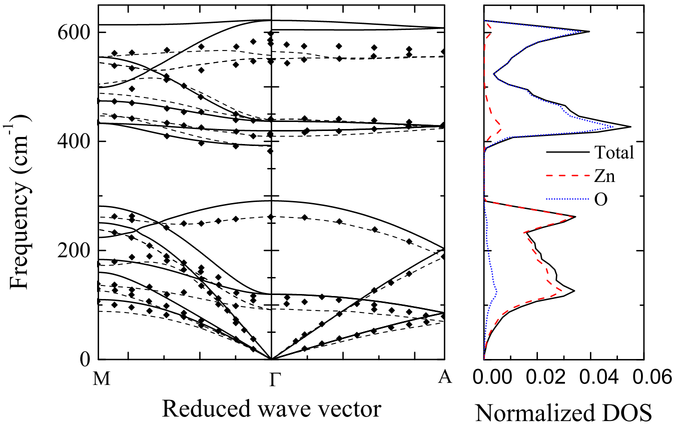

Figure 2.2: Phonon dispersion (left, solid lines) of WZ-ZnO along Γ-A and Γ-M directions and normalized partial phonon DOS (right) calculated by LD. The experimental data (diamonds) and DFT data (dashed lines) is extracted from Ref. [134].

control the temperature of the system. In Fig. 2.3 a, the lattice parameters a and c and the ratio c/a are displayed as a function of temperature. In comparison to experimental results [180], the linear thermal expansion coefficient obtained from MD simulations is overestimated by a factor of about three. Nonetheless, our MD simulations show correct trends in the changes of a, c and c/a with increasing temperature. The relative error of the lattice parameters from MD simulations is less than 1% compared with experimental data [180] in the temperature range of 300-1400 K. The melting point from the direct MD simulation was ~2680 K (see Fig. 2.3 b), which is higher than that of experimental value [181] of 2242 K. This superheating phenomenon was caused by the finite size effects and the limited simulation time in MD simulations.

In order to obtain a more accurate melting point for WZ-ZnO from MD simulations, the two-phase method [182] was performed with our ZnO potential model. A simulation box was constructed as a cuboid

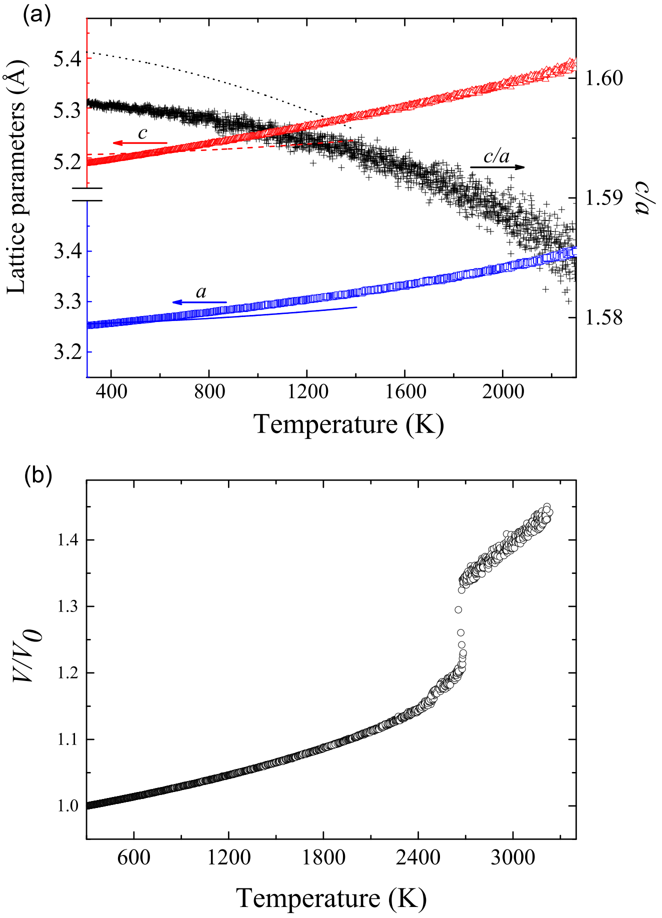

Figure 2.3: (a) Lattice parameters a (blue squares) and c (red triangles) and the ratio c/a (black crosses) calculated from the MD simulations as a function of temperature compared with experimental data Ref[180] (a: the blue solid line; c: the red dashed line; c/a: the black dotted line). (b) Variation of the normalized volume, V/V_0, as a function of temperature from the direct heating MD simulation. The system contained 2156 ZnO pairs, and was annealed from 300 K to 3300 K at a constant rate of 10 K/5 ps during the simulation.

(2.36 nm × 2.04 nm × 8.70 nm), whereby the c axis in the WZ structure was along the longest side of the cuboid. Here, we only considered the case that the melting fount is perpendicular to the c axis. In total, the simulation box contained 1536 ZnO pairs. The simulation box was divided into a solid phase region and a liquid phase region, both of which had equal numbers of ZnO pairs. The lattice parameters of the WZ-ZnO at 2200K obtained by the previous MD simulations were used to construct the solid phase. First the atoms in the solid phase were frozen while the liquid phase were equilibrated at temperatures of about 2200 K for 50000 time steps. The atoms in the solid phase were then released and equilibrated together with the liquid phase at NVE ensemble for 1.5×10^5 time steps, where the last 10^5 time steps were used to monitor the solid-liquid interfaces. The initial lengths of the cuboid sides were moderately changed in different attempts to obtain slightly different temperatures and pressures. An equilibrium P-T point was affirmed to be found only if the number of the $\{0001\}$ bilayers in solid phase remained unchanged during the last 10^5 time steps of simulation. Details of simulation methods can be found in Refs [182, 183]. We have tried more than 50 initial configurations and an equilibrated solid-liquid interface was found in nine of them. The melting temperature obtained from the two-phase method is 2308 K, which is in excellent agreement with experimental values [181].

2.3.4 High-Pressure Simulations

The pressure-induced WZ-to-RS phase transition in ZnO [111, 114–117, 129, 133, 136, 139, 143, 152] and other WZ crystals [93, 171, 184–186] is an intriguing phenomenon, whereby the mechanism remains unclear. The HC structure as a possible intermediate phase in the WZ-to-RS phase transition as predicted by DFT calculations [186] and molecular dynamics simulations [93, 143, 152, 184] has not yet been found experimentally. However the HC structure has been reported experimentally only in ZnO: a few layers of local HC structure have been observed at ZnO/Ag boundaries [187]. Our own DFT calculations showed that among several II-VI semiconductors (here we considered ZnS, CdS, and CdSe), ZnO has the smallest energy

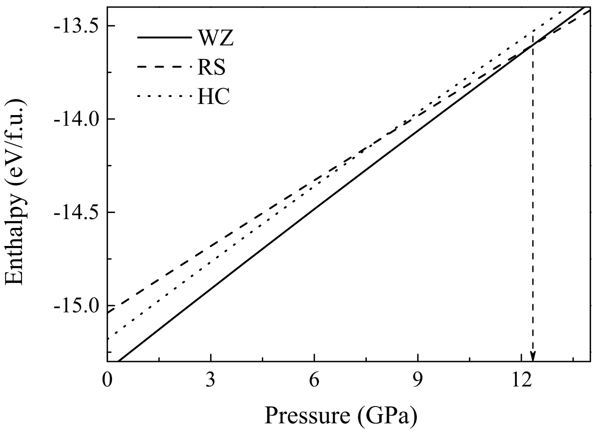

Figure 2.4: Enthalpies as a function of hydrostatic pressure for ZnO in the WZ (solid line), HC (dotted line) and RS (dashed line) structures. The vertical arrow indicates the pressure of equal enthalpy for the WZ and the RS structures.

difference of the HC structure compared to the WZ structure, $\Delta E_{\mathrm{HC-WZ}}$ ($\Delta E^{\mathrm{ZnO}}_{\mathrm{HC-WZ}} = 0.138$ eV/f.u.; $\Delta E^{\mathrm{ZnS}}_{\mathrm{HC-WZ}} = 0.332$ eV/f.u.; $\Delta E^{\mathrm{CdS}}_{\mathrm{HC-WZ}} = 0.180$ eV/f.u.; $\Delta E^{\mathrm{CdSe}}_{\mathrm{HC-WZ}} = 0.208$ eV/f.u.;) and the lowest value of ratio ρ, where $\rho = \Delta E_{\mathrm{HC-WZ}}/\Delta E_{\mathrm{RS-WZ}}$ under zero temperature zero pressure conditions ($\rho_{\mathrm{ZnO}} = 0.469$; $\rho_{\mathrm{ZnS}} = 0.530$; $\rho_{\mathrm{CdS}} = 0.672$; $\rho_{\mathrm{CdSe}} = 0.717$.) ZnO may be the best candidate to find stabilized HC structure in experiments.

Figure 2.4 shows the enthalpies of ZnO with WZ, HC and RS crystal structures as a function of hydrostatic pressure at 0 K. Our potential model predicts that the point where the enthalpies of the WZ- and RS- ZnO are equal is 12.3 GPa, which is slightly higher than that reported in experiments [114–117] (8.7-10.5 GPa) and in DFT calculations [111, 117, 136, 139] (6.6-14.5 GPa). The enthalpy of the HC structure never shows a minimum in the studied pressure range, which agrees with previous DFT studies [129]. Therefore, it is unlikely to stabilize the HC structure in ZnO by merely applying hydrostatic pressure.

However, it was predicted by DFT calculations [129] that in a certain pressure range, the enthalpy of HC-ZnO was minimized by applying uniaxial pressure along the c axis (the WZ <0001> direction). The transition pressure is 6.0 GPa found by means of DFT calculations using the local density approximation (LDA) [129]. Using our potential model, the WZ-to-HC transition under uniaxial pressure was tested by means of MD simulations. The same system as in the direct heating MD simulation was used and first equilibrated at 300 K and zero pressure for 2 ns. After equilibration, the temperature was kept constant at 300 K. Uniaxial pressure along the c axis was applied and increased at a rate of 0.05 GPa/10 ps until the pressure reached 10 GPa. Next, the uniaxial pressure was released at the same rate until it reached zero. During the compression and the reverse process, the pressure in other directions was kept at a value of zero. In Fig. 2.5 a, the snapshots of the ZnO matrix clearly indicate the WZ-to-HC phase transition and its reverse transition. By plotting the ratio of c/a as a function of pressure, it is shown in Fig. 2.5 c that the WZ-to-HC transition pressure takes place at 8.8 GPa and the reverse transition takes place at 2.9 GPa with a large hysteresis. Based on the previous studies [129] and our MD simulations, the HC structure is very likely to be stabilized by applying uniaxial pressure along the c axis in WZ-ZnO. If the HC phase can be stabilized in ZnO or other WZ materials, many interesting phenomena are expected to be observed: the dipole moments in the WZ nanostructures will totally disappear, and so does the piezoelectric property in the WZ materials. However, difficulties can be expected in experiments: for bulk materials, a perfect single crystal may be hard to access, as achieving a homogeneous transition in bulk materials is difficult. For mesomaterials or nanomaterials, applying a uniaxial pressure on a single object is difficult.

Another interesting phenomenon found in the MD simulations is that the BCT structure formed in the reverse HC-to-WZ transition (see Figs. 2.5 a and b). In Fig. 2.5 b, the final configuration of the released unit cell was expanded to a $3 \times 3 \times 3$ matrix and each atom was colored by the number of its nearest neighbors, n_{nn}. Here, the atoms are defined to be the nearest neighbors if their interatomic distance is less than 2.8 Å. In this way, the BCT domains ($n_{\mathrm{nn}} = 5$) and the WZ domains ($n_{\mathrm{nn}} = 4$) can be easily

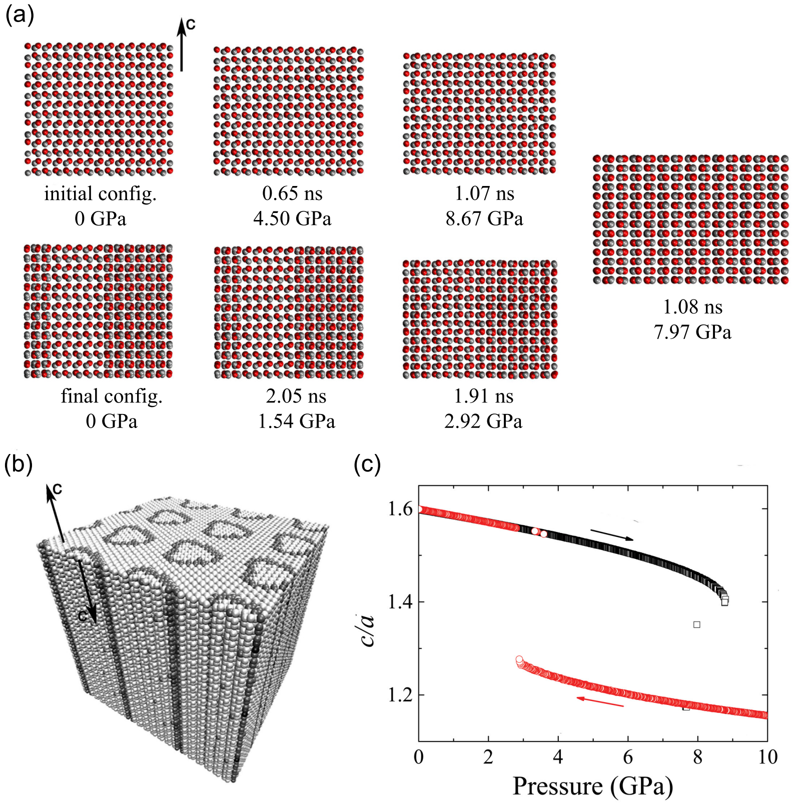

Figure 2.5: (a) Snapshots of bulk ZnO from MD simulations at 300 K. A uniaxial pressure was applied along the c axis (WZ <0001> direction) and released when it was reached 10 GPa. A WZ-to-HC phase transition was observed under an uniaxial pressure of 8.8 GPa and the reverse transition was observed under 2.9 GPa. The red and black spheres are O and Zn respectively (b) A $3 \times 3 \times 3$ matrix (lower left) shows that BCT-ZnO was formed as boundaries (darker regions) that separate two WZ-ZnO grains (lighter regions) with anti-parallel c axes (c) c/a as a function of uniaxial pressure from MD simulations. Black squares are the data from up-stroke phase transition and the red circles are the data from down-stroke reversed phase transition.

distinguished. It is clear from Fig. 2.5 b that the BCT-ZnO domains formed as boundaries that are separating two WZ-ZnO grains with anti-parallel c axes. Recently, there has been much discussion about the BCT structure in ZnO and other binary semiconductors [57, 74–78, 80, 137, 145], including molecular simulation studies with various ZnO potentials [74–76]. Here we note that the SMs derived by Binks *et al.* [81] and Alsunaidi *et al.* [154] overestimates the stability of BCT-ZnO. The relative energy differences of the BCT compared to the WZ ($\Delta E_{\mathrm{BCT-WZ}}$) calculated using these potential models [81, 155] is about 0.007 eV/f.u., which is very small in comparison to our DFT-GGA results of 0.048 eV/f.u. and previous LDA-GGA results [74] of 0.074 eV/f.u.. Therefore, we should strongly question the findings of the BCT-ZnO structure appearing in the molecular simulations as it may be an artifact of the interaction potential model.

2.3.5 Surface Energy Calculations

If the interaction potentials are to be used in the studies of ZnO nanostructures, the capability of the potentials to reproduce the surface properties of ZnO needs to be tested. Previous studies showed that the non-polar $\{10\bar{1}0\}$ and $\{11\bar{2}0\}$ surfaces are the most stable surfaces [188, 189]. However, the polar $\pm\{0001\}$ surfaces can be stabilized by different mechanisms [190–194]. The surface energies of these four different polar and non-polar surfaces in WZ-ZnO were calculated by both DFT and the ZnO potential model. In the classical LS simulations, four two-dimensional periodical slab models were constructed, whereby the four different surfaces are oriented in a non-periodic direction. These slabs were divided into two regions though the middle planes perpendicular to the surface normal. The atoms in the region 1 (surface region) were allowed to relax while the atoms in region 2 (bulk region) were fixed. The thickness of slabs was at least 20 Å and the surface areas ranged from 402 to 581 Å^2. It is possible to cut a slab with a $\{10\bar{1}0\}$ surface in two ways: either breaking one bond or two bonds. Only the former case is considered here, since it is most favorable. The $\{11\bar{2}0\}$ surface can only be cut in one way, while there are two ways for the $\pm\{0001\}$, one by breaking one bond, the other by breaking three bonds.

Again, only the surface obtained by breaking one bond is considered. In order to stabilize the polar surfaces, point defects [195] were constructed by moving a quarter of surface atoms from the surface to the bottoms of the slabs. The surface energies can be calculated as:

$$E = \frac{E_{\text{surface}} - nE_{\text{bulk}}}{A} \tag{2.10}$$

Where E_{surface} is the energy of all the atoms in the surface region, and n is the number of {ZnO} pairs in surface region, E_{bulk} is the energy per {ZnO} pair in the bulk, and A is the surface area of the simulation cell.

For the DFT calculations, the schemes used to calculate the surface energies are slightly different from those in the classical LS simulations. First, in DFT calculations, 3-D periodic conditions must be used so the vacuum needs to be constructed as a vacuum slab between the ZnO slab surfaces. Large slab models as in the LS simulations exceed the computational limit of DFT calculations. However, to obtain a reliable surface energy, both the slab itself and the vacuum must be sufficiently thick. The thickness of the $\{10\bar{1}0\}-$, $\{11\bar{2}0\}-$ and $\pm\{0001\}-$ slabs were 21.22 (16 layers), 19.36 (13 layers), and 29.20 (12 bilayers) Å, respectively, and the thickness of the vacuum layers were ∼28 Å. Monkhorst Pack k-meshes [167] of 28 × 17 × 1, 17 × 17 × 1, and 28 × 28 × 1 were used for the $\{10\bar{1}0\}-$, $\{11\bar{2}0\}-$ and $\pm\{0001\}-$ slabs, respectively. Second, since the total energy of the slab needs to be compared with the total energy of a bulk cell, only stoichiometric cells can be used. For the $\{10\bar{1}0\}$ and $\{11\bar{2}0\}$ surfaces, this is automatically the case, since each layer contains an equal amount of Zn and O. The {0001} surface slab however, consists of bilayers, thus an (unreconstructed) {0001}-slab always contains one Zn-terminated and one O-terminated surface. Since only the total energy can be calculated, these surfaces cannot be distinguished, and therefore an average surface energy is obtained.

The relaxed and unrelaxed surface energies of four surfaces are listed in Table 2.3 and are compared with SMs [153, 196], ReaxFF [88], and other DFT results [188–190]. Even though PCRIM was used in our ZnO potentials whereby surface atoms cannot have a different charge than the

Table 2.3: Relaxed and unrelaxed (in parentheses) surface energy for non-polar and polar ZnO surfaces in comparison with Shell Models (SMs), reactive force field (ReaxFF), and DFT calculations. The unit of the surface energy is in J/m^2.

	Force Fields				Ab-Initio Calculations	
	PCRIM	SM[a]	SM[b]	ReaxFF[c]	this work	literature[d]
$\{10\bar{1}0\}$	1.46 (1.60)	1.1	1.003	0.96	0.94 (1.28)	1.04 (1.20), 1.3
$\{11\bar{2}0\}$	1.51 (1.59)	1.2	-	1.06	0.98 (1.28)	1.06 (1.19), 1.4
Zn-$\{0001\}$	2.00 (2.53)[e]	2.1[f]	-	-	1.90 (2.16)[g]	($\sim$2.0)[h]
O-$\{000\bar{1}\}$	2.23 (3.04)[e]					

[a] Ref. [196]; [b] Ref. [153]; [c] Ref. [88]; [d] Ref. [188–190]; [e] "Point defects" [195] were constructed on the surfaces in order to remove the dipole moments; [f] 1/4 of the surface atoms were removed from both sides of the polar surfaces to stabilized them [196]. The difference in surface energies between the Zn-terminated and O-terminated ±{0001} surfaces can not be distinguished; [g] The average of the Zn-terminated and O-terminated ±{0001} surfaces; [h] The average of unrelaxed surface energies of the Zn-terminated and O-terminated ±{0001} surfaces, which is derived by the cleavage energy [190] divided by two.

bulk atoms, the surface energy calculations with the newly developed potentials show considerable agreement with DFT results. The calculations predict the correct relative order of the surface energies for different surfaces: $E_{O-\{000\bar{1}\}}$ and $E_{Zn-\{0001\}} > E_{\{11\bar{2}0\}} > E_{\{10\bar{1}0\}}$. However, the surface energies calculated for the non-polar $\{10\bar{1}0\}$ and $\{11\bar{2}0\}$ surfaces using our ZnO potential model ($\sim$1.5 J/m^2) are slightly larger than those obtained from the DFT calculations (0.94$\sim$1.4 J/m^2). SMs and ReaxFF shows better capabilities to reproduce the surface energies of non-polar surfaces of ZnO than the PCRIM.

2.4 Conclusions

Two main conclusions can be drawn from this chapter: (1) we demonstrated that the combination of the LI, empirical and ab-initio energy surfaces fittings is an efficient way to develop new potentials with high intrinsic accuracy. (2) a high-performance set of interatomic pair potentials based on an

8-parameters PCRIM was developed and validated for ZnO. Compared to other SMs, ABOP, or ReaxFF, which have much more parameters and much more complex functional forms to describe the interactions, our 8-parameter PCRIM shows similar or even better results in reproducing physical properties of ZnO. These physical properties include the lattice parameters, elastic constants, bulk modulus, structural stabilities, lattice dynamics and surface energies. The variation of the lattice parameters of WZ-ZnO at high temperature conditions can be quantitatively correctly described by the potentials. The melting point of ZnO was estimated to be 2308 K by the two-phase method which is in excellent agreement with the experimental result of 2242 K. The coexistence pressure of the WZ and RS phase at 0 K is predicted at 12.3 GPa. A WZ-to-HC transition induced by uniaxial pressure predicted by previous DFT calculations was also reproduced by means of MD simulations with our newly developed ZnO potential model. Finally we summarized the shortcomings of our ZnO potential model: (1) The stabilities of the CsCl structures in ZnO are underestimated by this model; (2) The linear expansion coefficient of WZ-ZnO is overestimated by a factor of three when compared with experimental data; (3) The surface energies calculated for the non-polar $\{10\bar{1}0\}$ and $\{11\bar{2}0\}$ surfaces are slightly larger than the DFT results. In this chapter, we explored a rational and efficient routine to develop pair potentials for a binary compound. There is an urgent need for a set of simple but effective potentials to extend theoretical studies on semiconductor materials, especially for accurate modeling of phase transitions and big systems. Using this new approach to developing potentials, many other potentials for materials of interest could be developed. In particular, this novel set of potentials for ZnO is expected to enable reliable studies of the physical properties of ZnO bulk materials and certain of the solid-solid phase transitions in ZnO. Surface properties are essential at nanoscale. Some of the calculated surface energies by this potential model deviate from DFT-GGA results about 50%. However, differences in DFT results with different schemes (LDA, GGA, B3LYP, and HF) are also large [189]. Whether this potential model is suitable to use in simulating ZnO nanostructures is still unclear. We encourage reader to apply our ZnO potential model to ZnO nanostructures and compare the results with first principles calculations or experiments.

Chapter 3

Deriving a Transferable Force Field for CdS-CdSe-PbS-PbSe Solid Systems

This chapter is based on the paper: Z. Fan, R. S. Koster, S. Wang, C. Fang, A. O. Yalcin, F. D. Tichelaar, H. W. Zandbergen, M. A. van Huis, and T. J. H. Vlugt, 'A Transferable Force Field for CdS-CdSe-PbS-PbSe Solid Systems', J. Chem. Phys., 2014, ***141****, pp 244503*

3.1 Introduction

Transition metal monochalcogenides with the formula ME (M is a transition metal, E = S, Se, or Te) are key materials in the development of nanoscience and nanotechnology [197–200]. Within this class of materials, cadmium chalcogenides (CdE) and lead chalcogenides (PbE) are abundantly used because of their each intriguing physical properties. CdE are wide-bandgap II-VI semiconductors with a four-fold wurtzite (WZ) or zinc blende (ZB) crystalline structures [201]. CdE nanostructures show quantum confinement so that the effective band gap depends on the crystalline size [202]. PbE belong to IV-VI semiconductors forming a six-fold rocksalt (RS) crystalline structure [203], which are important thermoelectric materials with a low thermal conductivity and high thermoelectric figures of merit [204, 205]. CdE and PbE nanocrystals (NCs) can be synthesized in diverse morphologies, *e.g.*, spheres, cubes, rods, tetrahedrons, truncated octahedron, and hexagonal disks [197, 206–211]. These NCs can also be used as seeds in the seed growth (SG) process to obtain heteronanocrystals (HNCs) such as core-shell and core-multishell structures, tetrapods and octapods, and nanodumbbells [18–20]. Recently, oriented attachment (OA) and ion exchange (IE) [33, 212, 213] have been shown to be very powerful tools in the synthesis and design of nanostructures. In OA, NCs are used as building blocks and are assembled in different patterns depending on the preferred attachments of particular facets [30, 213]. In the IE process, either the cations or anions in a nanostructure are partially or completely replaced by a substitutional ion from a solution or vapor [33, 212]. OA and IC can be independently used [9, 24, 25, 27, 35, 214–216] or combined [23] to synthesize nanostructures such as nanowires, nanorod couples, dimers, thin films, and 2-D superlattices. They are promising techniques in the design and application of nanomaterials and nanodevices.

To theoretically study bulk crystalline materials, first principles density functional theory (DFT) calculations using three-dimensional periodic boundary conditions provide reliable and accurate results within affordable computational requirements [35, 82, 136, 139, 217–219]. However, to simulate NCs containing more than a few thousands of atoms, DFT calculations are no longer possible because of the huge computational demands. Instead, classical molecular simulations techniques such as molecular dynamics (MD) or Monte Carlo (MC) using classical force fields are more commonly used to deal with large systems [35, 68, 75, 94]. Deriving accurate force fields using appropriate functional forms is an essential prerequisite for performing reliable and accurate classical MD and MC simulations.

There is limited number of force field models developed for cadmium chalcogenides. Wright and Gale [220] proposed a transferable shell model (SM) for both ZnS and CdS. The SM has a long history of success in modeling ionic materials [221]. In such a model, an ion is presented by a massive and positively charged core and a massless and negatively charged shell, and a "spring" is used to connect the core and shell, thus the SM is able to describe ionic polarizability. The SM developed by Wright and Gale [220] is able to accurately reproduce several physical properties for ZnS but has a poor performance for CdS. Moreover, there are three limitations in this SM: (1) most transition metal chalcogenides are partially ionic and partially covalent [222], but full integer charges, $\pm 2\ e$ were still used in this model. The use of integer charges in force fields of ionic solid materials helps their transferability and enables modelling of the energy and local structure of defects in the materials [91, 155, 223]. However, there is also evidence that force fields developed for ionic solids using partial charges [82, 94, 224] have superior performance to those using integer charges [220, 225, 226] for reproducing physical properties such as lattice parameters, elastic constants, and phase stabilities; (2) Three-body and four-body interatomic interaction potentials were used in this SM to stabilize the tetrahedrally coordinated structure of CdS and ZnS. Three-body interatomic interaction potentials are often used to describe the directional feature of the covalent bonds. However the presently used functional forms of these angle dependent potentials [220, 227] are often pointed to the materials' stable phases with a particular bond angle (*e.g.* 104.7° for tetrahedral coordination structures), thus the stabilities for other structures with different bond angles (*e.g.*, 90° and 180° for octahedral coordination structures) are significantly underestimated. (3) One third of the total atoms are extra "shell" atoms which decreases the computational efficiency. Other interaction models which do not include charges and attempt to incorporate Coulomb interactions into effective two-body or many-body interactions. Two examples thereof are a transferable Stillinger-Weber (SW) potential developed for the Zn-Cd-Hg-S-Se-Te system [227] and a analytical bond order potential (ABOP) for Cd-Zn-Te systems [228]. These potentials cover several elements and can accurately reproduce the lattice parameters, elastic properties and cohesive energies for II-VI binary compounds in the four-fold WZ or ZB structures. However, both the SW potential [227] and the ABOP [228] models failed to accurately reproduce the relative stabilities between the six-fold RS phase and the four-fold WZ and ZB phases. Therefore, the description of the pressure-induced ZB-to-RS or WZ-to-RS phase transitions in II-VI binary compounds using these potential models could be questionable. A simple but effective partially charged rigid ion model (PCRIM) [163] was first used to develop a pair potential for CdSe by Rabani [92], and the model was extended to CdS and ZnS by Grünwald et al [94]. In this model, effective charges of ±1.18 e were set for cations and anions, and Lennard-Jones (LJ) potentials were used to describe the short-range interactions (in the text, this model will be referred as the LJ model) [92, 94]. Unlike the SM, SW potentials, and the ABOP model mentioned above [220, 227, 228] which are only valid to describe the four-fold WZ and ZB phases, this LJ model captured the energy features for three phases, WZ, ZB and RS [92, 94]. Therefore, it has been frequently used in simulation studies of phase transitions [68, 93, 184, 229]. One minor flaw in this LJ model is that the parameterization was over-constrained: Both the cation-cation and anion-anion short-range interatomic interactions were included and the remaining parameters in the cross terms (cation-anion, S-Se, and Zn-Cd short-range interatomic interactions) are obtained by the Lorentz-Berthelot mixing rules. Using too many constrains in the fitting procedures decreases the degrees of the freedom, thus may lead to less accurate results. For example, the calculated bulk moduli of CdS and CdSe by this LJ model were smaller than the experimental data, and physical properties of ZnSe can not be accurately described by this LJ model [94]. There are even fewer force fields published for lead chalcogenides. Schapotschnikow *et al.* [31] derived a pair potential model for PbSe within the same LJ model approach, and used it in the atomistic simulations of the morphological transformations and fusion of PbSe NCs. In this LJ model for PbSe, the effective charges for Pb and Se ions are ±1.29 e, and the parameters that describe the Se-Se short-range interactions in PbSe are very different from that in the LJ model for CdSe [92]. Therefore, to describe the PbSe-CdSe ternary system, this PbSe LJ model [31] cannot be easily combined with the CdSe LJ model [92]. The

PCRIM has also been applied to develop force fields for PbTe [217, 230]. To our best knowledge, no force field has yet been published for PbS.

When deriving force fields for ionic solid materials, it is important to note the following: (1) For half-ionic-half-covalent materials, the use of partial (effective) charges has a considerable advantage over using full integer charges [82]. (2) Although three-body and many-body interactions may exist in the systems, including them in a force field model should be applied with caution. In many cases, force fields consisting of only pair potentials can already describe a wide range of polymorphs for materials with considerably good accuracy [31, 82, 92, 94], but those including many-body potentials can often be applied to fewer phases [217, 220, 227]. (3) Force fields developed by following a conventional fitting procedure whereby the training sets merely include available experimental data can not satisfy the increasing needs of high accuracy and wide utilizable range [83]. DFT and ab-initio-MD data are commonly included in the training sets to develop "nearly prefect" force fields to describe not only crystal structures, elastic and vibration properties, but also properties of high-pressure, metastable, liquid, and gas phases, and of different surfaces and interfaces [31, 82, 155, 217, 228]. On the other hand, a classical force field can never perfectly describe the quantum world. However, using suitable functional forms with careful parameterization, a derived classical force field with simple functional forms can capture many essential physical and chemical properties of materials and is useful in the atomistic simulations for large systems (*e.g.*, nanostructures).

We developed a transferable PCRIM for the CdS-CdS-PbS-PbSe solid system and used it in a MD study of cation exchange in PbSe-CdSe HNCs. In this model, the values of the effective charges were determined by a Bader analysis [56]. The short-range interatomic interaction potentials were parameterized to reproduce the lattice parameters, elastic properties, and relative stability for CdS, CdSe, PbS, and PbSe polymorphs. In particular, we included the relative stabilities of stable WZ and ZB, high-pressure RS and CsCl, and metastable honeycomb (HC) phases from DFT calculations in the training set to ensure an accurate description of the possible structural transitions. DFT calculations for the four II-VI and IV-VI binary compounds and a board range of validation tests for the force field are also

Table 3.1: DFT-calculated Bader charges of cations in CdS, CdSe, PbS, and PbSe polymorphs. All charges are in e.

	CsCl	RS	ZB	WZ	HC
CdS	0.847	0.810	0.852	0.867	0.843
CdSe	0.712	0.825	0.725	0.711	0.750
PbS	0.929	1.001	0.913	-	0.933
PbSe	0.813	0.812	0.804	-	0.781

provided in details.

3.2 Methods

3.2.1 Density Functional Theory Calculations

First principles DFT calculations were employed to calculate the crystal structures and relative stabilities of CdS, CdSe, PbS and PbSe polymorphs and their mixed phases, as well as the surface energies for several different non-polar surfaces in WZ-CdX (X = S or Se) and RS-PbX. For each material, calculations were performed for five polymorphs: WZ, RS, ZB, HC and CsCl (Figure 3.1 a-e). By a full structural optimization, WZ-PbX will automatically transfer into a five-fold HC structure, which indicates that the WZ phase is unstable for PbS and PbSe. A Bader charge analysis [56] was carried out to determine the effective charges on the atoms for each polymorph. For the details of these DFT calculations, we refer to our previous work [35, 82]. The results of the Bader charges of the cations are listed in Table 3.1. Differences between the Bader charges of different materials and different structures are small. These similar Bader charges enable us to develop a transferable force field with a uniform absolute value of effective charge for all four materials. The effective charges were fixed at ± 0.8 e for all cations and anions as in our previous work [35].

To provide DFT data of the mixed phases for the fitting procedure, four

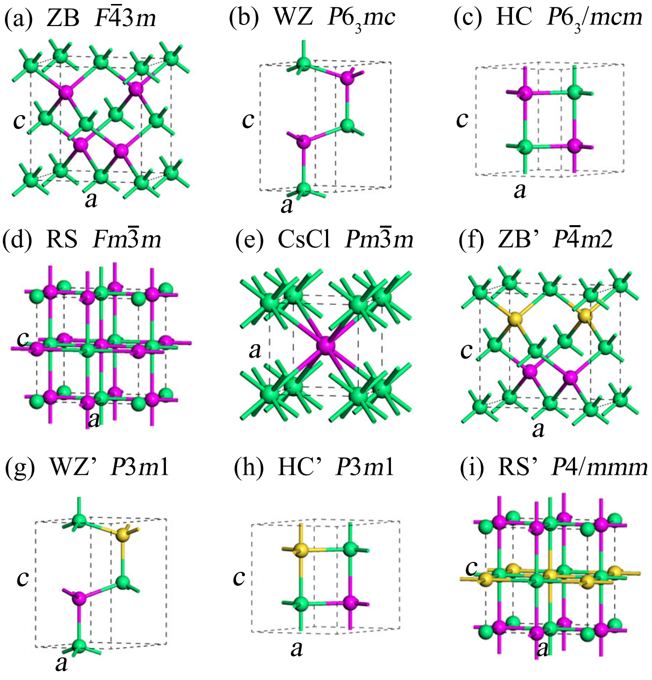
(a) ZB $F\bar{4}3m$
(b) WZ $P6_3mc$
(c) HC $P6_3/mcm$
(d) RS $Fm\bar{3}m$
(e) CsCl $Pm\bar{3}m$
(f) ZB' $P\bar{4}m2$
(g) WZ' $P3m1$
(h) HC' $P3m1$
(i) RS' $P4/mmm$
c
a

Figure 3.1: Unit cells for binary compounds (a-e) and for QMPs (f-i). (a) ZB, (b) WZ, (c) HC, (d) RS, (e) CsCl, (f) ZB', (g) WZ', (h) HC', and (i) RS'. The space groups are listed for each structures. The green spheres represent one type of cations (Cd or Pb); Yellow and purple spheres represent two different anions (S and Se).

quasi-mixed phases (QMPs) were constructed by replacing half of the total anions in a unit cell (S and Se) with the other type (Se or S). The formulas of these QMPs are Cd_2SSe and Pb_2SSe. Due to the relatively small unit cell used, rather than being randomly distributed, the two different anions are arranged in alternate layers in the QMPs when 3-D periodic boundary conditions applied. We labeled these QMPs as WZ', RS', ZB', and HC' to correlate them with their original crystal structures and also to mark the reduced symmetry of these QMPs with a prime symbol. Schematic representations of these QMPs are shown in Figure 3.1 f-i together with their space groups. Note that because of the reduced symmetry in these QMPs, the internal coordinations in these QMPs may differ from those in their correlated crystal structures, and for ZB' and RS', lattice parameter a is not necessarily equal to c. Full structural optimization were carried out for WZ'-, ZB'-, and RS'-Cd_2SSe and HC'-, ZB'- and RS'-Pb_2SSe. The basic set-up of DFT calculations for each QMP is the same as that for its correlated crystal structure.

3.2.2 Fitting Methodology

The functional format of the interaction potentials for CdS and PbS were kept the same as those for CdSe and PbSe [35]. It only contains Coulomb interactions and short-range two-body interactions [35]:

$$u_{ij} = \frac{q_i q_j}{r_{ij}} + Ae^{-r_{ij}/\rho} - \frac{C_6}{r_{ij}^6} \tag{3.1}$$

The first term describes the long-range Coulomb interactions. The second and the third terms are the Buckingham potential that describes the repulsive and dipole-dipole interactions. A, ρ and C_6 are parameters to be obtained by fitting. The short-range cation-cation interactions (the Buckingham potential) are ignored.

Both a conventional and relaxed fitting procedure [83] were used to obtain the parameters. Empirical fitting based on experimental data and relaxed ab-initio energy surface fitting [35, 82] based on DFT data were combined to obtain all parameters. All 18 parameters in the Buckingham potentials were relaxed simultaneously and obtained by fitting to the experimental data, including the lattice parameters and elastic constants of RS-PbX, WZ- and ZB-CdX measured at room temperature, as well as the DFT data, including the lattice parameters and relative stabilities of RS-, ZB-, CsCl-, and HC-PbX and WZ-, ZB-, RS-, and HC-CdX. For DFT-GGA calculations are generally known to systemically show larger lattice parameters in comparison to experimental data. The lattice parameters obtained by our DFT-GGA calculations were normalized by rescaling their volumes [35, 82]. All calculations in the fitting procedures were carried out by GULP [177]. A cut-off radius of 12 Å was set for the short-range Buckingham potentials and long-range tail correction were not applied. The Ewald summation method [61, 174] was used to calculate the electrostatic interactions. Further details about the fitting procedures can be found elsewhere [35].

To complete the parameter set, the parameters of the short-range S-Se Buckingham potential are also required. These parameters were obtained by fitting the DFT data of the lattice parameters, internal coordinations, and relative stabilities of the QMPs (WZ'-, ZB'-, and RS'-Cd_2SSe; and RS'-, ZB'-, and HC'-Pb_2SSe). The lattice parameters of the QMPs from the DFT-GGA calculations were also rescaled [35, 82] for fitting. During fitting, all previously determined parameters remained unchanged, only the three parameters A, ρ and C_6 in the S-Se Buckingham potential were relaxed. The complete parameter set of the transferable force field for CdS-CdSe-PbS-PbSe system is listed in Table 3.2.

3.2.3 Molecular Dynamics Simulations

MD simulations were used to compute several properties of the CdX and PbX and their mixed phase at finite temperatures. For bulk materials, periodic matrices containing about 4000 atoms were constructed for WZ- and ZB-CdX and RS-PbX based on the experimental lattice parameters. In the MD simulations, the equations of motion were integrated using the velocity Verlet algorithm with a time step of 1 fs. At $T = 300$ K and $p = 0$ GPa, Each MD simulation of 0.5 ns was performed in the Isobaric-Isothermal

Table 3.2: The complete set of parameters of the transferable force field for CdS, CdSe, PbS, PbSe, and their mixed phases (see Eq. 6.1). Parameters A, ρ, and C are in eV, Å, and eV·Å^6, respectively. The short-range interactions between cations are ignored. The effective ion charges q are ± 0.8 e.

interaction	A	ρ	C
Cd-S	1.26×10^9	0.107	53.5
Cd-Se	2.64×10^9	0.108	64.4
Pb-S	3.05×10^6	0.173	154
Pb-Se	4.88×10^6	0.173	211
S-S	4.68×10^3	0.374	120
Se-Se	5.20×10^3	0.384	127
S-Se	5.44×10^3	0.376	122

(NpT) ensemble, The first 0.1 ns was used for equilibration whereby the velocities were rescaled to the target temperature. This MD time is long enough to equilibrate the systems. The temperature and the pressure were controlled by a standard Nosé-Hoover thermostat and barostat [231].

3.3 Physical Properties of CdS, CdSe, PbS, and PbSe

We first test our transferable force field by reproducing the geometrical structures and elastic properties of CdX and PbX. For the lattice parameters, we considered five structures (WZ, ZB, RS, HC and CsCl) for CdX and four structures (RS, ZB, HC and CsCl) for PbX. For the elastic constants and bulk moduli, we only considered the most stable phases for CdX (WZ and ZB) and PbX (RS). Reliable experimental data are only partially available for the lattice parameters, elastic constants, and bulk moduli of these binary compounds in their stable and high-pressure phases. Lattice parameters for the other phases can only be compared with DFT calculations. In addition, MD simulations were performed for the stable phases for each material to obtained the lattice parameters at finite temperature (300 K).

The results are listed in Tables 3.3 and 3.4 for lattice parameters and elastic properties, respectively, together with available experimental data, DFT calculations and the results calculated using the LJ models [31, 92, 94]. It should be clarified that most of these physical properties were used in the fitting procedure as training sets, therefore our potential set was expected to accurately reproduce these properties. As is shown in Table 3.3 and 3.4, this new force field is able to accurately reproduce all properties concerned for all four binary compounds. Compared to other models [31, 92, 94], our force field model shows equivalent or higher accuracy when reproducing lattice parameters and elastic properties. Note that we repeated the calculations using the previous LJ models for CdS [94], CdSe [92] and PbSe [31]. The results were slightly different from the original values reported [31, 92, 94].

The cohesive energy, defined as the energy required for separating a solid or liquid into isolated free atoms, is often used to describe the energy features of condensed materials and to compare the energies of a material between different phases. Cohesive energies of solids can be either measured by experiments or calculated by DFT. The cohesive energies of WZ-CdX and RS-PbX calculated by DFT-GGA are listed in Table 3.5. The DFT-calculated cohesive energies of CdS and CdSe are 6.603 and 5.414 eV/f.u., respectively, which are slightly larger than the experimentally measured values [232] of 5.71 and 4.93 eV/f.u. for CdS and CdSe, respectively. The cohesive energies by DFT calculations are 8.640 and 8.065 eV/f.u. for PbS and PbSe, respectively. For PbX, there is no available experimental data for comparison. These DFT-calculated cohesive energy values were not included in the training set for fitting, because the PCRIM was chosen to describe the interatomic interactions whereby the ions remain charged while being pulled apart from each other [82]. Therefore, force field models with fixed charges are only applicable to calculating lattice energies (the energy required for separating a solid into a gas of its ions). The lattice energies calculated with the present force field are -6.320, -6.027, -6.034, and -6.079 eV/f.u for WZ-CdS, WZ-CdSe, RS-PbS, and RS-PbSe, respectively. For a more detail discussion on the difference between the lattice energy and the cohesive energy, the reader is referred to Refs. [82, 223].

Compared to reproducing the absolute energies (cohesive energy or lattice energy), accurately reproducing the relative stability (energies) of different phases of a material is more important for a force field to accurately simulate solid-solid phase transitions [82]. The relative stability of polymorphs was included in the training set, thus assuring accuracy in describing the related solid-solid phase transitions [82]. The calculated relative stabilities are also listed in Table 3.5, in comparison with the data calculated with the LJ models [31, 92, 94] and by DFT-GGA. According to our DFT-GGA results, CdS and CdSe have very similar relations of the phase stabilities. The order of their polymorphic stabilities is: $E_{\mathrm{WZ}} \sim E_{\mathrm{ZB}} < E_{\mathrm{HC}} < E_{\mathrm{RS}} < E_{\mathrm{CsCl}}$. Here, E can either be the opposite number of cohesive energy or the total energy. Note that our DFT-GGA calculations predicted a higher stability of the HC phase than the RS phase for CdSe at zero temperature and zero pressure conditions, in contrast to previous DFT calculations whereby the local density approximation (LDA) was used [218]. In general, both of our new transferable PCRIM and the previous LJ model [92, 94] can correctly reproduce the order of the stabilities for CdX. We first discuss the relative stabilities of the WZ, HC, and RS phases, which are involved in the extensively studied pressure-induced WZ-to-RS phase transition [93, 136, 139, 143, 171, 184, 229, 233]. Figure 3.2 shows the enthalpies (H) of CdX with the WZ and RS structures as a function of hydrostatic pressure at 0 K. The points where $H_{\mathrm{WZ}}=H_{\mathrm{RS}}$ are 4.8 and 4.1 GPa for CdS and CdSe, respectively. These results are in good agreement with the recently reported experimental measurements of the transition pressures for CdS (3.0∼4.3 GPa) [234] and CdSe (3.0∼4.8 GPa) [235]. The LJ model [92, 94] for CdS and CdSe shows smaller values of $\Delta E_{\mathrm{RS-WZ}}$ and $\Delta E_{\mathrm{HC-WZ}}$ compared to our force field model and DFT-GGA calculations, thus yielding slightly lower transition pressures [94]. Both the present model and the LJ model [92, 94] show similar ratios of $\Delta E_{\mathrm{HC-WZ}}/\Delta E_{\mathrm{RS-WZ}} \sim 0.5$ which is smaller than the DFT results of ∼0.7. This deviation may contribute to a slightly biased preference of the HC phase as an intermediate phase in the route of the WZ-to-RS phase transition when applying these models [93, 184, 236]. To the best of our knowledge, the classical force field model presented in this work provides the most accurate description of the pressure-induced WZ-to-RS phase transition for CdS and CdSe.

Table 3.3: Lattice parameters of CdS, CdSe, PbS and PbSe polymorphs calculated by lattice statics and MD simulations using the present force field, compared with experimental and DFT data and the results calculated by the LJ models of Refs. [31, 94]. Lattice parameters a and c are in Å; u is the internal coordinate. The values in parentheses are MD results at 300 K; the values in square brackets are normalized lattice parameters from DFT calculations; the values in bold are data used for the fit of the force field parameters.

	CsCl	RS	ZB	WZ			HC	
	a	a	a	a	c	u	a	c
CdS								
Expt.	-	5.32 (4.3 GPa)^{a}	5.83^{b}	**4.14**^{b}	**6.72**^{b}	**0.378**^{b}	-	-
PCRIM, this work	3.59	5.39	5.81 (5.86)	4.13 (4.17)	6.63 (6.69)	0.379	4.38	5.54
LJ model^{c}	3.53	5.43	5.83	4.16	6.59	0.384	4.43	5.52
DFT, this work	3.42 [3.36]	5.51 [**5.41**]	5.94 [**5.83**]	4.21	6.85	0.377	4.45 [**4.37**]	5.82 [**5.72**]
CdSe								
Expt.	-	5.54 (4.8 GPa)^{d}	6.08^{b}	**4.30**^{b}	**7.01**^{b}	**0.376**^{b}	-	-
PCRIM, this work	3.77	5.63	6.08 (6.13)	4.32 (4.36)	6.94 (7.00)	0.379	4.57	5.63
LJ model^{c}	3.75	5.74	6.14	4.38	6.96	0.383	4.64	5.94
DFT, this work	3.56 [3.49]	5.75 [**5.63**]	6.21 [**6.08**]	4.39	7.17	0.377	4.66 [**4.56**]	6.07 [**5.94**]
PbS								
Expt.	3.29 (25 GPa)^{e}	**5.94**^{f}	-	-	-	-	-	-
PCRIM, this work	3.62	5.94 (5.99)	6.67	-	-	-	5.06	5.91
DFT, this work	3.64 [**3.61**]	6.00	6.64 [**6.58**]	-	-	-	5.03 [**4.98**]	6.01 [**5.95**]
PbSe								
Expt.	3.38 (30 GPa)^{e}	**6.12**^{f}	-	-	-	-	-	-
PCRIM, this work	3.71	6.09 (6.13)	6.84	-	-	-	5.18	6.05
LJ model^{g}	3.66	6.05	6.77	-	-	-	5.14	6.01
DFT, this work	3.77 [**3.72**]	6.21	6.89 [**6.80**]	-	-	-	5.21 [**5.14**]	6.23 [**6.15**]

^{a} Ref. [234]; ^{b} Ref. [201]; ^{c} Calculated using the LJ model reported in Ref. [94]; ^{d} Ref. [235]; ^{e} Ref. [237]; ^{f} Ref. [203]; ^{g} Calculated using the LJ model reported in Ref. [31]

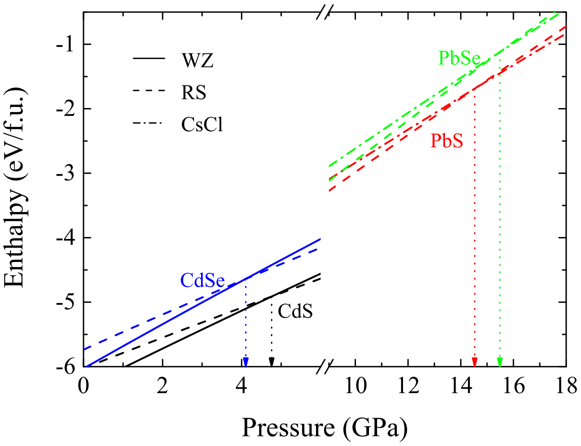

Figure 3.2: Calculated enthalpies (H) as a function of hydrostatic pressure for CdS (black lines), CdSe (blue lines), PbS (red lines) an PbSe (green lines) in the WZ (solid lines), RS (dash lines) and CsCl (dash-dot line) structures. The vertical arrow indicates the pressure where $H_{\mathrm{WZ}} = H_{\mathrm{RS}}$ or $H_{\mathrm{RS}} = H_{\mathrm{CsCl}}$.

Another issue is the relative stability of the WZ and ZB structures in CdX. In II-VI group semiconductors, some materials form the WZ structure in nature (*e.g.* ZnO, CdS, and CdSe) and some form the ZB structure (*e.g.* CdTe, ZnS, ZnSe and ZnTe). The relative stability of WZ and ZB is similar (energy difference less than a few meV/atom), especially for CdS and CdSe which have almost the same stability or energy of the WZ and ZB polymorphs at zero temperature zero pressure conditions based on DFT calculations. Calculated using a force field for tetrahedrally coordinated materials that only contain Coulomb interactions and two-body potentials, the WZ phase is always more stable than the ZB phase [82, 92, 94, 155, 238]. This is naturally true for ZnO [82, 155], but not for other II-VI semiconductors. To correct this issue, three-body and even four-body interactions were proposed to be added in force field models for CdS and ZnS [195, 220]. This restricts the utilizable range of the force field to only the four-fold WZ or ZB structures. The functions used for the three-body interactions resulted into a unique preferred bond angle of 109.5°, which led to an artificially low stability of other non-tetrahedrally coordinated phases (*e.g.* the six-fold RS phase). The same problem also exists in the SW potential [227], which yields exactly equal stability for WZ and ZB but significantly underestimateded

Table 3.4: Elastic constants and bulk moduli of WZ-, ZB-CdX and RS-PbX calculated using the present force field and the LJ models of Refs. [31, 94], together with experimental data. The elastic constant c_{ij} and bulk modulus B are in GPa. The values in bold are data used for the fit of the force field parameters.

	c_{11}	c_{12}	c_{13}	c_{33}	c_{44}	c_{66}	B
WZ-CdS							
Expt.[a]	**86.5**	**54.0**	**47.3**	**94.4**	**15.0**	**16.3**	**62.7**
PCRIM, this work	85.3	56.2	48.4	85.4	14.6	14.5	62.3
LJ model[b]	79.4	47.9	41.8	74.8	17.6	15.7	55.0
ZB-CdS							
Expt.[a]	**77.0**	**53.9**	-	-	**23.6**	-	**61.6**
PCRIM, this work	72.4	57.2	-	-	24.2	-	62.3
LJ model[b]	65.0	50.0	-	-	27.7	-	55.0
WZ-CdSe							
Expt.[a]	**74.1**	**45.2**	**39.0**	**84.3**	**13.4**	**14.5**	**53.1**
PCRIM, this work	72.4	47.9	41.4	72.5	12.3	12.2	53.1
LJ model[b]	65.9	38.0	32.9	64.4	15.2	14.0	44.8
ZB-CdSe							
Expt.[a]	**66.7**	**46.3**	-	-	**22.3**	-	**53.1**
PCRIM, this work	61.6	48.8	-	-	20.3	-	53.1
LJ model[b]	53.8	40.2	-	-	24.2	-	44.7
RS-PbS							
Expt.[c]	**126.0**	**16.0**	-	-	**17.0**	-	**49.9**
PCRIM, this work	127.0	16.3	-	-	16.3	-	53.2
RS-PbSe							
Expt.[c]	**123.7**	**19.3**	-	-	**15.9**	-	**54.1**
PCRIM, this work	129.9	16.5	-	-	16.5	-	54.3
LJ model[d]	125.0	19.1	-	-	19.1	-	54.4

[a] Ref. [201], [b] Calculated using the LJ model reported in Ref. [94], [c] Ref. [203], [d] Calculated using the LJ model reported in Ref. [31]

Table 3.5: Relative energy differences of CdS, CdSe, PbS and PbSe polymorphs calculated using the present force field and the LJ models of Refs. [31, 94], in comparison with DFT data. The number 0 indicates the most stable phase among the polymorphs. The values in parentheses are the cohesive energies calculated by DFT or the lattice energies calculated with the force fields. The values in bold are data used for the fit of the force field parameters. The energy differences, cohesive energies, and lattice energies are reported in eV/f.u..

	CsCl	RS	ZB	WZ	HC
CdS					
DFT, this work	1.278	**0.268**	**0.002**	**0** (6.063)	**0.180**
PCRIM, this work	1.341	0.297	0.015	0 (6.320)	0.149
LJ model[a]	1.358	0.095	0.030	0 (12.095)	0.066
CdSe					
DFT, this work	1.200	**0.292**	**0**	**0.002** (5.414)	**0.210**
PCRIM, this work	1.290	0.291	0.014	0 (6.027)	0.149
LJ model[a]	1.396	0.148	0.027	0 (11.486)	0.082
PbS					
DFT, this work	**0.508**	**0** (8.640)	**0.380**	-	**0.316**
PCRIM, this work	0.467	0 (6.034)	0.360	-	0.373
PbSe					
DFT, this work	**0.478**	**0** (8.065)	**0.374**	-	**0.320**
PCRIM, this work	0.528	0 (6.079)	0.381	-	0.397
LJ model[b]	0.428	0 (12.922)	0.464	-	0.423

[a] Calculated using the LJ model reported in Ref. [94], [b] Calculated using the LJ model reported in Ref. [31]

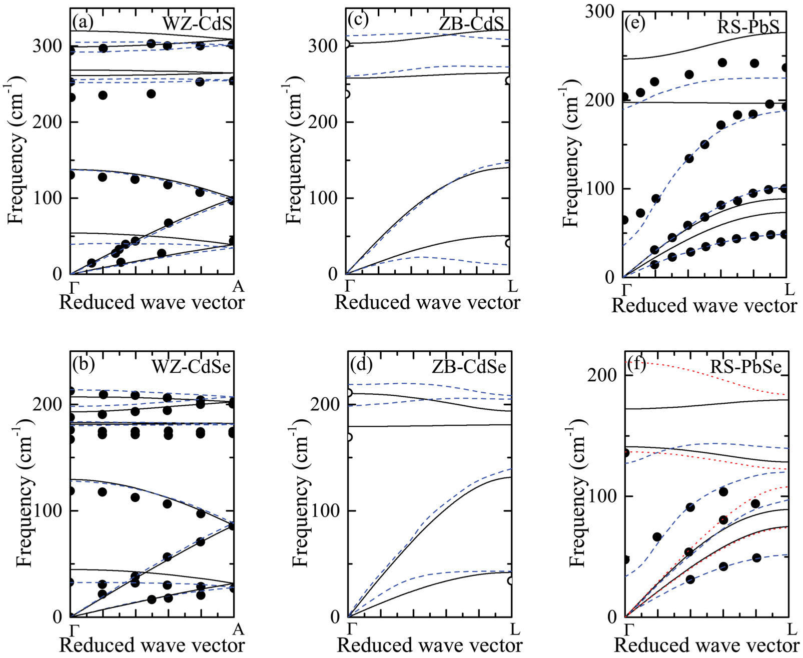

Figure 3.3: Phonon dispersion relations of (a) WZ-CdS, (b) WZ-CdSe, (c) ZB-CdS, (d) ZB-CdSe, (e) RS-PbS, and (f) RS-PbSe. The paths in reciprocal space were chosen as Γ(0, 0, 0) → A(0, 0, 0.5) for the WZ phase and Γ(0, 0, 0) → L(0.5, 0.5, 0.5) for the ZB and RS phase. The black solid lines are the phonon dispersion curves calculated using this force field; the blue dash lines are DFT calculations reported in Refs [241–244]; the circles are experimental data reported in Ref [241, 244–246] and the diamonds are frequencies estimated from the experimental data of WZ-CdX [201]; the red dot lines are calculated using the LJ model for PbSe reported in Ref. [31].

the relative stability of the high-pressure RS phase ($\Delta E_{\mathrm{RS-WZ}}^{\mathrm{SW-CdS}} = 1576$ meV/f.u. and $\Delta E_{\mathrm{RS-WZ}}^{\mathrm{SW-CdSe}} = 1168$ meV/f.u.). Calculated using our new force field model, the relative stabilities of ZB with respect to WZ are 15 and 13 meV/f.u. for CdS and CdSe, respectively, while those calculated by the LJ model [92, 94] are 30 and 27 meV/f.u. for CdS and CdSe, respectively. Both numbers are higher than that computed from DFT ($\Delta E_{\mathrm{ZB-WZ}}^{\mathrm{CdS}} = 2$ meV/f.u. and $\Delta E_{\mathrm{ZB-WZ}}^{\mathrm{CdSe}} = -2$ meV/f.u.). This deviation in our force field or the LJ model [92, 94] can be neglected since the energy differences are less than the thermal energy, $k_{\mathrm{B}}T$.

We further test our transferable force field by reproducing the phonon dispersion relations of WZ-, ZB-CdX and RS-PbX. These vibration properties were not used in the fitting procedures. Figures 3.3a, b, c and d show the calculated phonon dispersion relations for WZ-CdS, WZ-CdSe, ZB-CdS, and ZB-CdSe, respectively.The paths in reciprocal space were chose as Γ → A for the WZ phase and Γ → L for the ZB phase. For WZ-CdX, the calculated phonon dispersion curves are in excellent agreement with the inelastic neutron scattering data [241, 245] and DFT computations [241, 242]. For ZB-CdX, there are no experimental data available for comparison. Only DFT-calculated phonon dispersion relations [243] and a few frequencies at the high symmetrical points estimated from the WZ-CdX measurements [201] can be used for comparison. In general, the phonon dispersion relations calculated for ZB-CdX using this force field are in agreement with the DFT calculations. Figures 3.3 e and f show the calculated phonon dispersion curves in the direction of Γ → L for RS-PbS and RS-PbSe, respectively. Unlike the CdX, the calculated phonon curves for PbX deviate from the experimental data [246] and DFT calculations [244], especially for the optical modes. Accurately reproducing the phonon dispersions for lead chalcogenides is extremely difficult for the existing classical force fields. Consider for example, the phonon dispersions of RS-PbSe that are also calculated by the LJ model for PbSe [31] (red dotted lines in Figure 3.3 f). Neither the present force field, nor the LJ model [31] is able to accurately reproduce the optical branch of phonons in PbSe. The same issue is also present for the force fields developed of PbTe [217, 230]. In the fitting procedures, we also attempted to include the frequencies of the optical modes at the Γ point to the training set within this pair potential model to improve the description of the phonon relations. No significantly improved result was found. We suspect that only using two-body interactions is insufficient to accurately describe the vibrations of the atoms in lead chalcogenides.

3.4 Physical Properties of Mixed Phases

So far, we have demonstrated that the new transferable force field is able to accurately reproduce several physical properties of CdS, CdSe, PbS, and PbSe binary compounds. We expect that this transferable force field will also describe well mixed phases of these four binary compounds. We emphasize that three assumptions were made for the transferability in this model: (1) the same absolute value of the effective charge was used for all ions; (2) short-range interatomic interactions between cations were ignored; (3) the same parameters of short-range interatomic interactions between anions were used for different materials. The parameters for the cross term (short-range S-Se interaction) were obtained by fitting to DFT-calculated lattice parameters and stabilities of different QMPs. If these assumptions are reasonable, we should be able to use this force field to compute some basic physical properties of the mixed phases that are in agreement with the experimental and DFT data.

Table 3.6 lists the lattice parameters and relative stabilities of different QMPs (WZ'-, ZB'-, RS'-Cd_2SSe and RS'-, ZB'-, and HC'-Pb_2SSe) calculated by this force field. A comparison is made with the values calculated by DFT and the LJ model of Ref. [94] (only available for Cd_2SSe). Note that in the LJ model [94], the Lorentz-Berthelot mixing rules were used to obtain the parameters for all cross terms. Since the DFT data were used in the training set to obtain the parameters of the cross terms, our force field is able to more accurately reproduce the DFT results in comparison to the LJ model [94].

In the general case, the cations or anions in mixed phases are more

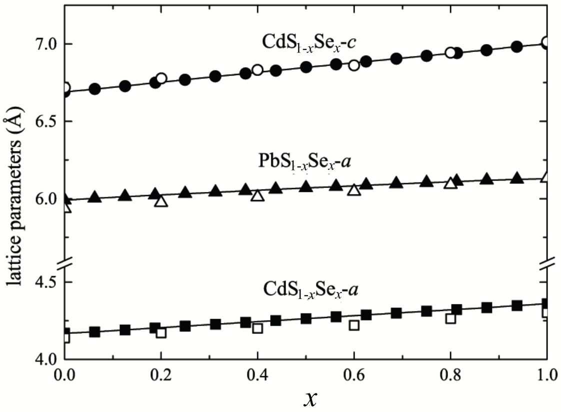

Figure 3.4: Lattice parameters of CdS$_{1-x}$Se$_x$ and PbS$_{1-x}$Se$_x$ calculated from the MD simulations as a function of the fraction x using our new force field. The circles and the squares are the lattice parameter c and a in WZ-CdS$_{1-x}$Se$_x$, respectively; the triangles are the lattice parameter c in RS-PbS$_{1-x}$Se$_x$. The solid symbols are from the MD simulations and the open symbols are experimental measurements reported in Refs. [247, 248].

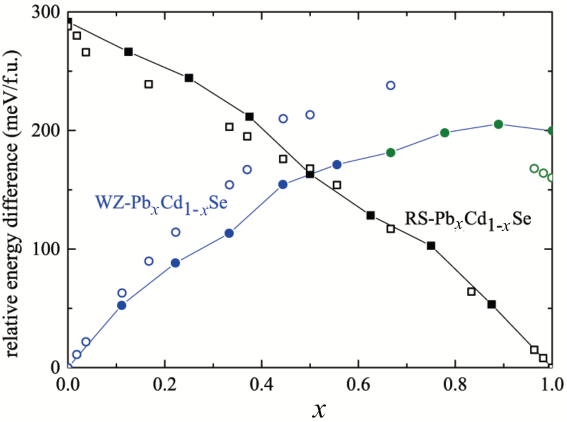

Figure 3.5: Relative energy difference for the WZ- and RS-Pb$_x$Cd$_{1-x}$Se mixed phases as a function of x at 0 K. The circles are WZ-Pb$_x$Cd$_{1-x}$Se with increasing x from 0 to 1; the squares are RS-Pb$_x$Cd$_{1-x}$Se with decreasing x from 1 to 0. The solid symbols are calculated using the force field and the open symbols are DFT data reported in Ref. [35]. The colors black, blue and green indicate the RS, WZ and HC structures, respectively.

Table 3.6: Lattice parameters and relative stabilities of Cd_2SSe and Pb_2SSe quasi-mixed phases (QMPs) calculated using the present force field and the LJ models of Ref. [94], in comparison with DFT data. The lattice parameters a and c are in Å; the relative energy difference ΔE is in eV/f.u.. The number 0 indicates the most stable phase among different structures. The lattice parameters from DFT calculations are normalized by rescaling their volumes. The values in bold are data used for the fit of the force field parameters.

	RS'[a]			ZB'[a]			WZ'[a] or HC'[a]		
	a	c	ΔE	a	c	ΔE	a	c	ΔE
Cd_2SSe									
DFT, this work	**5.52**	**5.52**	**0.298**	**5.95**	**5.96**	**0**	**4.21**	**6.88**	**0.004**
PCRIM, this work	5.53	5.54	0.299	5.94	5.94	0.005	4.22	6.81	0
LJ model[b]	5.61	5.57	0.134	6.00	5.96	0.018	4.28	6.78	0
Pb_2SSe									
DFT, this work	**6.04**	**6.04**	**0**	**6.69**	**6.68**	**0.354**	**5.06**	**6.05**	**0.158**
PCRIM, this work	6.02	6.02	0	6.79	6.69	0.363	5.13	5.99	0.193

[a] The prime symbols on the abbreviations of the structures denote the distortion and the reduced symmetry of the structures by replacing S with Se. See text and Figure 3.1; [b] Calculated using the LJ model reported in Ref. [94]

randomly distributed than in the QMPs in our DFT calculations. The chalcogenides with the same cation have the same crystal structure and similar lattice parameters. Therefore, their mixed phase forms continuous solid solution within a wide temperature range [247, 248]. MD simulations were used to reproduce the lattice parameters of WZ-$CdS_{1-x}Se_x$ and RS-$PbS_{1-x}Se_x$ with different values of x from 0 to1. In the MD simulations, the WZ-CdS and RS-PbS matrixes were used as the initial configurations, and in each MD simulation 1/16 of the total number of S were randomly selected and replaced with Se. Thus the rate at which the ions were exchanged was approximately 30 anions per 500 ps. As expected, WZ-$CdS_{1-x}Se_x$ and RS-$PbS_{1-x}Se_x$ mixed phases formed solid solutions within the range of x from 0 to 1. $CdS_{1-x}Se_x$ remained WZ while $PbS_{1-x}Se_x$ remained RS. No phase transition or (local) structural distortion was found in the simulations. Figure 3.4 shows the relative lattice parameters of WZ-$CdS_{1-x}Se_x$ and RS-$PbS_{1-x}Se_x$ as function of x, which are in good agreement with experimental results [247, 248].

In contradiction to the chalcogenides with the same cations, those with the same anions but different cations have different crystal structures. A six-fold ↔ four-fold phase transition should be observed in WZ-$\mathrm{Pb}_x\mathrm{Cd}_{1-x}\mathrm{X}$ (x: 0→1) and RS-$\mathrm{Pb}_x\mathrm{Cd}_{1-x}\mathrm{X}$ (x: 1→0) with increased/decreased fraction of Pb. This two-way phase transitions are difficult to be directly observed in bulk materials but have been observed in heteronanostructures that were initiated by cation exchange [23, 35]. For this type of mixed phases, no additional parameter is needed for the force field. The transferability of the force field for describing the interatomic interactions between Cd and Pb is based on the assumption that the interatomic interactions between cations are only Coulomb interactions.

We first compare the zero-temperature results by lattice statics simulations to available DFT data [35]. In the lattice statics simulations, 2×2×3 (36 atoms) and 2×2×2 (32 atoms) superlattices were constructed for WZ-CdSe and RS-PbSe as initial configurations, respectively. For each simulation, 4 randomly selected cations (either Cd in WZ-CdSe or Pb in RS-PbSe) were replaced by the other type of cations and a full geometrical relaxation was preformed for the superlattice. A simulation continued until all cations in a superlattice were replaced by the other type. Therefore, the lattice energies of the WZ- or RS-$\mathrm{Pb}_x\mathrm{Cd}_{1-x}\mathrm{Se}$ mixed phases with different fractions of x, can be obtained. At zero temperature and zero pressure conditions, the Gibbs Free energy equals the lattice energy, $G = E$. Therefore, the relative energy difference for a particular fraction of Pb can be calculated as [35]:

$$\Delta E_{\mathrm{Pb_xCd_{1-x}Se}} = E_{\mathrm{Pb_xCd_{1-x}Se}} - xE^{\mathrm{RS}}_{\mathrm{PbSe}} - (1-x)E^{\mathrm{WZ}}_{\mathrm{CdSe}} \tag{3.2}$$

Where $E^{\mathrm{RS}}_{\mathrm{PbSe}}$ and $E^{\mathrm{WZ}}_{\mathrm{CdSe}}$ are the lattice energies of RS-PbSe or WZ-CdSe. The calculated relative energy differences for WZ-$\mathrm{Pb}_x\mathrm{Cd}_{1-x}\mathrm{Se}$ (x: 0→1) and RS-$\mathrm{Pb}_x\mathrm{Cd}_{1-x}\mathrm{Se}$ (x: 1→0) are shown in Figures 3.5. The values calculated by the force field are in reasonable agreement with the available DFT data [35]. Both calculations predict an automatic WZ-to-HC structural transition in WZ-$\mathrm{Pb}_x\mathrm{Cd}_{1-x}\mathrm{Se}$ with increasing fraction of Pb. This structural transition only took place when x→1 according to DFT calculations, but is found to be a gradual transition in the range of $x = 0.6{\sim}1$ using the force field. The calculated relative energy differences at 0 K are all positive indicating a complete phase separation of PbSe and CdSe.

To reproduce the concentration-induced six-fold ↔ four-fold phase transition in the $Pb_xCd_{1-x}X$ mixed phases, four independent MD simulations were carried out: WZ-$Pb_xCd_{1-x}X$ with $x = 0 \rightarrow 1$ and RS-$Pb_xCd_{1-x}X$ with $x = 1 \rightarrow 0$. The method mentioned earlier in the text was used to replace cations. The rate at which the ions were exchanged was also kept at $\sim$30 cations per 500 ps. This exchange rate is larger than in experiments [35] (typically a few minutes for a complete cation exchange of a 20-nm-sized NC), but it is slow enough to observe phase transitions in the MD simulations. Apparently, using this artificial cation exchange, the MD simulations by no means are able to reveal the mechanisms of the real cation exchange phenomenon. We here only show the occurrences, possible routes and mechanisms of these phase transitions initiated by cation exchange. We used a relatively high temperature (T = 500 K) for these MD simulations. The DFT computations of the relative stability of the ternary systems at zero temperature and a rough estimation considering the configurational entropy indicated that at relatively low temperatures ($T \leq$ 300 K), a mixed phase is thermodynamically not favored over phase separation. A relatively high temperature is required to enable the $Pb_xCd_{1-x}X$ ternary systems to form mixed phases. A high temperature also provides the activation energy to cross energy barriers and therefore the phase transitions can be easily detected within a relatively short MD simulation time.

Figure 3.6 shows typical snapshots of the four MD simulations at the transition concentrations. A WZ-to-RS phase transition (Figure 3.6 a was found as expected in the WZ-$Pb_xCd_{1-x}S$ system at $x = 1/2$, but, unexpectedly, the WZ-$Pb_xCd_{1-x}Se$ was trapped in a metastable HC phase (Figure 3.6 b from $x = 3/8 \sim 1$). We feel that a higher temperature or a longer simulation time may enable the $Pb_xCd_{1-x}Se$ ($x \geq 0.5$) mixed phase to leap from the metastable HC phase to the stable RS phase, since such transformation involves activated nucleation events [93]. Surprisingly, the MD simulations starting from RS-$Pb_xCd_{1-x}S$ and RS-$Pb_xCd_{1-x}Se$ (x: $1 \rightarrow 0$) also yielded different results. The RS-$Pb_xCd_{1-x}Se$ mixed phase transform to the WZ structure at x=3/4 (Figure 3.6 c), while the x=1/2 (Figure 3.6 d). How-

(a) Pb$_x$Cd$_{1-x}$S (x: 0→1)

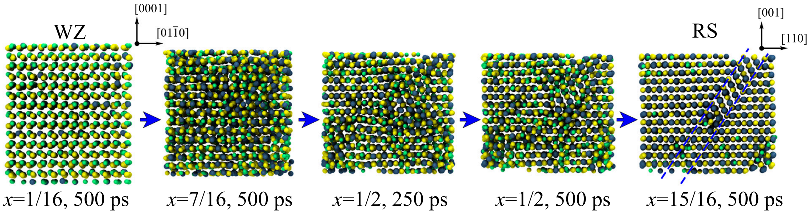
WZ
[0001]
[01$\bar{1}$0]
RS
[001]
[110]
x=1/16, 500 ps
x=7/16, 500 ps
x=1/2, 250 ps
x=1/2, 500 ps
x=15/16, 500 ps

(b) Pb$_x$Cd$_{1-x}$Se (x: 0→1)

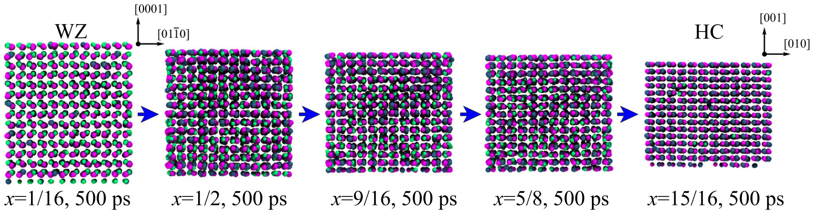
WZ
[0001]
[01$\bar{1}$0]
HC
[001]
[010]
x=1/16, 500 ps
x=1/2, 500 ps
x=9/16, 500 ps
x=5/8, 500 ps
x=15/16, 500 ps

(c) Pb$_x$Cd$_{1-x}$S (x: 1→0)

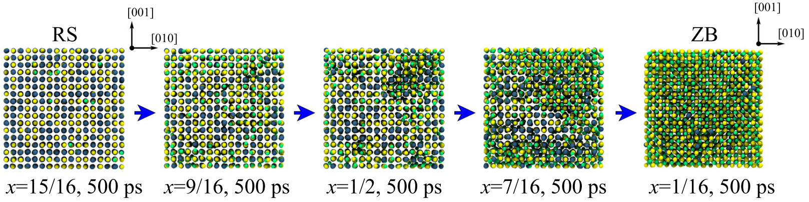
RS
[001]
[010]
ZB
[001]
[010]
x=15/16, 500 ps
x=9/16, 500 ps
x=1/2, 500 ps
x=7/16, 500 ps
x=1/16, 500 ps

(d) Pb$_x$Cd$_{1-x}$Se (x: 1→0)

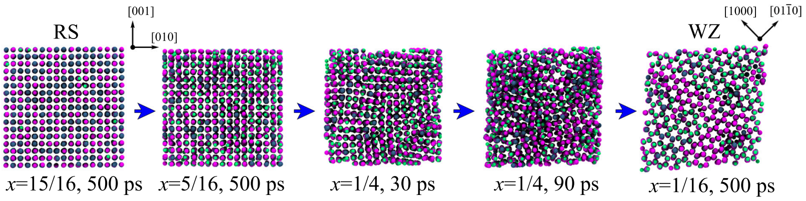
RS
[001]
[010]
WZ
[1000]
[01$\bar{1}$0]
x=15/16, 500 ps
x=5/16, 500 ps
x=1/4, 30 ps
x=1/4, 90 ps
x=1/16, 500 ps

Figure 3.6: Snapshots of MD simulations of (a) WZ-Pb$_x$Cd$_{1-x}$S (x: 0→1), (b) WZ-Pb$_x$Cd$_{1-x}$Se (x: 0→1), (c) RS-Pb$_x$Cd$_{1-x}$S (x: 1→0), and (d) RS-Pb$_x$Cd$_{1-x}$Se (x: 1→0) ternary mixed phases at 500 K. The green, blue, yellow, and purple spheres represent Cd, Pb, S, and Se atoms, respectively. For each system, the first and the last snapshots show the final configurations with the lowest and highest fractions of exchanged cations, respectively; the second to the forth snapshots show the configurations when the phase transitions are taking place. The blue dash lines at the upper right of the figure indicate twin boundaries in the RS-Pb$_{15/16}$Cd$_{1/16}$S.

ever, both results are acceptable since the WZ and ZB phases for CdX have very similar stabilities and the transition routes are expected to be highly sensitive to the temperature, the initial configuration, nucleation energies, energy barriers to transform from one phase to another, the rate at which the cations are exchanged, etc. Very recently, it was reported that both the RS-to-ZB and partially RS-to-WZ transitions are found by a cation exchange (Pb→Cd) process in RS-PbSe 2D-superlattices [23].

3.5 Surface Energy Calculations

Using this force field, the surface energies of several different non-polar surfaces of WZ-CdX and RS-PbX were calculated and were compared with the results calculated by the LJ models [31, 92, 94] and by DFT. For the WZ-CdX, the $\{10\bar{1}0\}$ and $\{11\bar{2}0\}$ surfaces were considered while for RS-PbX, the $\{100\}$ and $\{110\}$ surfaces were considered. These non-polar surfaces are the most important surfaces for WZ-CdX and RS-PbX having the lowest surface energies. Polar surfaces as WZ-$\pm\{0001\}$ and RS-$\pm\{111\}$ are also important, but the stabilizing mechanisms are complicated and can differ between different materials or between different terminated atoms (*i.e.* cation-terminated, anion-terminated, or reconstructed polar surfaces) [82, 219, 249–251]. Surfaces energies of those polar surfaces calculated by DFT and by classical force fields are normally in the same order of magnitude [68, 82]. However, DFT and classical force fields in general use very different schemes to calculate polar surfaces [82], thus the comparison between them is difficult and less meaningful. Therefore, we omit the calculations and discussions of the polar surfaces. For the details about the DFT and classical computations of surface energy, we refer to our previous work [82].

Table 3.7 shows the calculated surface energies by the present PCRIM, the LJ models [31, 92, 94], and DFT for CdX and PbX, respectively. We expect that the materials with the same cations have similar surface properties, since they have the same structures and the very similar physical properties. However, the DFT results for CdSe reported by Manna *et al.* [250] and Csik *et al.* [252] are very different from those for CdS reported

Table 3.7: Surface energies of the most stable non-polar surfaces for CdX and PbX calculated with the present force field, the LJ models of Refs. [31, 94], and by DFT, together with available DFT data in literature. The surface energies are in J/m^2.

	surface	PCRIM, this work	LJ model [a]	DFT, this work	DFT, literature
WZ-CdS	$\{10\bar{1}0\}$	0.29	0.42	0.323	0.28 [b]
	$\{11\bar{2}0\}$	0.30	0.44	0.318	0.29 [b]
WZ-CdSe	$\{10\bar{1}0\}$	0.25	0.35	0.237	0.46[c], 0.59[d]
	$\{11\bar{2}0\}$	0.26	0.37	0.231	0.50[c], 0.67[d]
RS-PbS	{100}	0.29	-	0.178	0.160[e]
	{110}	0.49	-	0.327	-
RS-PbSe	{100}	0.29	0.33	0.179	0.184[f]
	{110}	0.49	0.67	0.316	0.318[f]

[a] Calculated using the LJ models reported in Refs. [31, 94]; [b] Ref. [249]; [c] Ref. [252]; [d] Ref. [250]; [e] Ref. [251]; [f] Ref. [219].

by Barnard *et al.* [249]. The former are almost two times larger than the latter. The authors from the last paper suggested that the difference may be due to the different schemes used in the DFT calculations and/or the different materials studied. We performed the DFT-GGA calculations for both CdS and CdSe. It turns out that our results for CdS are similar to those reported in Ref. [249] and the values for CdSe are slightly smaller than those for CdS. In our DFT calculations, we used the same basic settings with considerably high accuracy for all materials, which indicates that the surface properties for CdS and CdSe are indeed similar and these significant differences from former DFT calculations are likely due to the different computational methods used. Similarity is also found between the surfaces of PbS [251] and of PbSe [219].

The surface energies for CdX and PbX calculated by our force field are in reasonable agreement with our DFT calculations. The calculated surface energies of the {001} facet of PbX (~0.29 J/m^2) are slightly higher than the DFT results (~0.18 J/m^2). For WZ-CdX, the two most stable surfaces, $\{10\bar{1}0\}$ and $\{11\bar{2}0\}$, have very similar surface energies, which dominate the morphologies of the WZ-CdX nanostructures (*e.g.*, WZ-CdX NCs normally form spheres and rods). For RS-PbX, the {100} facet has the lowest surface energy, thus PbX NCs easily form cubes or truncated cubes.

3.6 Conclusions

We derived a transferable force field for the CdS-CdSe-PbS-PbSe systems. This Partially Charged Rigid Ion Model contains only two-body interatomic interactions and 22 parameters. This new force field has simple functional forms but equivalent or better descriptions of several physical properties of CdX and PbX in comparison to other models. The physical properties of CdX and PbX including the crystalline structures, elastic constants, bulk moduli, relative stability, transition pressures, phonon dispersion relations, and the surface energy can be described by this force field with considerably high accuracy. This force field is also able to describe the MS_xSe_{1-x} and $Cd_xPb_{1-x}X$ ternary systems. The former forms continuous solid solutions while concentration-induced four-fold (WZ or ZB) $\leftrightarrow$ six-fold (RS) transitions were found in the latter by changing the fraction of the cations. A classical force field can never be prefect and one should be aware of its limitations. Here, we also summarize the shortcomings for this force field: (1) According to our DFT-GGA calculations, the stability of the HC phase is slightly overestimated and that of the ZB phase is slightly underestimated for CdX; (2) Due to the simplification of this PCRIM, several physical properties can not be accurately reproduced for CdX and/or PbX, including the cohesive energies and melting points for CdX and PbX, and the phonons in RS-PbX. The melting points of WZ-CdS, WZ-CdSe, RS-PbS, and RS-PbSe assessed by direct heating MD simulations [82] are 1137, 1088, 1665, and 1608 K, respectively. The experimentally measured melting points [201, 203] are 1748, 1512, 1383, and 1353 K for WZ-CdS, WZ-CdSe, RS-PbS, and RS-PbSe, respectively. Note that the force field was not tuned to reproduce experimental melting points; (3) The calculated surface energies of the 001 facet of PbX are slightly higher than the DFT results. The charge transfer on the polar surfaces of the CdX and PbX cannot be described by the rigid ion model. This transferable force field for the CdS-CdSe-PbS-PbSe systems is expected to be used in the classical molecular simulations to investigate many burgeoning researches in material science such as solid-solid phase transitions, the seeded growth mechanism, oriented attachment, and cation exchange of NCs, which are of interest for the further development of functional chalcogenide nanostructures.

Chapter 4

Thermally Induced Transformation of CdSe Nanocrystals

This chapter is based on the paper: Z. Fan, A. O. Yalcin, F. D. Tichelaar, H. W. Zandbergen, E. Talgorn, A. J. Houtepen, T. J. H. Vlugt, and M. A. van Huis, 'From Sphere to Multipod: Thermally Induced Transitions of CdSe Nanocrystals Studied by Molecular Dynamics Simulations', J. Am. Chem. Soc., 2013, ***135****, pp 5869–5876.*

4.1 Introduction

Cadmium selenide (CdSe) is a II-VI group semiconductor which has been widely studied [201]. There are three known structures of CdSe: wurtzite (WZ), zinc blende (ZB) and high-pressure rock salt (RS). Theoretical studies [253] showed that the WZ and ZB CdSe bulk materials have very similar energies at zero temperature and zero pressure, and in practice both WZ and ZB bulk CdSe are stable at relatively low temperatures [254]. CdSe nanocrystals (NCs) are studied extensively as a model system, as they show tunable optical and electronic properties depending on their size [5, 255]. Therefore, the size-, shape- and structure-controlled synthesis of the CdSe nanocrystals has become an important research area [17, 197, 256, 257]. Special attention has been paid to heterostructural nanocrystals [258] (HSNCs) such as branched nanocrystals[19, 20, 259–266], due to their novel and complex morphologies and the potential application in optoelectronic devices. In 2003, Manna *et al.* [259] reported the synthesis of CdTe nanocrystals with a tetrapod shape. Since this discovery, several other types of nanotetrapods consisting of different compounds and using various synthesis methods have been reported [19, 260–262]. II-VI and IV-VI semiconductor nanocrystals having an octapod morphology have also been reported recently [20, 263–266]. These multipod morphologies contain a ZB tetrahedral or octahedral core and the WZ legs are grown on the surfaces of the ZB cores along the ±<0001>direction.

The crystal and electronic structure as well as mechanical, thermodynamic and vibrational properties of bulk CdSe have been systematically studied by means of density functional theory (DFT) calculations [243, 253, 267, 268]. Wang *et al.* [269] have studied the geometries and electronic structure of CdSe surfaces using the tight-binding method. The passivation of CdSe surfaces by ligands and the binding energies of ligands were calculated by DFT [250] and molecular simulations [270] respectively. In addition, much research has been conducted on the pressure-induced WZ-to-RS phase transition [93, 184, 233, 271, 272]. One of the most important studies was done by Grünwald *et al.* [93] who successfully simulated the WZ-to-RS phase transition in CdSe NCs using molecular dynamics (MD) simulations with a classical forcefield for CdSe first developed by Rabani [92]. The mechanism of this pressure-induced phase transition is somewhat controversial as the metastable intermediate h-MgO phase found in the MD simulations has not been observed experimentally. In contrast to the pressure-induced transformations, little is known on the effect of temperature on CdSe nanostructures.

In this work, we used MD simulation to predict a thermally induced sphere-to-multipod morphological transition in CdSe NCs mediated by local

ZB-to-WZ phase transformations. The MD simulations show that an uncapped spherical CdSe NC with ZB structure transforms to a nanotetrapod or a nanooctapod upon heating. Below we will compare our results with in-situ heating experiments performed in the high resolution transmission electron microscope (HR-TEM), whereby similar nanotetrapods were observed. The MD simulations reveal the vacancy-assisted mechanism of the WZ-to-ZB transition and indicate that the final morphology is temperature and size dependent.

4.2 Methods

4.2.1 Molecular Dynamics Simulation

The empirical pair potential of CdSe developed by Rabani [92] was used to describe the interactions between atoms. The pair potential consists of two parts: Coulombic interactions and a short-ranged Lennard-Jones potential. We chose Rabani's potential because of its simplicity and effectiveness, which was demonstrated by several simulation studies [93, 184, 271, 272] on CdSe materials. We further investigated the validity of the interaction potential at high temperatures and the capability of the interaction potential to describe surface properties. The lattice parameters of bulk CdSe for both the WZ and ZB phases were calculated for temperatures ranging from 300 to 1000 K by MD simulations. The results show that, except for the overestimation of the thermal expansion coefficient [180], Rabani's potential leads to quite accurate predictions for the lattice parameters of the CdSe bulk materials at high temperatures. The differences between MD simulations and X-ray diffraction experiments [180] are less than 4%. Also, the surface energies calculated by the LS simulation are in good agreement with DFT results.

Three ZB CdSe nanosphere models were constructed with radii of 1.8, 2.3 and 2.8 nm containing 880, 1720 and 3028 atoms respectively. A WZ CdSe nanosphere (radius 1.8 nm, 882 atoms) was also constructed. All nanosphere models are isolated in vacuum without surfactants. In the MD simulations of CdSe NCs, the equations of motion were integrated using the velocity Verlet algorithm with a timestep of 1 fs. The temperatures were controlled by the Nose-Hoover thermostat [63]. The CdSe nanosphere models were constructed by cutting a sphere from a bulk CdSe crystal. As we study isolated NCs in vacuum, no periodic boundaries were applied. The electrostatic interactions were calculated by taking into account all atom pairs, and the short-ranged Lennard-Jones interaction was truncated and shifted at 10 Å. MD simulations of 30 ns were performed for all systems, out of which the first 3 ns were used to equilibrate configurations.

4.2.2 Synthesis of CdSe Nanocrystals

Following an adapted recipe of Mekis *et al.* [273], two precursors were prepared in a N_2 purged glovebox by dissolving 0.474 g Se (325 mesh) in 6 ml TOP (trioctylphosphine) and 0.36 g $Cd(Ac)_2$ in 9 ml TOP, respectively. Subsequently, the following synthesis was done in a Schlenk line to provide oxygen- and water-free conditions. Specifically, 24 g of TOPO (Trioctylphosphine oxide) was heated to 180 °C in vacuum under periodic flushing with N_2. After cooling down to 100 °C, 15 g HDA (1-hexadecylamine) and 0.45 g TDPA (1-tetradecylphosphonic acid) were added and dried at 120 °C in vacuum during 30 min under periodic flushing with N_2. The TOP-Se precursor was injected and the solution was heated to 300 °C under N_2 flow. Under vigorous stirring, the TOP-$Cd(Ac)_2$ precursor was injected to induce nucleation of CdSe nanoparticles. During the growth at 280 °C aliquots were taken to monitor the growth rate. After 550 s the reaction was stopped by cooling down the remaining reaction volume to room temperature. At 55 °C 30 ml of toluene was injected to avoid solidification of the TOPO. The obtained dispersion was purified by repeated washing with MeOH and precipitation of particles in a centrifuge at 3000 rpm for 5 min. The final stock of particles was dispersed in Chloroform.

4.2.3 TEM In-situ Heating Experiments

Heating experiments were conducted in-situ in the transmission electron microscope (TEM) on CdSe NCs with a diameter of about 6 nm. The NCs were dropcast onto MEMS microheaters with SiN electron-transparent viewing windows, which enables atomic-resolution imaging while heating inside the TEM [44]. A Cs-aberration-corrected cubed Titan TEM was used operating at 300 kV.

4.3 Results and Discussion

4.3.1 Sphere-to-Tetrapod Transformation

Figure 4.1 (a) and Supporting Movie M1 in Ref. [68] show the time evolution of ZB spherical $Cd_{440}Se_{440}$ NC at 800K during 30 ns. Surface reconstruction takes place at the start of the simulation: the surface becomes angular and rugged. Despite the thermal motion of the atoms, it is still possible to investigate the local crystalline order. The first two outermost bilayers transform from the ZB structure to the WZ structure in 3 ns. Here, we define a bilayer as a {CdSe} pair of nearest WZ {0001} planes or a {CdSe} pair of nearest ZB {111} planes. From 7 to 10 ns, the ZB-to-WZ transition also takes place in the third outermost bilayer (Fig. 4.1 (a)) of the NC. No clear local structural transition is then observed until the end of the MD simulation. After 20 ns, the $Cd_{440}Se_{440}$ NC reaches a relatively stable configuration. During the 30 ns MD simulation, the structure of the NC transforms from purely ZB to heterostructural whereby the interface between the ZB and WZ domains is along the WZ{0001}/ZB{111} atomic planes.

To visualize the transition, different parts of the tetrapod are shown separately in Fig. 4.1 (b): the WZ domains are displayed separately from the ZB core towards the (0001) direction. The heated ZB $Cd_{440}Se_{440}$ NC exhibits a distinct tetrapod morphology with a ZB core and four short WZ legs. The lengths of the four WZ legs differ: the longest one contains four bilayers and the shortest one contains only two. We always count the bilayer at the boundary of the ZB and the WZ domains as in the WZ structure. The ZB core has a tetrahedral morphology, and the four WZ legs are connected onto the four ZB Cd-terminated {111} facets of the tetrahedral core.

Before elaborating on the structural details of the nanotetrapod, we first mention the simulation result for the spherical *wurtzite* $Cd_{441}Se_{441}$ NC which

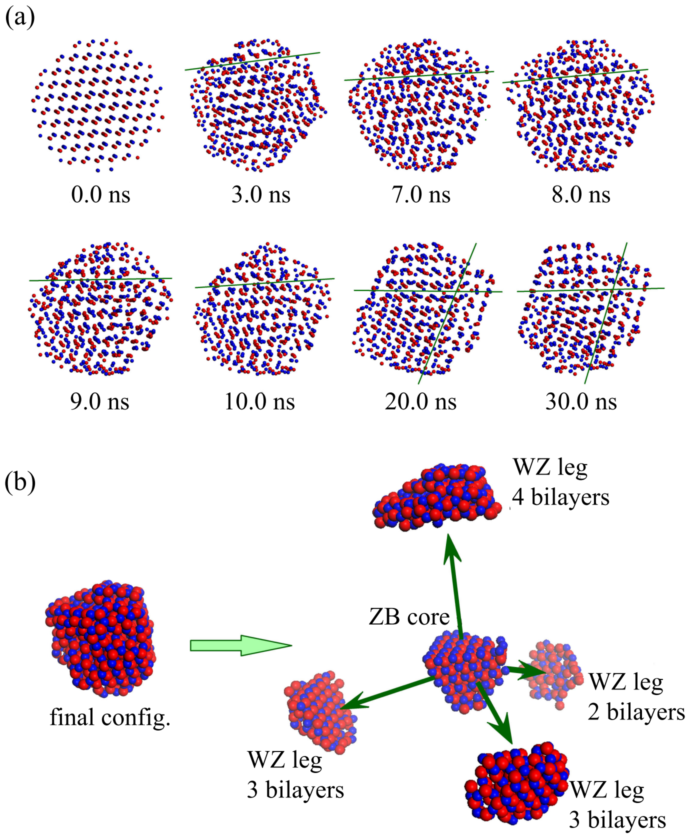
(a)
0.0 ns
3.0 ns
7.0 ns
8.0 ns
9.0 ns
10.0 ns
20.0 ns
30.0 ns
(b)
WZ leg
4 bilayers
ZB core
final config.
WZ leg
2 bilayers
WZ leg
3 bilayers
WZ leg
3 bilayers

Figure 4.1: (a) Snapshots of $Cd_{440}Se_{440}$ NCs from MD simulations at 800 K. Surface atoms show structural rearrangements after 3 ns. From 7 to the 9 ns, a local ZB-to-WZ transition takes place on the third outermost bilayer. The green line on the snapshot at 3 ns indicates a boundary betweeen the second and the third outermost ZB$\{111\}$/WZ$\{0001\}$ bilayer; the green lines on the snapshots at 7, 8, 9 and 10 ns indicate the boundaries between the third and the fourth outermost bilayers; the green lines on the snapshots at 20 and 30 ns indicate the boundaries between the WZ and the ZB domain. (b) Deconstruction of the final configuration (a tetrapod morphology with one ZB core and four short WZ legs). In all snapshots, the blue and red spheres are Cd and Se atoms, respectively.

leads to very different results. A local structural transition from the WZ structure to a body-centered-tetragonal structure (BCT) is observed. This transition was also found and studied in previous molecular simulations and DFT calculations for CdSe and other II-VI semiconductor nanostrucutres and bulk materials [74, 78, 80, 274, 275], and recently it was observed directly in ZnO nanoislands by aberration-corrected TEM [77]. During the simulation, the morphology of the WZ $Cd_{441}Se_{441}$ NC changes from spherical to rod-like, as shown in Figure S2 of the Supporting Information of Ref. [68].

The structural transition of the *zinc blende* NC can be quantified by local bond order parameters [276]. Local bond order parameters preserve the information of the local structure by symmetry analysis and are commonly used to distinguish among different crystal structures and the liquid phase[277, 278]. Detailed information about the definition of the local bond order parameters is presented in the Supporting Information of Ref. [68]. Here, the order parameter q_4 is chosen to monitor the structural evolution and the $q_4 - q_6$ plane is used to distinguish the ZB and the WZ structures. Either all Cd atoms or all Se atoms are removed from the $Cd_{440}Se_{440}$ NC, so that cationic and anionic sublattices are obtained. Both sublattices are face-centered cubic (fcc) in the ZB phase and hexagonal close packed (hcp) in the WZ phase. Atoms at the surfaces are considered separately from the atoms inside the NC, as the local structure of surface atoms cannot be evaluated precisely by bond order parameters based on nearest neighbor analysis. The surface atoms are distinguished by counting the numbers of the nearest neighbors for each atom in the Cd or Se sublattices; an atom is defined as a surface atom if the number of nearest neighbors is less than 9 and the atoms are defined to be nearest neighbors if their interatomic distance is less than 5.4 Å. We define a "core zone" consisting of all atoms within 0.8 nm of the center of the NC and a "shell zone" consisting of all atoms outside a sphere with a radius of 1.1 nm. Using this division, the atoms in the ZB core and in the WZ legs can be distinguished effectively. The atoms at the ZB/WZ boundaries are thereby not included in our analysis. As a reference, we first calculated the averaged values of q_4 for fcc and hcp structures in CdSe bulk materials at 800 K. $q_{4-fcc} = 0.190$ and

$q_{4-hcp} = 0.097$ at 800 K. The values of the order parameters q_4 and q_6 in the Se_{440} and Cd_{440} sublattices were calculated as a function of time. A fixed value of $q_4 = 0.4$ was allocated to surface atoms.

In Fig. 4.2 (a), simulation snapshots of the Se sublattice colored by q_4 show the structural evolution of the NC. At 0 ns, the color of most of the atoms, except for the surface atoms, are green corresponding to $q_4 \approx 0.2$, which indicates an initial fcc structure of the sublattice. During the MD simulation, more and more atoms on the edge turn to red corresponding to a decrease of q_4 to 0.13. After 9 ns, two layers of red atoms on the lower right part of the Se sublattice section are observed, coinciding with the longest WZ leg that has four WZ bilayers. In Fig. 4.2 (b), the averaged q_4 with respect to all the same atoms (either Cd or Se) at a certain zone (either the "core zone" or the "shell zone") are plotted as a function of time. The plots of the averaged values of q_4 for Cd and Se atoms in the same zone are overlapping, as the structures of Cd and Se sublattice are approximately identical. The result (Fig. 4.2 (b)) shows that the averaged q_4 of the atoms in the core zone remains nearly constant, coinciding with the fcc structure. This clearly shows that the atoms in the core zone remain in the ZB structure during the simulations. The averaged q_4 of the atoms in the shell zone decreases from 0.165 to 0.125 with relatively large fluctuations, suggesting a ZB-to-WZ structural transition. The q_4-q_6-plane for the Se_{440} sublattice in the core and shell zones are shown in Fig. 4.2 (c). Each data point corresponds to q_4 averaged over all atoms in one zone at a given timestep in the last 15 ns. The fcc structure in the ZB core zone and the hcp structure in the WZ shell zone can thus easily be distinguished.

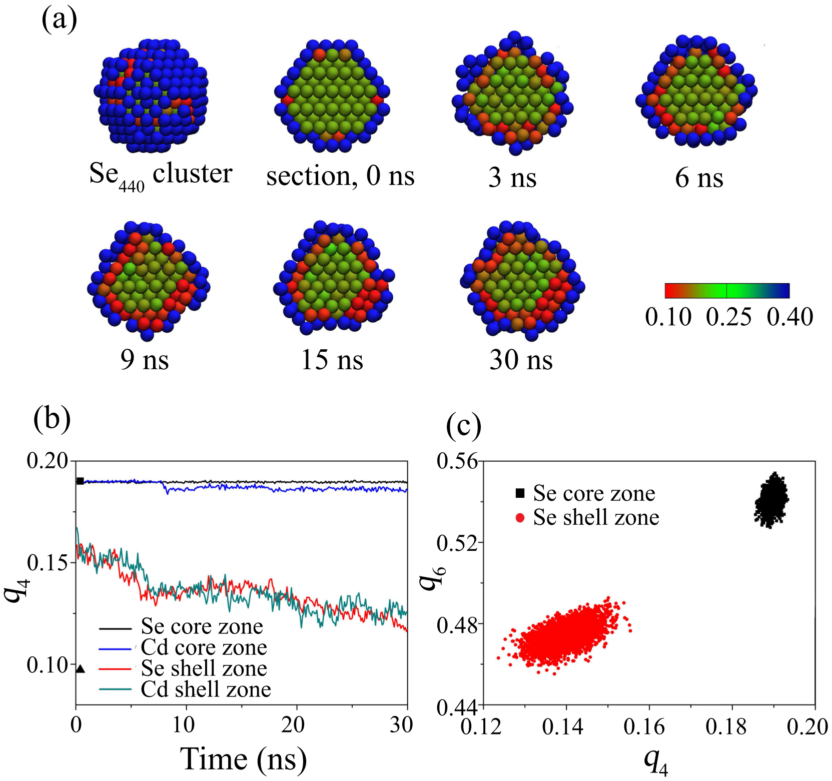

Figure 4.2: (a) Snapshots of the Se$_{440}$ sublattice colored by the value of the bond order parameter q_4 at 800 K. The surface atoms (see the definition in the main text) are given a value of 0.4 in order to not take them into account. (b) Plots of the averaged q_4 respect to all the Se or Cd atoms in one zone (see the definitions of the "core zone" and "shell zone" in the main text) as a function of time, fluctuating due to thermal vibrations. The black square and the black triangle indicate the referenced ideal values of q_4 of the fcc and hcp Se sublattice in the CdSe bulk materials at 800 K respectively, where $q_{4-fcc} = 0.190$ and $q_{4-hcp} = 0.097$ at 800 K. (c) The q_4-q_6-plane for the Se$_{440}$ cluster in the "core zone" and the "shell zone". Each point corresponds to the averaged values of q_4 and q_6 for all the atoms in different zones, calculated at a single time.

4.3.2 Atomic-Scale Transition Mechanism

The question now arises: what is the underlying mechanism of the morphological and local structural transitions? From a close inspection of the results, it is clear that the ZB-to-WZ local structural transition starts from the outermost layer, and then proceeds into the inner layers. In our simulation, the first two outermost ZB {111} bilayers change quickly (within 3 ns) into WZ {0001} bilayers, and the transition of the third outermost bilayer starts after approximately 7.5 ns. The snapshots of the third outermost bilayer around the transition provide the essential information (Fig. 4.3); Until 7.60 ns, the Cd and Se atoms in the bilayer are located at the ZB lattice sites, but deformations can be identified at the edge of the plane. From 7.70 ns onwards, several Cd atoms in the central area migrate to the WZ sites assisted by Cd vacancies. After 8.15 ns, the whole Cd layer is shifted from the ZB sites to the WZ sites. It is important to note that the slip (the mutual displacement along a so-called slip plane of the two parts of the structure at either sides of the slip plane) of the Cd layer is very gradual, taking place through a large number of individual atomic jumps, and is greatly assisted by point defects (Cd vacancies). In general, vacancies can be annealed out more easily in a nanocrystal than in a bulk material, since a defect needs to travel a much shorter distance to reach the surface. On the other hand, the surface also acts as a source of vacancies so that defects are easily produced at elevated temperatures. Elevated temperatures also enhance the mobility of the defects, thereby accelerating the process of the ZB-to-WZ transition.

The difference in potential energies between the bulk WZ and bulk ZB CdSe at 0 K is very small: DFT calculations [253] indicate an energy difference of just 2 meV per {CdSe} pair. The potential energies of the nanocrystals are strongly dependent on the morphology. It is difficult to compare the potential energies of the tetrapod with a ZB sphere at 800 K, since a spherical morphology is structurally unstable in the ZB structure at 800 K. However, potential energies can be compared at a lower temperature (200 K), whereby the ZB sphere is metastable. MD simulations of the initial spherical ZB NC were performed at a temperature of 200 K in 20 ns,

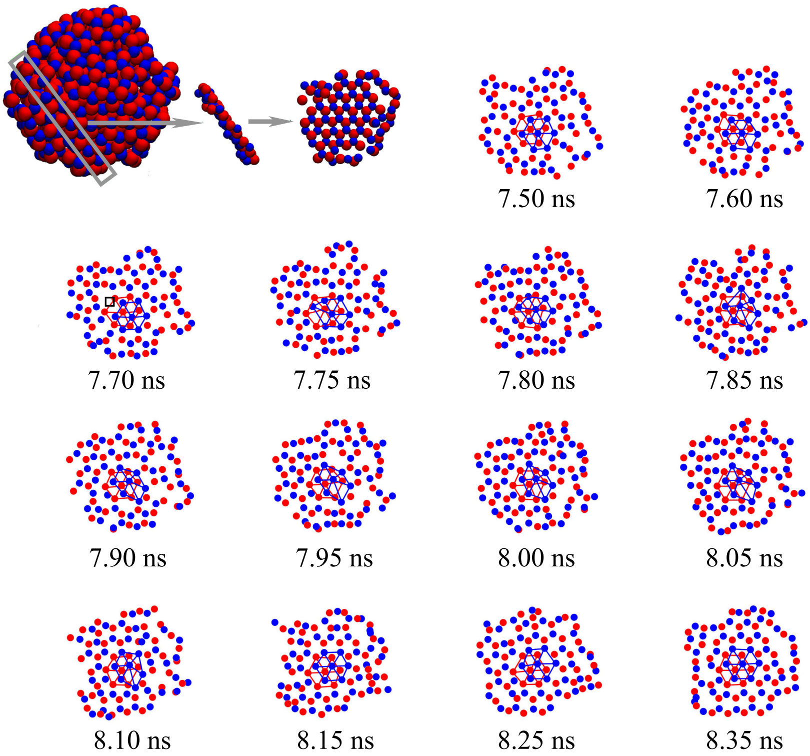

Figure 4.3: Snapshots of one of the third outermost ZB (111) (or WZ(0001)) bilayers from 7.50 to 8.35 ns. The shapshot on the upper left indicates where the bilayer is located in the NC and how it is oriented. Seven Cd and seven Se atoms in the middle of the bilayer are connected with lines to show the deformation of lattice sites during the local structure transition. The black square in the 7.70 ns snapshot indicates one of the Cd vacancies which cause local distortions and assist the ZB-to-WZ local structural transition. The blue and red spheres (dots) are Cd and Se atoms, respectively. Sometimes strings of atoms seem to appear, for example at the right-hand side of the 8.05 and 8.35 ns snapshots. This feature is caused by the presence of a string of vacancies.

whereby the first 4 ns were used to equilibrate the system. At such a low temperature, the configuration retains both a spherical morphology and the ZB structure. Next, the configuration of the heated tetrapod obtained from the MD simulation at 800 K was cooled down to 200 K in 3 steps. At each step the temperature was reduced 200 K and system was equilibrated for 5 ns. At $T = 200$ K, an extended MD simulation of 4 ns was performed. It turns out that the final configuration of the NC at 200 K retains the tetrapod-like shape. The averaged potential energy in the last 4 ns of the tetrapod is 40 meV per {CdSe} pair less than the ZB sphere at 200 K. We therefore conclude that the tetrapod configuration is energetically preferred over the spherical ZB NC configuration.

Surfaces always play an important role in nanocrystals due to the large surface to volume ratio. As mentioned previously, the Rabani CdSe potential describes the surface properties of CdSe materials relatively well. The results of the LS simulations in this work indicate that CdSe WZ $\{11\bar{2}0\}$ and $\{10\bar{1}0\}$ and ZB {110} are the most stable facets with only little differences in surface energy (less than 0.02 J/m^2). The polar surfaces, WZ {0001} and $\{000\bar{1}\}$ and ZB {111} and $\{\bar{1}\bar{1}\bar{1}\}$ facets, are relatively unstable, that is, surface energies of these facets are relatively high. The most unstable surfaces are the ZB Cd-terminated {001} and Se-terminated $\{00\bar{1}\}$ facets. DFT calculations [250] showed that ligands such as methyl phosphoric acid (MPA), methyl amine (MA) or trioctylphosphine oxide (TOPO) can greatly reduce the surface energies of the unstable surfaces on the CdSe NCs. For example, the surface energy of the WZ Cd-terminated (0001) facet passivated by MPA or MA can be reduced from 80 meV/Å^2 (bare surface) to approximately 40 meV/Å^2 (capped surface) which is comparable to the surface energies of the most stable WZ $\{11\bar{2}0\}$ or $\{10\bar{1}0\}$ facets passivated by the same kind of ligand. Using proper ligands, NCs can be synthesized with surfaces that without ligands would be unstable [279]; Evaporating the ligands by heating also activates the unstable surfaces again and causes structural or morphological transitions. Using MD simulations, Schapotschnikow *et al.* [31] showed that after evaporation of the ligands by annealing, a nearly spherical PbSe NC capped by ethylamine surfactants will undergo a morphological transition from multifaceted to cubic at 450 K.

Similarly, the morphological and local structural transitions of the ZB CdSe NC in our simulation could be the consequence of exposing its unstable surfaces to vacuum.

4.3.3 Experimental HR-TEM Results

Strong correspondence was found between the simulation results and the results of the annealing experiments conducted in-situ in the TEM on 6-nm-diameter CdSe NCs. The results are displayed in Fig. 4.4. Directly after dropcasting, deposits of the solution and ligands prevent high-resolution imaging. Shortly after low-temperature annealing at a temperature of 350 K, the high-resolution fringes reveal that the spherical NCs consist of multiple domains, which can be either WZ or ZB. Here, we remark that in the HRTEM images displayed in the reference work for the synthesis, [273] also multiple domains can be distinguished. One spherical NC in Fig. 4.4(a) displays already at this stage a precursor state for transforming into tetrapods: while this NC is nearly spherical, it displays already a ZB core and short WZ legs, and is very similar to the simulation result obtained after 30.0 ns shown in Fig. 4.1. Upon continued annealing for approximately 20 mins at a temperature of 390 K, several NCs transform into tetrapods with more elongated WZ pods, as shown in panel (b) of Fig. 4.4. The schematics in panels (d,e) show the orientation of the tetrapods observed in the experiments, whereby in general two of the pods are lying flat onto the SiN membrane support. Not all spherical NCs transformed into tetrapods: some evolved into single crystals (WZ or ZB), while others formed tripods, bipods or dimers. Supporting Movie M2 in Ref. [68] shows an isolated bipod or tripod at an elevated temperature of 400 K, which was followed in time during 3 minutes. Small changes are observed in the arrangement of atomic planes (width, occupancy) and in the overall morphology. These changes may be caused not only by the elevated temperature but may be additionally induced by the electron beam. However, the multipod structures shown in Fig. 4.4 were found everywhere on the SiN support membrane, also in areas that were not previously exposed to the electron beam. Because of non-ideal orientations of the heterogeneous nanocrystals with respect to the

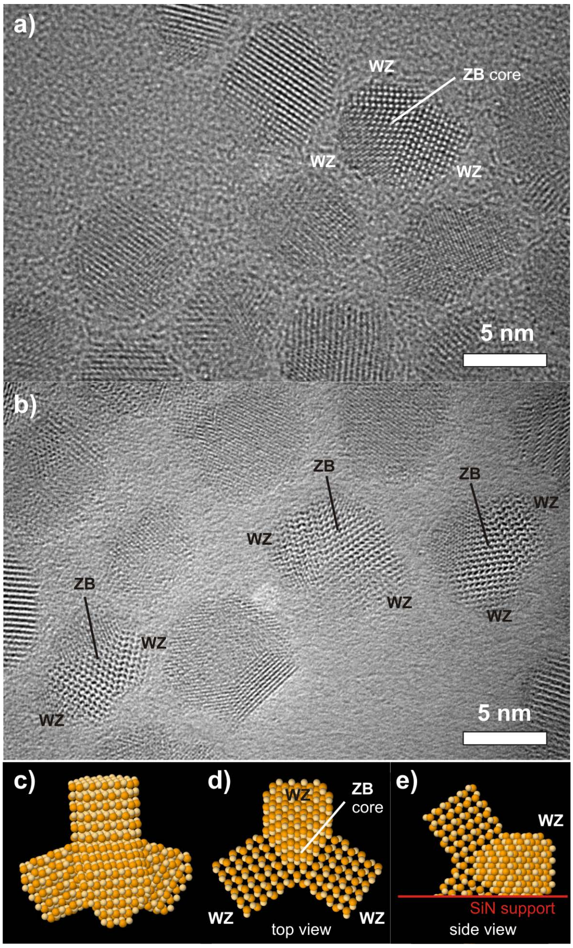
a)
WZ
ZB core
WZ
WZ
5 nm
b)
ZB
ZB
WZ
WZ
WZ
WZ
WZ
ZB
WZ
WZ
5 nm
c)
d)
WZ
ZB core
WZ
top view
WZ
e)
WZ
SiN support
side view

Figure 4.4: (a) HRTEM image of CdSe nanocrystals after low temperature annealing (350 K). The HR fringes reveal that the NCs consist of multiple domains, some of which are ZB and some of which are WZ. One particular NC has nearly spherical shape, but also contains all the elements of a tetrapod (the ZB core and the WZ pods are indicated). (b) After annealing to a temperature of 390 K, several NCs evolve into tetrapods, whereby the WZ legs become more pronounced. (c) Schematic of a tetrapod in a perspective view. (d) Schematic showing the projection of the tetrapods observed in the HRTEM images. (e) Schematic showing side view of (d): two pods are lying onto the support, the third pod is pointing away from the support, while the fourth (short) pod is pointing into the support; the latter two are overlapping in projection.

projection plane, the morphology of many NCs could not be distinguished. The synthesis and temperature treatment could be fine-tuned to yield a higher fraction of tetrapods after annealing, which is beyond the scope of the present work. A more extensive experimental study will be published elsewhere.

A direct comparison between the simulation results and experimental studies is difficult, as in the experimental situation the initial NCs are covered by stabilizing surfactants, which has a profound effect on the surface chemistry and therefore on the overall stability of the NCs. The extension of the WZ pods during annealing was not observed in the simulations, but this is most likely due to the limited simulation times (30 ns in simulation versus ~20 minutes in experiment). Other major differences between experiment and theory are the presence of a support in the experiments that is absent in the simulations and a different starting configuration (WZ/ZB distribution within the NCs). Nonetheless, the preliminary experiments show that the tiny tetrapods found in the simulations can actually be formed and do have a certain thermal stability. The merit of the simulations is that they provide fundamental insight into the ZB-WZ transition at the atomic scale: whereas a slip mechanism would be in the line of expectation, here we show that slip does not occur, and that instead the transformation is mediated by mobile vacancies on the cation sublattice.

4.3.4 Temperature and Size Effects

As already mentioned, the time scale in the experiments is many orders of magnitude larger than in the MD simulations. Therefore, in our simulations the temperatures were artificially elevated in order to shorten the transition times. For instance, CdSe NCs melt at a temperature above 750 K in the TEM, but in our MD simulations of 30 ns, we did not observe melting below 1000 K. A similar situation was also present in the study of the pressure induced WZ-to-RS transition in CdSe nanocrystals by Grünwald *et al.* [93]. It should be noted that the interaction potentials used in this work were developed by fitting the bulk properties of CdSe, so the different energetics and changes of the electronic structure of nanosized CdSe are not accounted for. Therefore, the temperatures in the simulations should be compared with the temperatures in the experiments in a qualitative manner. Figure 4.5 shows a graphical overview of configurations obtained at 6 different simulated temperatures, for 3 different NC sizes. The following striking features are observed: (1) Below 400 K, no apparent sphere-to-multipod transition is found within 30 ns. The spherical ZB CdSe NCs only show some rearrangement of surface atoms. (2) At temperatures of 400-1000 K, the sphere-to-multipod transitions are observed. Identical NCs evolve into configuration with longer legs within 30 ns when heated to higher temperatures. (3) In a temperature range of 1000-1200 K, melting of the NCs is observed.

Another interesting question is whether instead of a tetrapod, an octapod could be formed by heating. In the case of an octapod, the ZB core is octahedral with four equivalent $\{111\}$ facets as well as four equivalent $\{\bar{1}\bar{1}\bar{1}\}$ facets. However, it is generally known that a II-VI semiconductor nanooctapod is more difficult to be synthesize than a nanotetrapods, because the four ZB $\{\bar{1}\bar{1}\bar{1}\}$ facets are more reactive than the four ZB $\{111\}$ facets during colloidal synthesis of nanomaterials [20]. Only using a proper ZB core (a seed) with octahedral morphology, proper ligands, and well-controlled reaction temperatures, can these nanooctapods be synthesized successfully. Nonetheless, CdSe NCs with octapod morphology are observed in some cases in our simulations. As shown in Fig. 4.5, final configurations with a octapod morphology are observed for the $Cd_{860}Se_{860}$ at 800 K and $Cd_{1514}Se_{1514}$ NC at 800 K and 1000 K. In this work, the octapod-like morphology is only found in the largest NC model. This is in good agreement with experimental synthesis reports of nanotetrapods and nanooctapods. For octapods, it is required that the eight ZB$\{111\}$ facets of the core are well developed, which can be only achieved if the ZB core (seed) is sufficiently large. In addition, it is notable that the final configuration of the $Cd_{1514}Se_{1514}$ NC at 600 K, 800 K and 1000 K shows octapod-like morphologies, while the $Cd_{860}Se_{860}$ NC displays an octapod morphology at 600 K and 800 K, but at a higher temperature of 1000 K a tetrapod is formed. This unexpected result is in line with experimental results. In the synthesis of branched NCs, the reaction temperature is a critical factor to determine the morphologies

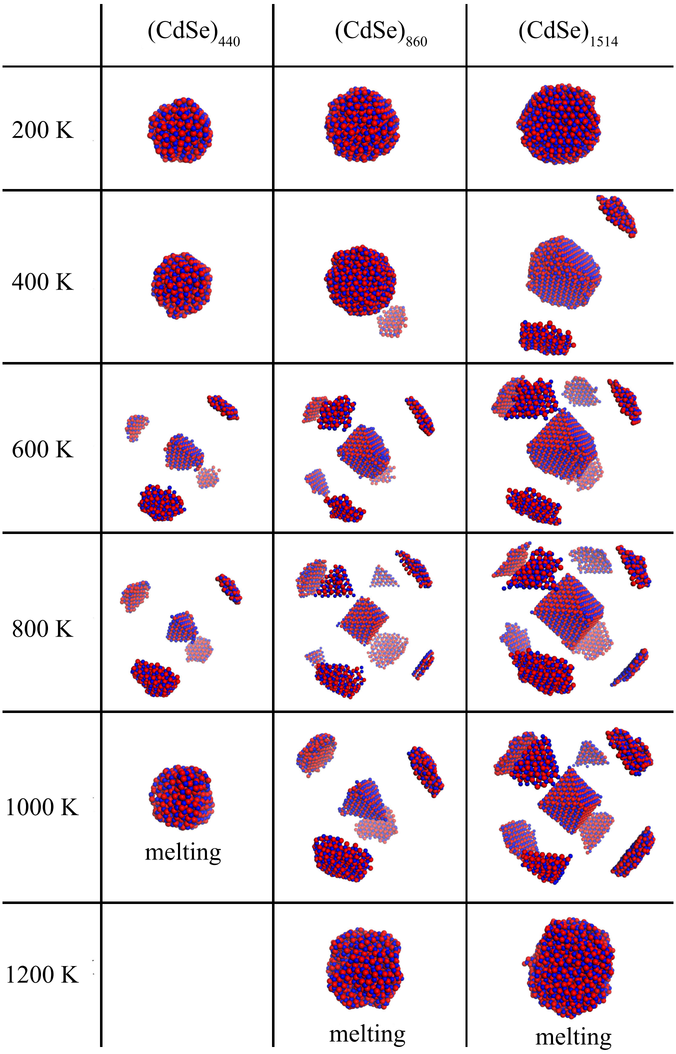
(CdSe)440
(CdSe)860
(CdSe)1514
200 K
400 K
600 K
800 K
1000 K
melting
1200 K
melting
melting

Figure 4.5: Final configurations of CdSe NCs with different sizes at various temperatures. When the ZB-to-WZ local structural transition takes place, for clarity reason the WZ domains are shifted along their [111] directions. The blue and red spheres are Cadmium and Selenium respectively.

of the products. Deka *et al.* [20] pointed out that in the synthesis of CdSe branched NCs, CdSe nanooctapods were observed in the temperature range between 593 K and 623 K, and the final products would be nanotetrapods instead if the reaction temperature was elevated to 653 K.

4.4 Conclusions

In summary, the morphological and structural transformations of the ZB CdSe NCs at high temperatures were studied using MD simulations with the Rabani CdSe potential. In the temperature range 600-1000 K, ZB CdSe nanospheres with different sizes change into heterogeneous NCs with tetrapod- or octapod-like morphologies. The morphology of the final configurations in the MD simulations depends on the size of the NCs and the temperature. The nanotetrapod consists of one tetrahedral ZB core and four WZ legs. The {111} surfaces on the ZB core connect with the {0001} surfaces of the WZ legs. In contrast to the tetrapod, octapods have ZB cores in an octahedral shape, whose four {111} and four $\{\bar{1}\bar{1}\bar{1}\}$ facets can adjoin with eight WZ legs. By means of MD simulations we have mimicked possible annealing experiments of the CdSe NCs in vacuum, and technically, the result can be clarified by characterizations such as HR-TEM or high-temperature X-ray diffraction, assuming ligands do not play any role (bare surfaces). A close inspection shows that the local ZB-to-WZ transition is caused by the shift of the Cd layer within the ZB {111} atomic plane, which is enabled by a high mobility of individual Cd vacancies. This finding is also of importance for understanding the process of cation exchange [27, 280], whereby cations within the nanostructure are (partly) replaced with other cations (*e.g.*, Pb ions in PbSe nanorods are partly exchanged with Cd ions so that core/shell PbSe/CdSe nanorods are obtained). It is commonly observed that the overall morphology of the nanostructures remains intact, presumably because the anion (Se) sublattice does not participate in the cation exchange process. This is in line with the current finding of high atomic mobility on the cation sublattice. The total potential energy of a tetrapod morphology was found to be *lower* than that of a spherical ZB

NC having the same number of atoms. The ZB or WZ CdSe NCs that are synthesized in experiments contain unstable surfaces with relatively high surface energies, but these unstable surfaces are passivated by ligands. We suggest that if these ligands could be entirely removed, for example by evaporation, a new morphology or structure with a lower potential energy will eventually be found. The simulation results are in good agreement with experimental results obtained by in-situ heating of 6-nm sized CdSe NCs inside the transmission electron microscope. The heterogeneous transition of the CdSe NCs could emerge as a new method of fabricating tetrapod or octapod morphologies and will be subject of future investigations.

Chapter 5

Cation Exchange in CdSe-PbSe Nanodumbbells

This chapter is based on the paper: A. O Yalcin, Z. Fan, B. Goris, W-F. Li, R. S. Koster, C. Fang, A. Van Blaaderen, M. Casavola, F. D. Tichelaar, S. Bals, G. Van Tendeloo, T. J. H. Vlugt, D. Vanmaekelbergh, H. W. Zandbergen, M. A. Van Huis, 'Atomic Resolution Monitoring of Cation Exchange in CdSe-PbSe Heteronanocrystals during Epitaxial Solid–Solid–Vapor Growth', Nano Lett., 2014, ***14****, pp 3361–3367.*

5.1 Introduction

Both the synthesis and design of hetero-nanocrystals (HNCs) have undergone a rapid development, whereby PbSe and CdSe NCs are key materials acting as functional building blocks within a wide variety of heterogeneous nanostructures [9, 18, 27, 39, 281–284]. PbSe-CdSe HNCs are of particular interest as they can exhibit properties different from individual PbSe and CdSe dots. The presence of two semiconductor quantum dots connected via a well-defined interface opens new possibilities for tailoring the optoelectronic properties [9, 18, 27, 282, 283, 285]. Heat treatment of HNCs can induce new interface designs [282, 286–289] exemplified by the transformation of PbSe/CdSe core/shell systems into PbSe-CdSe bi-hemispheres [282]. In this Chapter, we report an in-situ heating-induced epitaxial PbSe NC domain growth at the solid-solid PbSe-CdSe nano-interface through cation exchange. We show that Pb replaces Cd at the PbSe/CdSe interface, resulting in growth of the PbSe phase at the expense of the CdSe phase. The incorporated Pb is originating from Pb-oleate present as excess stabilizer at the surface of the mature PbSe/CdSe HNCs.

Vapor-liquid-solid (VLS) [290–292] and vapor-solid-solid (VSS) [293, 294] growth mechanisms are nowadays commonly applied in nano-chemistry to epitaxially grow semiconductor nanowires from the elements dissolved in a liquid (VLS) or solid (VSS) domain. In analogy with these growth mechanisms, the currently observed process could be called solid-solid-vapor (SSV) growth as the Cd evaporates, either as neutrally charged Cd atoms or in a molecular complex such as Cd-oleate.

5.2 Methods

5.2.1 In Situ Transmission Electron Microscopy

The synthesis of PbSe/CdSe dumbbell nanostructures is detailed in the Supporting Information of Ref. [35]. TEM specimens were prepared by dropcasting 8 l of the NC colloidal solution onto a MEMS microhotplate with electron-transparent SiN membranes, which was mounted onto a DENSsolutions low drift TEM heating holder [44]. After dropcasting, the sample was plasma cleaned for 10 s in order to remove deposits from the solution which prevent high-resolution imaging in the TEM. The in-situ experiments were performed in a 80-300 FEI Titan microscope equipped with a Chemi-STEM EDX detection system. During HAADF-STEM imaging, the microscope was operated at 300 kV. The camera length used in the experiments equals 91 mm in order to avoid diffraction effects and to guarantee Z-contrast imaging. In HAADF-STEM imaging, the intensity approximately scales with Z^2. As Pb has a higher Z-number than Cd, the PbSe domains appear with higher intensity in HAADF-STEM images in comparison to the CdSe domains.

5.2.2 Scanning Transmission Electron Microscopy Energy-Dispersive X-ray Spectroscopy Experiments

Chemi-STEM EDS experiments were performed using the same holder and in the same 80-300 FEI Titan microscope, but operated at an acceleration voltage of 200 kV. A beam current of approximately 250 pA was used for the acquisition of the EDS maps. A representative spectrum is shown in Supplementary Figure S20 of Ref. [35]. In the quantification of the elemental maps, 18 PbSe NC maps were used to determine the cation/anion ratio at the PbSe tips at the initial state. For the PbSe tips from where cation exchange proceeded, the elemental composition of 10 different PbSe tips was quantified. For the nanorod domains attached to the PbSe tips where cation exchange took place, the elemental composition of 10 different nanorod (transformed)-domains were quantified.

5.2.3 Molecular Dynamics Simulations

For the MD simulations, we used the new force field for the PbSe-CdSe system in Chapter 3. A description of the nano-dumbbell models are given in Section E of the Supporting Information of Ref. [35]. For simulations of the nano-dumbbells, Coulomb and short-range interactions were calculated by taking into account all atom pairs. The equations of motion were integrated using the velocity Verlet algorithm with a time step of 1 fs. Periodic boundary conditions were not used and the nano-dumbbell models were isolated in vacuum. Simulations of 5 ns were carried out in the NVT ensemble and 1 ns was used for equilibration.

5.2.4 Density Functional Theory Calculations

All density functional theory (DFT) calculations on defect energies and energies of mixed PbSe-CdSe phases were carried out using the first-principles

Vienna Ab initio Simulation Program (VASP) [59] using the Projector-Augmented Wave (PAW) method [295]. The generalized gradient approximation (GGA) formulated by Perdew, Burke, and Ernzerhof (PBE) was employed for the exchange and correlation energy terms [166]. The cut-off energy of the wave functions was 350.0 eV. The cut-off energy of the augmentation functions was about 500.0 eV. The electronic wave functions were sampled on a 442 grid using the Monkhorst and Pack method with 8 to 20 k-points depending on different symmetries of supercells (108 atoms). Structural optimizations were performed for both lattice parameters and coordinates of atoms. Different k-meshes and cut-off energies for waves were tested to have a good convergence (<2 meV/atom).

5.3 Results

5.3.1 In Situ TEM and STEM EDS Experiments

Figure 5.1a shows a HAADF-STEM image (high angle annular dark field scanning transmission electron microscopy) of CdSe-PbSe dumbbell HNCs, consisting of CdSe nanorods with PbSe tips at both ends. In this imaging mode, the intensity scales with Z^2, where Z is the atomic number. As Pb has a higher Z than Cd, PbSe NCs exhibit brighter contrast than the CdSe nanorods. When the HNCs were heated to 433 K with a heating rate of 10 K/min and annealed at this temperature for 5 min, the bright contrast corresponding to PbSe was observed not only at the tips, but extended gradually inside the nanorod domain (solid arrows in Fig. 5.1b), showing that the PbSe phase grows at the expense of the CdSe phase. When the HNCs were heated to 473 K with the same heating rate and annealed at this temperature for 5 min, the bright contrast was observed over the entire nanorod in some nanorods (solid arrows in Fig. 5.1c). The evolution of this growth was seen to initiate mostly from one PbSe tip domain (Supporting Movies S1 and S2 of Ref. [35]), though it can also proceed from both PbSe tip domains (dashed arrows in Fig. 5.1b-c).

Chemical mapping by means of Energy-Dispersive X-ray Spectrometry (EDS) using a Chemi-STEM detector (see Methods section) was performed

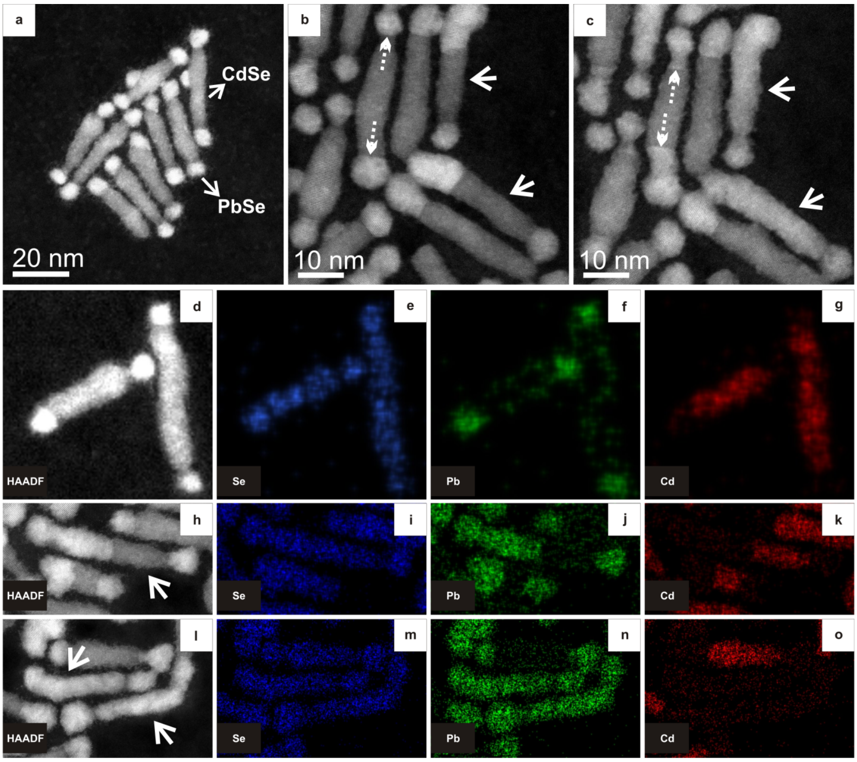

Figure 5.1: HAADF-STEM images and chemical mapping of the nano-dumbbells before and after heating. (a) HAADF-STEM image of CdSe-PbSe nano-dumbbells. The PbSe tips exhibit brighter contrast than the CdSe nanorods due to Z-contrast. (b,c) Dumbbell HNCs at 433 K (b) and at 473 K (c), showing gradual extension of PbSe domains at the expense of CdSe. A heating rate of 10 K/min was used in the in-situ studies and the HNCs were annealed at the indicated temperatures for 5 min before imaging. Dumbbell HNCs with solid arrows transformed totally to brighter contrast with heating. This phenomenon occurred mostly from one side, though it can proceed from both PbSe domains as well (dumbbell with dashed arrows in (c)). (d-o) HAADF-STEM images and corresponding STEM-EDX elemental maps of dumbbell hetero-nanostructures annealed for 5 min at temperatures of (d-g) 373 K, (h-k) 443 K, and (l-o) 473 K. In (d-g), HNCs are in original dumbbell state with PbSe tips and CdSe nanorod. In (h-k), a partially transformed nanorod is present. In (l-o), two PbSe-CdSe HNCs became full PbSe domains. The Se remains in place during the transformation. Note that the contrast is maximized in each individual image; hence intensities of different mappings cannot be directly compared.

to provide further evidence of the chemical transition. Figs. 5.1d,g show the initial state of the HNCs at 373 K with CdSe nanorods and PbSe tips. Fig. 5.1f shows that Pb is also present at the lateral surfaces of the CdSe nanorods, pointing to adsorbed Pb-oleate molecules. The dumbbell depicted with an arrow in Fig. 5.1h underwent a transformation after which half the nanorod exhibited a bright contrast. With annealing at 443 K for 5 min, the elemental maps of this dumbbell in Figs. 5.1i-k show that Pb is indeed present in the bright contrast regions and that Cd is absent. We therefore conclude that Cd started to sublimate (as neutral Cd atoms, or in a molecular form) and that at the same time PbSe was formed by Pb incorporation. Upon further heating to 473 K and 5 min annealing at this temperature, two nanorods (indicated with arrows in Fig. 5.1l) exhibited a bright contrast over their entire length. Elemental maps (Figs. 5.1m-o) showed that Cd is no longer present and the nanorod completely transformed into PbSe. Disappearance of Cd from a nanostructure was also reported by De Trizio *et al.* [288] during a heating of sandwich-morphology CdSe/Cu_3P/CdSe HNCs. Note that a complete transformation occurred very rarely (in about one per cent of the cases). Further heating of partially cation-exchanged nano-dumbbells led to dissociation of the domains (Supporting Movie S3 of Ref. [35]). The transformations took place everywhere on the substrate, not only in areas that were previously examined with the electron beam. The field of view was changed frequently in order to avoid beam effects when monitoring the evolution of the HNCs.

As a result of the cation exchange from CdSe to PbSe, the crystal structure transformed epitaxially from hexagonal wurtzite (WZ) to cubic rocksalt (RS). Fig. 5.2 and Supporting Movie S4 Ref. [35] show this transformation at atomic resolution. When the HNC was heated from 433 K (Fig. 5.2a) to 453 K (Fig. 5.2b) with a heating rate of 10 K/min, the brighter intensity corresponding to PbSe advanced into the CdSe region. The PbSe RS (200) lattice spacings started to appear along the nanorod domain instead of the CdSe WZ (0002) lattice spacings, as confirmed by the Fourier Transformation (FT) patterns shown in the insets. It is clear that the cation exchange takes place at the PbSe/CdSe interface and propagates epitaxially (layer by layer) along the WZ<0001>direction. Two types of interfaces were observed: {100}PbSe/{0001}CdSe and {111}PbSe/{0001}CdSe, similar to the interfaces previously reported in the literature for PbSe/CdSe and PbS/CdS HNCs [18, 215]. Sometimes both types of interfaces were observed within one single dumbbell NC. Figure. 5.2c shows a HNC with the interfaces of {111}PbSe/{0001}CdSe on the left (Fig. 5.2d) and {100}PbSe/{0001}CdSe on the right (Fig. 5.2f). It is clear from (Fig. 5.2 that epitaxial PbSe growth inside CdSe domain via cation exchange can advance from both PbSe/CdSe interfaces.

Considering the source of Pb that is required for the epitaxial PbSe growth in CdSe via cation exchange, we note that PbSe NCs with excess Pb surface atoms (off-stoichiometric) have been reported in the literature [297–299]. Pb atoms (possibly Pb-oleate molecules) are also present along the CdSe nanorods (Fig. 5.1f). From the quantification of the elemental maps (Table S1 of Ref. [35]), it was found that the PbSe tips contained an excess of Pb, having a cation/anion ratio of 1.3±0.2. After the transformation, the cation/anion ratio at these PbSe tips reduced to 1.02±0.14. These findings indicate Pb diffusion from PbSe tips towards the PbSe/CdSe interface. Supporting Movie S4 in Ref. [35] verifies this, whereby the bright Pb contrast propagates into the initially CdSe nanorod indicating the epitaxial growth of PbSe while the (PbSe) tip domain starts to lose some of its brightness indicating that excess Pb is consumed.

In the nanorod domains attached to the PbSe tips where cation exchange took place, the cation/anion ratio in the rod was reduced to 0.93±0.11 due to Cd sublimation. That most nano-dumbbells were not completely transformed must hence be due to the depletion of the source of Pb. The excess Pb atoms at the surfaces of the hetero-nano-interface diffuse towards the interface to form new layers of PbSe, but this process stops when all excess Pb has been depleted. As mentioned above, a complete transformation of the nanorods occurred only rarely. From an estimate of the number of Pb-oleate molecules that could cover the surface of the nanodumbbells (assuming a high surface density of 5 Pb-oleate molecules per nm^2), it was found that for the typical dimensions of the nanodumbbells in this study, the number of surface Pb atoms is not sufficient to replace all the Cd atoms in the CdSe domain (the number of Cd sites is at least two times larger).

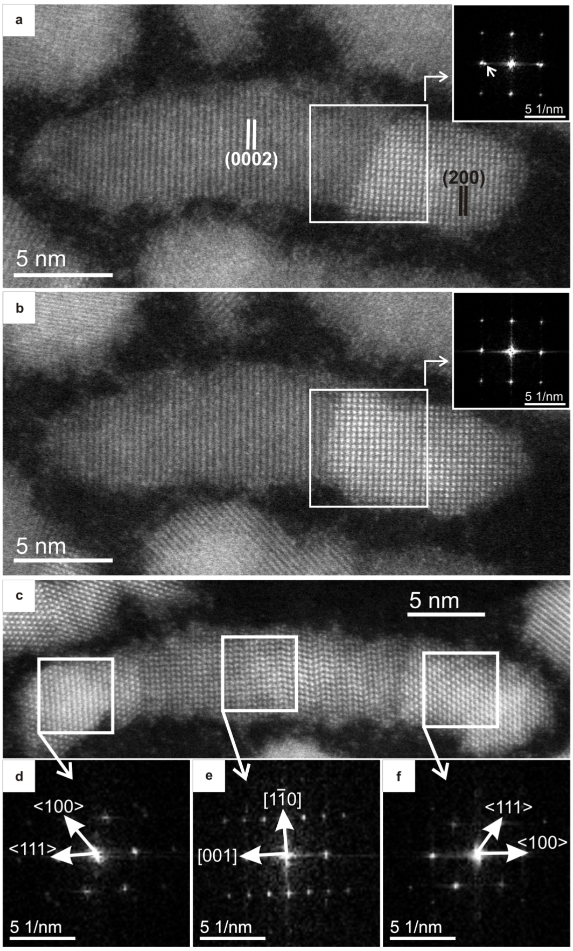

Figure 5.2: Atomic-resolution HAADF-STEM images of CdSe-PbSe HNCs. PbSe has cubic rock salt (RS) crystal structure with a lattice constant [296] of 6.13 Å, while CdSe has a hexagonal wurtzite (WZ) crystal structure with lattice parameters21 a=4.29 Åand c=7.01 Å. The CdSe WZ (0002) spacing is 3.5 Åand PbSe RS (200) spacing is 3.1 Å. With heating from 433 (a) to 453 (b) K with a heating rate of 10 K/min, WZ CdSe nanorods started to transform to RS PbSe. The insets are Fourier Transforms (FTs) taken from the white squares in each image. The spot depicted with an arrow in the inset FT of (a) corresponds to WZ CdSe(0002) spacing. It disappeared in the inset FT of (b), confirming the WZ to RS transformation. (c) HAADF-STEM image of a PbSe-CdSe dumbbell HNC. Stacking faults and a dislocation are present in the CdSe nanorod domain. The interface at the left-hand side is {111}PbSe/{0001}CdSe (panel 2d) whereas the interface at the right-hand side is {100}PbSe/{0001}CdSe (panel f).

Therefore, when a complete transformation does occur, likely also Pb atoms from neighbouring HNCs will have contributed to the growth of the PbSe domain. This is in agreement with the observation that when the nanodumbbells were lying isolated on the SiN support membrane, the growth process did take place but always resulted in only a partial transformation of the HNCs as shown in Fig. S21 of Ref. [35].

5.3.2 MD Simulations and DFT Calculations

In order to better understand the nanoscopic growth mechanism at the PbSe/CdSe interface, force field based MD simulations were performed on HNC models taking into account various possibilities for the PbSe/CdSe interfacial arrangements. Surfactant molecules are not included in the simulation models, and therefore the MD simulations serve only to study the structure of and atomic mobility at the PbSe/CdSe interfaces. The isolated nano-dumbbell models were equilibrated at 300 K and 500 K for 5 ns sequentially. Figure. 5.3a shows the final configuration of a nano-dumbbell model after 5 ns at 500 K. This model has both types of the interfaces (100PbSe/0001CdSe and 111PbSe/0001CdSe) in one HNC.

The nano-dumbbell model shown in Fig. 5.3 is structurally and morphologically stable at temperatures up to 500 K. The middle part of the CdSe rod and the whole PbSe tips retain their initial WZ and RS structures respectively. Structural disorder was mainly found in the CdSe domains near the interfaces. Compared to the {100}PbSe/{0001}CdSe interface, the CdSe domain near the {111}PbSe/{0001}CdSe interface is more structurally ordered. In the latter case, most of the Cd and Se atoms remain at the WZ lattice sites, which is likely due to the fact that the cation-terminated {0001}CdSe surface and the anion-terminated {111}PbSe surface form a continuous polar/polar interface whereas the lattice mismatch is small. In contrast, the {100}PbSe/{0001}CdSe interface is a non-polar/polar interface which leads to stronger distortions in the atomic lattice due to Coulombic interactions. The simulations therefore suggest that the transformation at the {100}PbSe/{0001}CdSe interface will be more efficient than at the {111}PbSe/{0001}CdSe interface, although this could not be confirmed by

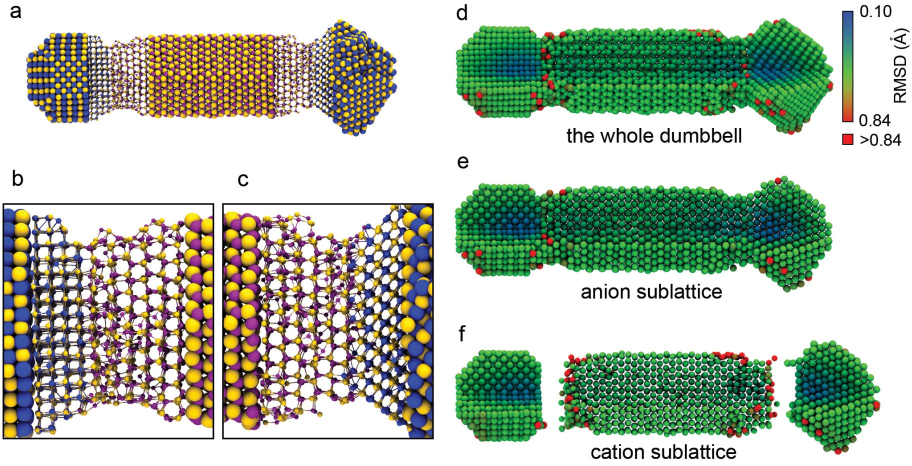

Figure 5.3: MD simulations of the PbSe-CdSe nano-dumbbells. (a) Overview image showing the final configuration of a dumbbell obtained after MD simulation at a temperature of 500 K for 5 ns. The ball-stick presentation was used to show the structure of the interfaces. The yellow, purple, and blue spheres are Se, Cd, and Pb atoms, respectively. (b) Magnified image of the {100}PbSe/{0001}CdSe interface at the left-hand side of the dumbbell, and (c) magnified image of the {0001}CdSe/{111}PbSe interface at the right-hand side of the dumbbell. (d,e,f) The map of the root-mean-squared displacement (RMSD) for each atom for the same PbSe-CdSe dumbbell model at 500 K. (d) The whole PbSe-CdSe dumbbell, (e) the anion sublattice, (f) the cation sublattice. The dumbbell was cut so that both of the surface and inner atoms can be seen. The red atoms have a RMSD larger than 0.84 Å.

the experiments as the orientation of the two crystals could be determined only in a limited number of cases. Not only is the atomic structure more disordered in the CdSe domains near the {100}PbSe/{0001}CdSe interfaces, the simulations also show an unusually high mobility of the Cd atoms in the few first atomic layers from the PbSe/CdSe interface, as evidenced by the map of the root-mean-squared displacement (RMSD) for each atom (Figs. 5.3d-f). Those atoms with the highest mobility (red atoms) are mostly Cd atoms near the interfaces or on the surface, indicating that the cation exchange occurs only very close to the interface.

The experimental observations and the MD simulations suggest that the transformation is mediated by vacancies in the Cd and Pb sublattices; evaporation of Cd results in Cd vacancies at the CdSe surface. After migration of these Cd vacancies to the PbSe/CdSe interface, Pb atoms can jump into the vacant sites, thereby leaving behind vacancies on the Pb sublattice, which will eventually recombine with excess Pb absorbed at the surface of the PbSe domain.

Density Functional Theory (DFT) calculations of defect energies (see Section F in Supporting Information of Ref. [35]) confirm that upon evaporation of Cd, both in CdSe and PbSe the defect energetics are ruled by vacancies. The DFT calculations also show (Table S10 in Ref. [35]) that the Se-Frenkel defect energy (Se vacancy + Se interstitial) is considerably higher (6.00 for CdSe and 3.80 eV for PbSe) than the Cd-Frenkel and Pb-Frenkel defect energies (3.16 and 3.30 eV, respectively). It is thus energetically much more expensive to create defects on the Se sublattice. Because the Se sublattice is not much affected by the cation exchange which takes place on the (Pb,Cd) sublattice, the crystallographic orientation relation between the CdSe and PbSe nanodomains is retained during the transformation. This is the reason that the growth process is epitaxial in nature.

5.4 Discussion

The most important driving force for the growth process is the evaporation of Cd. It is well known that a chemical reaction can be efficiently driven into one direction by bringing one reaction product in the gas phase. Assuming that the excess Pb originates from Pb-oleate coverage of the HNC and that the Cd evaporates in a molecular form, the reaction can be summarized as follows:

$$\mathrm{CdSe(s) + Pb - molecule(s) \rightarrow PbSe(s) + Cd - molecule(g)} \tag{5.1}$$

In the CdSe lattice, the Cd and Se atoms can be modelled as ions. Bader charge analysis performed on the electronic charge density obtained from DFT calculations shows that the effective charge of the Cd cation in CdSe bulk is approximately +0.8 e. However, the Cd will evaporate only as a neutral species. Because the transition from a charged $\mathrm{Cd}^{+0.8}$ ion to a neutral Cd^0 atom would require the nanocrystal to donate electrons, we consider it more likely that Cd at the surface of the nanocrystal binds to the surfactants (*e.g.*, oleate), followed by evaporation. We mention here that heating in vacuum is an efficient method to detach surfactants from nanocrystals [44, 296].

From the available experimental and simulation data, a mechanism can now be deduced to describe the cation exchange. All processes take place close to the interfaces in a fast and volatile manner as demonstrated by Supporting Movie S4 of Ref. [35]. The growth mechanism is shown schematically in Figure S1 of the Supporting Information of Ref. [35], and can be summarized as follows. (1) Cd sublimates from the surface of the CdSe nanodomains, whereby Cd vacancies are formed. (2) The Cd vacancies occupy positions at the CdSe side of the PbSe/CdSe interface (Figure S22 of Ref. [35]). (3) Cation replacement takes place as Pb atoms jump into vacant Cd sites in a layer by layer fashion, resulting in epitaxial growth of RS PbSe at the expense of WZ CdSe. (4) The jumping Pb atoms leave behind vacancies, which migrate to the PbSe surface. (5) The Pb vacancies at the surface recombine with Pb ions from adsorbed Pb-oleate molecules. The oleate molecule remains adsorbed at the PbSe surface, and possibly migrates to the CdSe domain where it combines with Cd and evaporates as Cd-oleate. (6) The process is halted when the excess Pb (in the form of Pb-oleate molecules) in the system is depleted.

5.5 Conclusions

In this Chapter, we show a novel solid-solid-vapor (SSV) growth mechanism whereby epitaxial growth of heterogeneous semiconductor nanowires takes place by evaporation-induced cation exchange. During heating of PbSe-CdSe nanodumbbells inside a transmission electron microscope (TEM), we observed that PbSe nanocrystals grew epitaxially at the expense of CdSe nanodomains, driven by evaporation of Cd. MD simulations reveals that the growth process is mediated by local structural disorder and formation of Cd vacancies. The atomistic mechanism described here most likely also takes place when HNCs undergo cation exchange in colloidal solutions, whereby instead of evaporating, the metal-molecule complex is dissolved in the solution. In the current solid-solid-vapor (SSV) growth mechanism, one solid phase grows epitaxially at the expense of another solid phase, efficiently driven by evaporation of one element (here Cd) with simultaneous supply of another element (here Pb, coordinated with a molecule). Our results show that SSV growth can provide an alternative path for growing heterogeneous semiconductor nanowires, especially when the lattices have a partly ionic character, and therefore holds promise for generating new families of heterogeneous nanostructures.

Chapter 6

Cation Exchange in PbS-CdS Nanocrystals

This chapter is based on the paper: Z. Fan, L-C Lin, W. Buijs, T. J. H. Vlugt, M. A. Van Huis, 'Atomic Understanding of Cation Exchange in PbS Nanocrystals Using Pseudolidands' submitted.

6.1 Introduction

To synthesize novel nanocrystals (NCs) and heteronanocrystals (HNCs) with designed shape and structure, cation exchange (CE) has recently been extensively explored and applied to nanoscale materials [9, 38–41, 280, 300, 301]. This process involves colloidal ionic NCs whereby the cations in the NCs are (partially) replaced by the cations from the surrounding solution. CE has greatly boosted the syntheses of nanostructures with diverse morphologies. Starting from elementary NCs that are synthesized using well-known synthesis routes such as hot injection [13], the CE technique can be used to modify the nanostructures into other novel nanostructures or heterostructures such as binary rods [26] and core/shell structures [36, 38]. The CE technique can be extremely powerful when combined with other advanced (post)syntheses techniques such as oriented attachment and seeded growth. This has enabled the synthesis of many novel nanostructures including nanooctapods [40], nanorod couples [25], and 2D honeycomb superlatices [23].

Pb→Cd exchange (*i.e.* replacing Pb^{2+} by Cd^{2+}) in lead chalcogenide NCs is a typical CE process that produces PbE/CdE (E = S, Se, Te) core/shell HNCs [27, 28, 36]. This CE process in colloidal PbS NCs can be expressed as follows:

$$\mathrm{Cd}^{2+}_{\mathrm{liquid}} + \mathrm{PbS}_{\mathrm{solid}} \rightarrow \mathrm{Pb}^{2+}_{\mathrm{liquid}} + \mathrm{CdS}_{\mathrm{solid}} \tag{6.1}$$

A typical experimental route of this CE consists of two simple steps [36, 37]: (1) synthesis of the PbS parent NCs, and (2) immersing the parent NCs in Cd-oleate solutions and applying heat for 0.5-10 hours at 373–473 K. PbS has a rocksalt (RS) crystal structure where the atoms have six-fold coordination, while CdS has a zinc blende (ZB) crystal structure where the atoms have four-fold coordination. The lattice mismatch between these two structures is less than 2% [95]. Pb→Cd CE in PbE NCs has often been described as a self-limiting process as the core/shell structure is often found in the product. Complete conversion is usually difficult to achieve [27, 37, 302]. Compared to other types of CE [9, 42] (*e.g.*, Cd→Ag) that take place spontaneously at ambient temperature and at a shorter timescale, the Pb→Cd CE requires a relatively high temperature and a long time to overcome a large energy barrier [34].

Although the Pb→Cd CE process has been studied by modern experimental techniques such as energy dispersive X-ray spectrometry (EDX), high resolution transmission electron microscopy (HRTEM), and 3D electron tomography [28, 35, 37, 281, 302], a detailed atomistic understanding of the atomistic mechanism is still missing. Theoretical investigation of this CE process using molecular simulation remains a great challenge. As schematically shown in Fig. 6.1a, CE not only involves parent NCs, but also the surrounding solution, consisting of exchanging cations, ligands, and solvent molecules. CE takes place first at the interface between the NCs and solution and then proceeds further into the NCs. To model the whole system atomistically requires large system sizes and long simulation

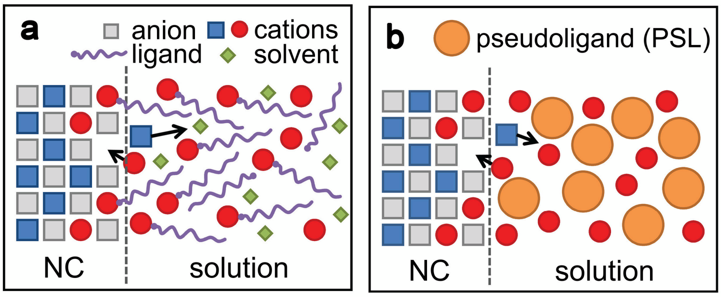

Figure 6.1: Schematic representation of a cation exchange (CE) process. (a) CE in experiments; (b) CE in MD simulations with a coarse-grained pseudoligand (PSL) model. The dash lines indicates the NC/solution boundaries; The black arrows indicate the motion of the cations during a CE process. The solution of cations and PSLs is essentially an ionic liquid

times, which is not computationally feasible. To overcome this, we developed a coarse-grained model to mimic the cation-ligand solutions in which the effects of ligands and solvent are incorporated into negatively charged large spherical particles (Fig. 6.1b, the orange circles). These particles are denoted by pseudoligands (PSLs). PbS-CdS systems are modelled using our newly developed all-atom force field [95] which accurately describes the crystal structures, elastic properties, polymorphic stability, and surface energy of PbS and CdS solids and $Pb_xCd_{1-x}S$ mixed phases. Here, classical Molecular Dynamics (MD) simulations are used, for the first time, to successfully study the Pb→Cd CE in PbS NCs within a solution. Our results indicate that the direction and rate of CE can be controlled by changing the ligand type, or by adjusting the temperature. A previously proposed vacancy-mediated exchange mechanism [27, 35, 302] has been revised according to our simulations and calculations. The Cd vacancies mediating the Pb jumps automatically form at the PbS/CdS interfaces, rather than formation on the NC surfaces and migrate to the interfaces. Co-operative behaviour was found in the Pb→Cd CE process that a Cd impurity decreased the energy barrier to a nearby Pb ion leaving the PbS core. Understanding the thermodynamics and kinetics of CE is crucial for the future development of the precise control of this technique.

6.2 Methods

6.2.1 Coarse-Grained Pseudoligand Model

The main function of our PSL model is to create a solution in which the exchanging cations can be dissociated and CE takes place at the NC/solution interface. We assume that electron transfer does not play an important role during the Pb→Cd CE, *i.e.*, the charges of the cations, anions, and anionic ligands in the solid and liquid phases, and at the solid/liquid interface remain unchanged. In the PSL model, the PSL-PSL or PSL-cation interatomic interactions consist two parts: long-ranged Coulombic interactions and short-ranged interactions described by a Buckingham potential [95]:

$$u_{ij}(r_{ij}) = \frac{q_i q_j}{r_{ij}} + Ae^{-r_{ij}/B} - \frac{C}{r_{ij}^6} \tag{6.2}$$

The partial charge of the PSL was set to -0.8 e. The parameters of the Buckingham potential are listed in Table 6.1. The parameters were tuned so that the systems consisting of cations and PSLs form liquid phases at temperatures around 400 K (typical temperature in CE experiments). In our model, the PSL-cation interactions are weaker than the Cd-S or Pb-S interactions. To control the strength of the PSL-cation interactions, we varied the parameter C for PSL-cation interactions. The parameter C of the PSL-cation interatomic potentials can be chose as 0 or 200 eV·Å^6. When keeping other parameters unchanged, a PSL-cation interaction potential with C = 200 eV·Å^6 has a lower minimum energy compared to that with C = 0 eV·Å^6 (see Fig. 6.2). The non-preferential, Pb-preferred, and Cd-preferred PSL models can be constructed using different combinations of the PSL-cation potentials with different values of parameter C (see Table 6.1).

Table 6.1: Parameters of the Buckingham potentials in the coarse-grained PSL model. The non-preferential, Pb-preferred, and Cd-preferred PSL models are constructed using different combinations of the cation-PSL potentials with different values of the parameter C.

	A (eV)	B (Å)	C (eV·Å^6)
non-preferential PSL			
Cd-PSL	1000	0.4	0
Pb-PSL	1000	0.4	0
S-PSL	15000	0.4	0
PSL-PSL	0	0.4	0
Pb-preferred PSL			
Cd-PSL	1000	0.4	0
Pb-PSL	1000	0.4	200
S-PSL	15000	0.4	0
PSL-PSL	0	0.4	0
Cd-preferred PSL			
Cd-PSL	1000	0.4	200
Pb-PSL	1000	0.4	0
S-PSL	15000	0.4	0
PSL-PSL	0	0.4	0

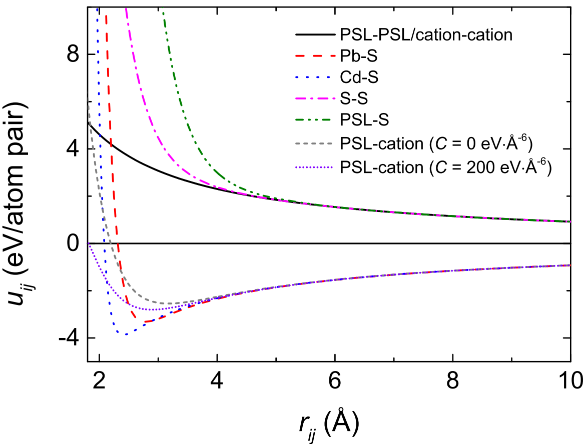

Figure 6.2: The interatomic interaction pair potentials as a function of interatomic distance $\mathbf{r_{ij}}$. The parameter C in the PSL-cation interatomic potentials can be chose as 0 or 200 eV·Å^6.

6.2.2 Construction of Colloidal PbS and CdS NCs

A spherical PbS NC with a diameter of 4.7 nm containing 1088 {Pb–S} pairs was cut out from a RS-PbS matrix with a lattice parameter of 6.0 Å. The PbS NC was placed in the centre of a cubic simulation box with a box dimension of 10 nm. The simulation box was randomly filled with 4352 {Cd–PSL} pairs such that the distance between any two ions is larger than 3.5 Å to prevent atomic overlaps. Periodic boundary conditions were applied in all directions. The construction of the colloidal ZB-CdS NCs is similar to that of RS-PbS NC systems described above. A spherical CdS NC with a diameter of 4.7 nm containing 1057 {Cd–S} pairs was cut out from a ZB-CdS matrix with a lattice parameter of 6.00 Å. 4228 {Pb–PSL} pairs were randomly positioned inside a cubic simulation box of a size of 10 nm.

6.2.3 Molecular Dynamics Simulation

All MD simulations were carried out using the LAMMPS code [303]. The Particle–Particle–Particle–Mesh (PPPM) method [304] was used to calculate the Coulombic interactions and a cut-off radius of 10 Å was set for all short-ranged interactions without using long-range corrections. The equations of motion were integrated using the velocity-Verlet algorithm with a time step of 1 fs. Four S ions in the centre of the NC were constrained at fixed positions to prevent the Brownian motion of the NCs. Simulations of 100 ns were carried out in a NPT ensemble and the first 100 ps was used for preliminary equilibration at the desired temperatures and zero pressure. Some simulations ran longer. The longest simulation time was 300 ns. For the simulations of the reverse Cd→Pb CE in colloidal ZB-CdS NCs, MD simulations were performed for the colloidal ZB-CdS NC for 100 ns at 550 K with non-preferential, Pb-preferred, and Cd-preferred PSLs.

6.2.4 Volume Scaled Exchange Rate

Several MLs were defined in a PbS NC (one ML has a thickness of 3.5 Å, see the inset of Fig. 6.6a) and the exchange rate in the j^{th} ML and at time t, $\eta_j(t)$, was defined as:

$$\eta_j(t) = \frac{(N^{\text{o}}_{\text{Cd}} - N^{\text{i}}_{\text{Cd}}) - (N^{\text{o}}_{\text{Pb}} - N^{\text{i}}_{\text{Pb}})}{\Delta t \Delta V_j} \tag{6.3}$$

where N is the number of Cd or Pb ions passing through the surface o or i during a time Δt. The superscripts o and i represent the outer and the inner surfaces of the j^{th} ML, respectively. A positive value of N indicates the cations are moving inward to a given ML while a negative value indicates moving outward. Δt is a small time interval ($\Delta t = 1$ ps) and ΔV_j is the volume of the j^{th} ML. Using this definition, a positive η indicates a Pb→Cd CE process while a negative value indicates the reverse Cd→Pb CE. We sampled the η_j every 100 ps for the first four outermost MLs from simulations for a PbS NC with non-preferential PSLs at 550 K. Each data point in Fig 6.6a corresponds to an averaged η_j over a time interval of 10 ns from ten independent simulations.

6.2.5 Root Mean Square Motion

Root mean square Motion (RMSM) was used to describe the vibration and mobility of the ions, defined as:

$$\text{RMSM} = \sqrt{\frac{1}{t}\sum_{t_j=1}^{t}(x_i(t_j) - \bar{x}_i)^2} \tag{6.4}$$

where t is the time to sample the data, which is the last 100 ps of ten independent 100 ns simulations. $x_i(t_j)$ is the position of an ion i at time t_j, $\bar{x}_i$ is the time-averaged position of the ion i. The time interval between two samplings is 1 ps. The RMSM of each ion and its initial distance r to the centre of the NC were calculated. The RMSM was further averaged over the same types of ions with similar r (± 0.5 Å).

6.2.6 PbS/CdS Interfacial Energy Calculations

To calculate the interfacial energy, two different PbS/CdS heterostructures were constructed including four different PbS/CdS interfaces (see Fig. 6.3). Figure 6.3a shows a PbS/CdS heterostructure that the PbS-[111] direction is oriented along the CdS-[111] direction, thus creating two polar/polar interfaces (the PbS-(111)/CdS-($\bar{1}\bar{1}\bar{1}$) and PbS-($\bar{1}\bar{1}\bar{1}$)/CdS-(111) interfaces, these two interfaces are donated as PbS-(111)/CdS-(111)). Figure 6.3b shows a heterostructure that the PbS-[100] direction is oriented along the CdS-[111] direction, thus creating two non-polar/polar interfaces (the PbS-(100)/CdS-(111) and PbS-(100)/CdS-($\bar{1}\bar{1}\bar{1}$) interfaces, these two interfaces are donated as PbS-(100)/CdS-(111)). These two types of interface are dominant in the PbS/CdS HNCs in our simulations and the PbE/CdE HNCs in CE experiments. Three-dimensional periodic boundary conditions were used. The initial interfacial areas of the PbS-(111)/CdS-(111) and PbS-(100)/CdS-(111) interfaces are about 240 and 280 Å^2, respectively. The initial lengths of the side perpendicular to the interfaces are about 41 and 47 Å for the PbS-(1110/CdS-(111) and PbS-(100)/CdS-(111) heterostructures, respective. Since all interfaces are created by connecting ideal PbS and CdS facets, we refer these interfaces as ‘ideal interfaces’.

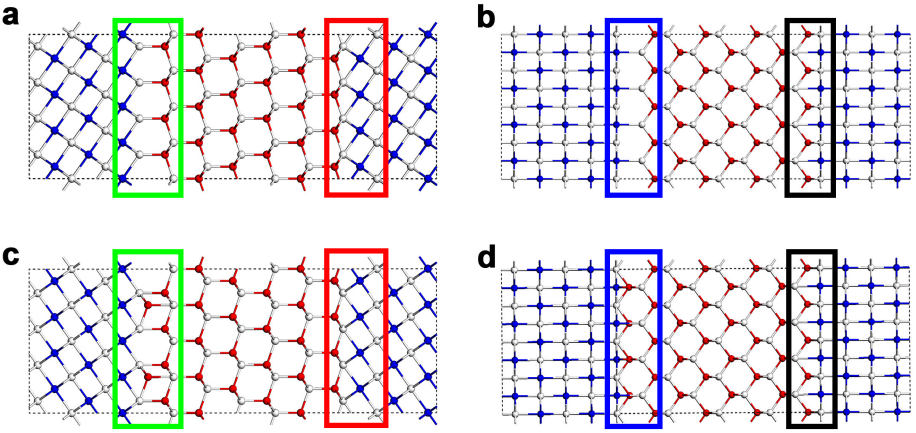

Figure 6.3: **PbS/CdS heterostructures with different interfaces a** A PbS/CdS heterostructure with ideal PbS-(111)/CdS-(111) interfaces. **b** A PbS/CdS heterostructure with ideal PbS-(100)/CdS-(111) interfaces. **c-d** PbS/CdS heterostructures with artificially created point defects at the PbS/CdS interfaces. All heterostructures are in a PbS-[110] pojection. The green, red, blue, and black rectanges indicate the PbS-($\bar{1}\bar{1}\bar{1}$)/CdS-(111), PbS-(111)/CdS-($\bar{1}\bar{1}\bar{1}$), PbS-(100)/CdS-($\bar{1}\bar{1}\bar{1}$), and PbS-(100)/CdS-(111) interfaces, respectively. The white, blue and red spheres represent S, Pb, and Cd, respectively.

The PbS/CdS heterostructures were fully relaxed at zero temperature and zero pressure conditions. The interfacial energy E_{inter} can be calculated as:

$$E_{\text{inter}} = \frac{E_{\text{hs}} - (n_{\text{CdS}} E_{\text{CdS}} + n_{\text{PbS}} E_{\text{PbS}})}{2A} \tag{S5}$$

Where E_{hs} is the total lattice energy of the heterostructure; E_{CdS} and E_{PbS} are the lattice energies of ZB-CdS and RS-PbS per formula unit, respectively; n_{CdS} and n_{PbS} are the number of CdS and PbS pairs in the heterostructure, respectively; A is the area of the interface. Note that the values of interfacial energy are the average of two interfaces created in pairs. The heterostructure with ideal PbS-100/CdS-111 interfaces was not stable during structural optimization. This is because a large dipole moment was created in the heterostructure with non-polar/polar interfaces. The interfacial energy of the ideal PbS-111/CdS-111 interface is also considerably high, since the cations are dense at one interface (red rectangle in Fig. 6.3a) but are sparse at the other (green rectangle in Fig. 6.3a). Therefore, we remove part of the Cd ions from one interface to the other in order to stabilize the structure and to reduce the interfacial energies. We found that, for the heterostructure with PbS-(111)/CdS-(111) interfaces, the interfacial energies became minimum when one fourth of the Cd ions were moved from the PbS-(111)/CdS-($\bar{1}\bar{1}\bar{1}$) to the PbS-($\bar{1}\bar{1}\bar{1}$)/CdS-(111) interface (Fig. 6.3c). For the heterostructure with PbS-(100)/CdS-(111) interfaces, the interfacial energy became minimum when half of the Cd ions were moved from the PbS-(100)/CdS-(111) to the PbS-(100)/CdS-($\bar{1}\bar{1}\bar{1}$) interface (Fig. 6.3d).

6.2.7 Energy Barriers for Cation to Migrate at the PbS/CdS Interface

We use the heterostructures models with artificially created point defects as initial states to calculate the energy barrier for a cation to migrate between two cation sites at the CdS/PbS interfaces. When calculating the energy barriers, the position of the migrating cation was gradually moved along the pathway. The pathway includes straight lines between its initial position (i), an adjoining tetrahedral cation site (t), and an adjoining octahedral cation site (o). For the Pb ion jumping at the PbS-(111)/CdS-(111) interface, we distinguished two situations: (1) a Pb ion jumps to a vacancy, or (2) a Pb ion kicks out a Cd ion and occupies its site.

6.2.8 Simulations of CE at High-Temperature-High-Pressure Conditions

MD simulations for PbS NCs in Cd-PLS solutions at high-pressure-high-temperature conditions were performed. The simulation details are similar to those under zero pressure (see Section 6.2). The only difference is that a hydrostatic pressure was applied to the system and was kept by the NPT ensemble. To investigate the effect of pressure on the Pb→Cd CE, five independent simulations were performed for a PbS colloidal NC at 600 K and different pressures. The pressure range from 0 to 1.00 GPa with an increasing step of 0.25 GPa. At a fixed pressure of 1.0 GPa, MD simulations were performed for the same PbS colloidal NC system at 700, 750, and 800 K.

6.3 Results

6.3.1 Thermodynamic Driving Force

The thermodynamic driving force for CE is controlled by two main factors: the free energy difference between the two materials forming the NCs, and the solubility of both cations in the ligand solution [33, 34]. The former depends on several factors such as the lattice energy, surface energy, size and shape of the NCs, the interfacial energy when forming HNCs, and the entropy of mixing. The dominating factor is the lattice energy difference between ZB-CdS and RS-PbS, as the difference in surface energies and the lattice mismatch between ZB-CdS and RS-PbS are relatively small [95]. During CE, the change in entropy is typically one or two orders of magnitude smaller than the change in enthalpy at ∼500 K [35], and thus the entropy of mixing is also not a dominating factor determining the thermodynamic equilibrium [302]. The lattice energy of ZB-CdS computed using our force field is about 0.3 eV per formula unit (eV/f.u.) less than that of RS-PbS [95]. Therefore, if the PSL-Cd and PSL-Pb interatomic interactions are equivalent (*i.e.*, using non-preferential PSLs) and at a sufficiently high temperature, the relatively low lattice energy of ZB-CdS will promote the Pb→Cd CE process in PbS NCs. MD simulations of a 4.7-nm-sized PbS nanosphere immersed in a non-preferential PSL solution were carried out at 500 K. Pb→Cd CE was indeed observed in our simulations. Figure 6.4a shows that, as a function of simulation time, the number of Pb cations in the parent NC decreases whereas the number of Cd cations increases, clearly demonstrating the exchange of cations. We also observed that the number of S anions remained constant, which indicates that the anionic sublattice is more stable than the cationic sublattice in the NC. The CE process found in the MD simulations is in excellent agreement with the experimental observations [302]: the exchanging Cd ions in the solutions initially cover the surface of the parent NC (*i.e.*, corresponding to the sharp increase of the number of in-going Cd ions during the first few nanoseconds as shown in Fig. 6.4a), while the surface Pb ions in the parent NC are dissolved into the solution. Subsequently, the Cd ions diffuse inwards to the NCs. When the Cd ions occupy the sites of the first few outermost monolayers (MLs), the exchange slows down, forming a PbS/CdS core/shell HNC (see Fig. 6.4e). The formation of the CdS shell impedes the outwards diffusion of the Pb ions from the PbS core. As the exchange slows down, the numbers of in-going Cd ($N_{\mathrm{Cd}}^{\mathrm{NC}}$), the number of remaining Pb in the NC ($N_{\mathrm{Pb}}^{\mathrm{NC}}$), and the exchange ratio (ρ_{Cd}), defined as the number of in-going Cd ions divided by the total number of the cations in the NC ($\rho_{\mathrm{Cd}} = N_{\mathrm{Cd}}^{\mathrm{NC}}/(N_{\mathrm{Cd}}^{\mathrm{NC}} + N_{\mathrm{Pb}}^{\mathrm{NC}})$, grey circles in Fig. 6.4b-c), becomes nearly constant after a few tens of nanoseconds. The PbS/CdS core/shell HNCs with higher exchange ratios (*e.g.*, the final configuration of an exchanged HNC at 600 K in a MD simulation of 100 ns in Fig. 6.4i) have a structure and morphology which is very similar to those of experimentally observed core/shell HNCs, which is apparent from HRTEM images of PbE/CdE configurations obtained in CE experiments [28, 282, 305] (see Figs. 6.4j-l).

The preferential dissolution of the cations in solutions with different

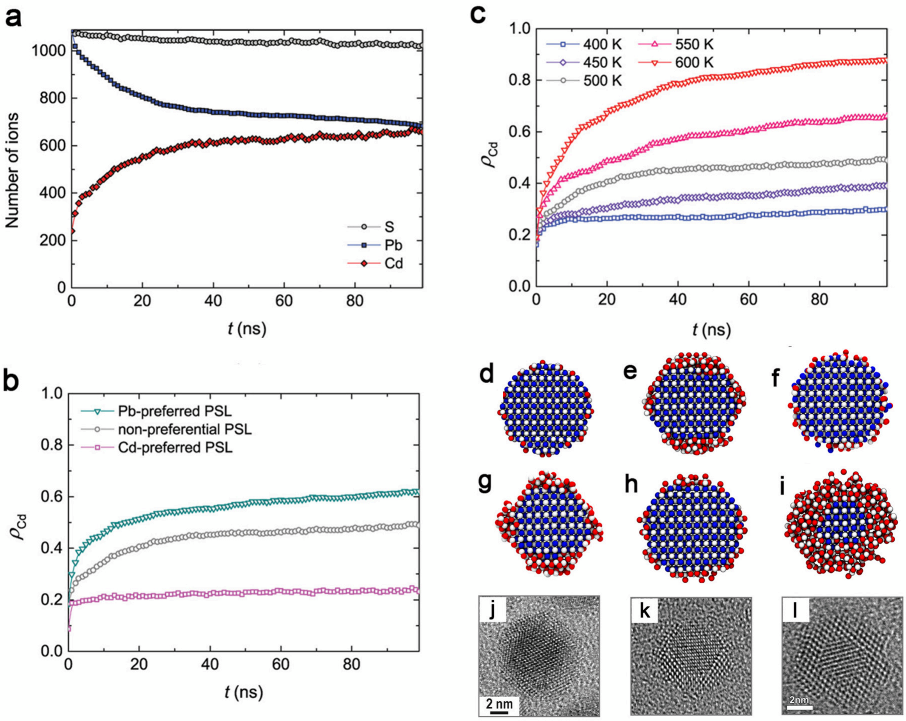

Figure 6.4: The Pb→Cd CE process in a 4.7-nm-sized PbS NC using different PSLs and at different temperatures. (a) Number of in-going Cd ions (red diamonds), and remaining Pb ions (blue squares) and S ions (grey circles) in the parent PbS NCs as a function of simulation time. MD simulation were performed at 500 K with non-preferential PSLs. (b-c) Time evolution of exchange ratio ρ_{Cd} (the ratio of in-going Cd ions over the total number of cations in the NC). (b) Simulations performed at 500 K with different PSLs. A constant value of ρ_{Cd} (~0.2) for the simulation with Cd-preferred PSLs indicates that CE did not take place. The low fraction of Cd ions corresponds to those were adsorbed at the NC surface. (c) Simulation performed using non-preferential PSLs at different temperatures. (d-i) Snapshots of the RS-(110) sections of the NCs in 100 ns MD simulations: (d) initial configuration; (e-i) final configurations of 100 ns simulations at 500 K with non-preferential (e), Cd-preferred (f), and Pb-preferred PSLs (g), and those with non-preferential PSLs at 400 K (h) and 600 K (i). The white, blue and red spheres represent S, Pb, and Cd, respectively. (j-l) High-resolution transmission electron microscopy (HRTEM) images of PbE/CdE core/shell HNCs achieved by experimental CE, in a [110] projection. (j) A 9-nm-sized PbS/CdS core/shell HNC, image adapted with permission from Ref. [305] (copyright 2014 American Chemical Society); (k) A 5.6-nm-sized PbSe/CdSe core/shell HNC, image adapted with permission from Ref. [282] (copyright The Royal Society of Chemistry 2011); (l) A 6.6-nm-sized PbTe/CdTe core/shell HNC, image adapted with permission from Ref. [28] (copyright 2009 American Chemical Society).

ligands has a crucial role in determining the direction and exchange ratio of CE. Using the same system and temperature (*i.e.*, the 4.7-nm-sized PbS NC immersed in the Cd-PSL solution at 500 K), we investigate the influence of different ligand solutions on the CE process by considering different PSL-cation interactions. For Pb-preferred, non-preferential, and Cd-preferred PSL solutions, the exchange ratio ρ_{Cd} as a function of simulation time is shown in Fig. 6.2b. As shown in this figure, Pb→Cd CE can be significantly accelerated using a Pb-preferred solution, and it can also be completely prohibited using a Cd-preferred solution. Note that a small amount of Cd ($\rho_{\mathrm{Cd}} \sim 20\%$) was also found in the NC with the Cd-preferred PSLs. These Cd ions did not penetrate into the NC but were adsorbed at the NC surface (Fig. 6.4f).

We also found that, immersing a ZB-CdS NC in a solution containing Pb ions and Cd-preferred PSLs, the system underwent a reverse Cd→Pb CE (Fig. 6.5). The reverse CE did not take place using a non-preferential or a Pb-preferred PSL solution. A way to achieve both the forward and backward Pb⇔Cd CE in experiments is to change the type of ligand: Cd-oleates are often chosen as the cation-ligands solutions to achieve Pb→Cd CE [36, 37, 302], while aqueous Pb nitrate solutions, $\mathrm{PbCl_2}$-oleylamine, and Pb-oleates-oleylamine have been used to achieve the reverse CE process [306–309].

Temperature is another key factor for determining the equilibrium and the exchange ratio of CE. Independent MD simulations for PbS nanospheres immersed in non-preferential PSL solutions were performed at temperatures ranging from 400 to 600 K. The CE process is faster at higher temperatures resulting in a more complete Pb→Cd replacement (Fig. 6.4c). At 600 K, nearly 90% of the cations in the NC was replaced by Cd within 100 ns, and a CdS shell with a thickness about four MLs was formed (Figs. 6.4c,i). In experiments, high temperatures often lead to severe damage and distortion of the NCs (amongst others, Ostwald ripening can take place) [37, 302]. In the simulations, complete damaging of the PbS NC was also observed at 700 K, whereby the whole NC dissolved in the solution. Note that temperatures used in the MD simulations should not be directly compared with those in experiments. The time scale in our MD simulations is generally of the

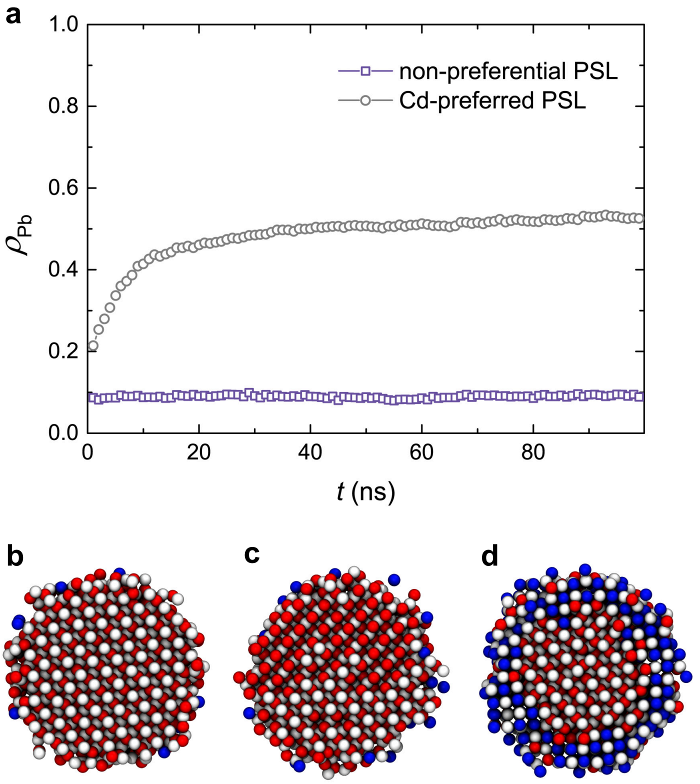

Figure 6.5: Reverse Cd→Pb CE in a ZB-CdS NC. (a) Time evolution of exchange ratio ρ_{Pb} (the ratio of in-going Pb ions over the total number of cations in the NC). Simulations were performed at 550 K with the number of non-preferential (grey circles) and Cd-preferred (purple squares) PSLs. The constant value of $\rho_{\mathrm{Pb}} \sim 0.1$ for the simulation with non-preferential PSLs indicates that CE did not take place (also see the final configuration in (c)). (b-d) Initial (b) and final (c-d) configurations of the ZB-CdS NC in a 100 ns simulation at 550 K with non-preferential (c) and Cd-preferred PSLs (d). The white, blue and red spheres represent S, Pb, and Cd, respectively.

order of hundreds of nanoseconds, which is much shorter than a typical timescale of the Pb→Cd CE experiments (mins∼hrs) [27, 28, 36, 37, 302]. Accordingly, a higher temperature is required in our simulations in order to accelerate the CE process.

6.3.2 Self-Limiting Exchange

One of the appealing features of CE at the nanoscale is the fast exchange rate compared to the process at the macroscopic scale. Nonetheless, the Pb→Cd exchange is often reported to be self-limiting. Although complete Pb→Cd exchange has been experimentally reported [23, 27, 302], accurate control, high temperatures, and long times are required. Figure 6.6a shows the time evolution of the averaged volume-scaled exchange rate η at the first four outermost MLs of the PbS NC from the MD simulations at 550K with non-preferential PSLs. The CE process takes place in a layer-by-layer fashion. The exchange front moves from the first outermost ML to the second ML at 20∼40 ns and further proceeds to the third outermost ML from ∼50 ns onward (Fig. 6.6a). The exchange rate of the fourth layer is always zero, suggesting that the exchange front has not yet reached the fourth ML in 100 ns. The overall exchange rate η significantly decreases as the exchange front moves inwards. This is consistent with the averaged root mean square motion (RMSM) calculated for different ionic species as a function of r (r is the distance from the initial position of an ion to the centre of the NC) in Fig. 6.6b. To clarify the ionic positions in the PbS/CdS core/shell structure, the radial density of each ionic species are plotted in the upper left inset of Fig. 6.6b. The RMSM of all types of ions increases as the ions are closer to the NC surface, indicating a faster CE process at the surface than on the inside. Obviously, the large surface-to-volume ratio of nanostructures leads to a swift CE process at the nanoscale, but the spherical morphology of the PbS parent NCs and the layer-by-layer fashion of the Pb→Cd CE process determine its self-limiting nature. This has also been reported experimentally for an analogous Cd→Zn CE process in CdSe NCs [38].

It is instructive to also point out that the radial density of each atom

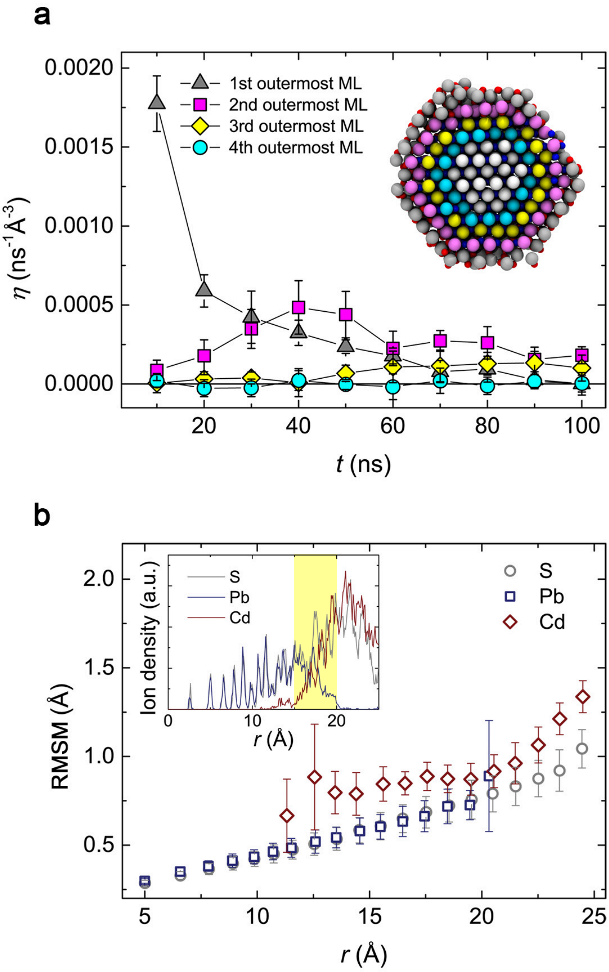

Figure 6.6: Exchange rate and atomic mobility analyses of the Pb→Cd CE. (a) Time evolution of the averaged volume-scaled exchange rate η for the four outermost atomic monolayers (MLs). Data was collected from 10 independent 100 ns MD simulations of a PbS NC at 550 K. The upper right inset shows the final configuration of a NC's RS-(110) section from one of the MD simulations. The S ions are coloured according to the colour code of the different outermost MLs. The small red and blue spheres are Cd and Pb, respectively. (b) Averaged RMSF of S (grey circles), Pb (blue squares) and Cd (red diamonds) as a function of r (r is the distance between the ion and the centre of the NC). The upper left inset shows the ion density as a function of r. The yellow region labels the $\mathrm{Cd}_x\mathrm{Pb}_{1-x}\mathrm{S}$ mixed phase domain between the PbS core and the CdS shell. Data were sampled in the last 100 ps of the ten independent 100 ns MD simulations.

type (upper left inset of Fig. 6.6b) indicates a pure PbS domain ($r \leq 15$ Å), a $Cd_xPb_{1-x}S$ mixed phase domain (15 Å $< r <$20 Å), and a pure CdS domain (20 Å $\leq r <$ 24 Å). Considering the inhomogeneity in PbS/CdS HNCs, the mixed phase layer with a thickness of 5 Å is relatively thin. It has been also experimentally shown that PbS/CdS HNCs obtained by CE have a sharp PbS/CdS boundary [28, 37]. Unlike systems containing materials with the same crystal structure which easily form mixed phases or solid solutions (*e.g.*, the CdSe/ZnSe [38] and CdSe/CdS/ZnS [310] systems), PbS and CdS in HNCs undergo phase separation even at relatively high temperatures [35, 282].

6.3.3 Kinetics: A Revised Vacancy-Mediated Mechanism

To obtain a better understanding of the Pb→Cd CE, it is crucial to understand the kinetics. Based on a variety of experimental data, a hypothetical vacancy-mediated mechanism has been generally accepted [27, 35, 302]. In this mechanism, it was claimed that Cd vacancies first form at the surface of NCs and migrate further towards the PbE/CdE interface. These vacancies transport the Pb ions from the PbS core edges to the surrounding solutions. Although the formation and migration energies of a Cd vacancy can be largely reduced on a NC surface, the probability that a Pb ion is transferred by such a backward and forward motion of a vacancy is rather small. In addition, this vacancy-mediated mechanism also contradicts to generally accepted knowledge that point defects, rather than moving towards the inside of NCs, should be easily annealed out of NCs at a high temperature [311].

By tracing the trajectories of the Pb ions leaving the PbS core, we are able to reveal the mechanism of Pb→Cd exchange at the atomic level. We propose a revised vacancy-mediated mechanism for Pb→Cd CE. Figures 6.7 a and b show typical MD snapshots when a Pb ion (the green spheres) leaves from a PbS-(111) and -(100) facet, respectively. The Pb ion from the PbS-(111) facet jumps to an adjoining tetrahedral cation site (a tetrahedrally coordinated site with four nearest neighbour anions), whereas the Pb ion from the PbS-(100) facet jumps to an octahedral cation site (an octahedrally coordinated site with six nearest neighbour anions). In both cases, a cation vacancy forms at the outer layers (indicated by open diamonds in Figs 6.7 a and b) before the Pb ions jumped into them, partially supporting the vacancy-mediated mechanism that forming a Cd vacancy is a required non condition for the jumps of Pb ions. The energy barrier for a Pb ion to jump without a vacancy (*i.e.*, the Pb ion kicks out a Cd ion and occupies its position) is ~1.8 eV, which is much higher than that with a Cd vacancy already present (0.41~1.25 eV), indicating that the 'kick-out' type of motion is unlikely to occur in Pb→Cd exchange (Fig. 6.8). It is important to note that the formation of Cd vacancies in our simulations differs from the previous vacancy-mediated mechanism. During the CE process, Cd vacancies do not form at the NC surfaces and migrate to the PbS/CdS interfaces, but automatically form at the PbS/CdS interfaces. The automatic formation of Cd vacancies at the PbS/CdS interface can be achieved by two ways: (1) a Cd ion at a PbS/CdS interface jumps to an adjoining octahedral cation site forming an interstitial and a vacancy (a Frenkel pair), or (2) after a Pb ion leaves its site during CE, no other cation occupies the vacancy which is left behind. The interfacial energies of the ideal PbS-(100)/CdS-(111) and PbS-(111)/CdS-(111) interfaces and those with artificially created point defects are listed in Table 6.2. The results show that interfaces with Cd vacancies and interstitials indeed have lower interfacial energies than the ideal ones. Our findings confirm that interfaces play an important role in the cation exchange process at the nanoscale [27, 35, 312].

It has been reported that the Cd→Cu/Ag CE processes show a cooperative behaviour [313, 314], whereby exchanged Cu/Ag ions decrease the energy barrier for a nearby guest ion (Cd) leaving its site. Similar phenomena of cooperativity has also been found in our simulations. We have carefully examined the trajectories of about fourty individual Pb ions leaving the PbS core. When these Pb ions were leaving the PbS core, exchanged Cd ion(s) could always be found at the next nearest neighbor sites of the Pb ions (*e.g.*, see Figs 6.7a and b). To understand this cooperative behaviour, we calculated the reduction of the energy barrier for Pb ions leaving their sites with the assistance of one nearby Cd impurity at the interfaces (Fig. 6.8). As shown in Fig. 6.8, with one nearby exchanged

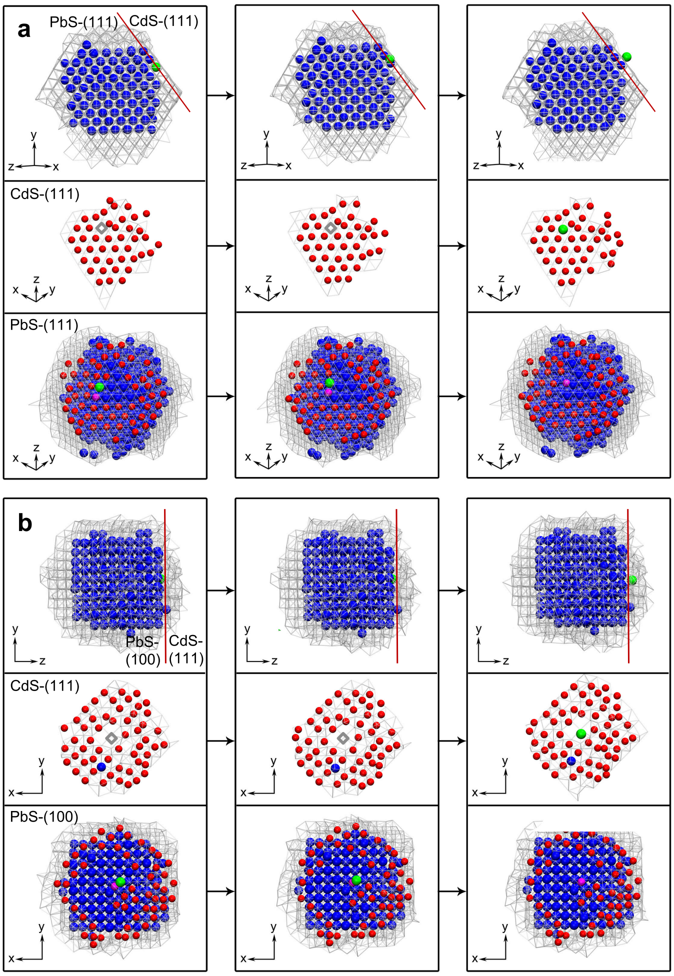

Figure 6.7: Typical MD snapshots of the Pb→Cd CE mediated by Cd vacancies and impurities. (a) CE taking place on a PbS-(111)/CdS-(111) interface. (b) CE taking place on a PbS-(100)/CdS-(111) facet. The snapshots are from MD simulations of a PbS NC at 550 K. The blue and red spheres are Pb and Cd, respectively; The anion sublattice is shown with white lines (framework consisting of S-S bonds); The open diamonds indicate Cd vacancies. The labelled Pb ions (green) on the edge of the PbS cores jumped to a outer CdS layer, the sites which were left behind were occupied by nearby Cd ions (the magenta spheres). The first two columns and the third column in (a-b) show the moments before and after the Pb ion left its site, respectively. The first row in (a-b) show the side-view of the NC where Cd ions are not shown for clarity. The red lines indicate the PbS/CdS interface where CE took place. The second and the third rows in (a-b) show the bird's-eye view of the CdS and PbS facets where CE took place, respectively.

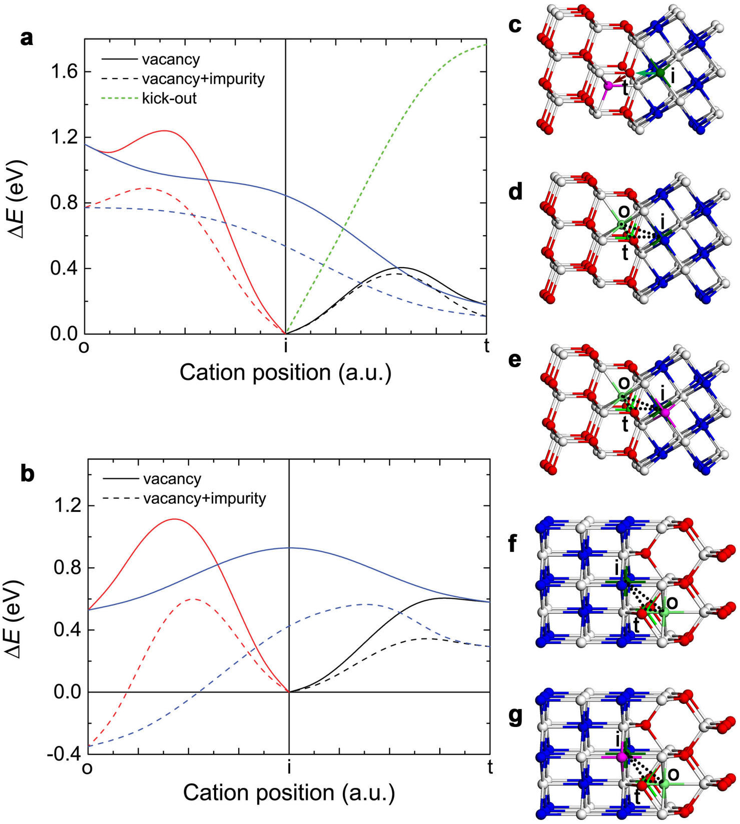

Figure 6.8: Energy barriers for a Pb ion to jump out of the PbS facet at different PbS/CdS interfaces at zero temperature. (a-b) Energy variation (ΔE) as a function of the position of the jumping Pb ion at a PbS-(111)/CdS-(111) (a) and a PbS-(100)/CdS-(111) (b) interface. The Pb ions jump between the initial position (i), a tetrahedrally coordinated (t), and an octahedrally coordinated (o) cation site. The red, black, and blue lines in (a-b) correspond to the pathways i-o, i-t, and o-t, respectively. (c-g) Pathways of the jumping Pb ion at different interfaces. The white, blue and red spheres represent S, Pb, and Cd, respectively. (c) a 'kick-out' type of jump at a PbS-(111)/CdS-(111) interface corresponding to the green short dashed line in (a). The Pb ion (green) kicks out a Cd ion and occupies its site, and the Cd ion becomes an interstitial (magenta). The green and dark red arrows indicate the pathways of the Pb and Cd ions, respectively. (d) and (f) show the jumps of the Pb ion (green) which are mediated by a Cd vacancy (at the position t) at a PbS-(111)/CdS-(111) (solid lines in (a)) and a PbS-(100)/CdS-(111) (solid lines in (b)) interface, respectively. (e) and (g) show the jumps of the Pb ion (green) which are mediated by both a Cd vacancy (at the position t) and a Cd impurity (magenta) at a PbS-(111)/CdS-(111) (dashed lines in (a)) and a PbS-(100)/CdS-(111) (dashed lines in (b)) interface, respectively. The dotted lines in (d-g) indicate the pathways of the jumping Pb ion.

Table 6.2: Interfacial energies of the ideal PbS-(111)/CdS-(111) and PbS-(100)/CdS-(111) interfaces and those with point defects. The value of the interfacial energies is the average of the two interfaces created in one heterostructure. The interfaces with point defects were created to achieve the minimum interfacial energies. The interfacial energies are in eV/Å^2.

	ideal	with defects
PbS-(111)/CdS-(111)	not stable	0.74
PbS-(100)/CdS-(111)	2.13	0.68

Cd ion, the barrier for a Pb jumping to an adjoining octahedral site at a PbS-(100)/CdS-(111) interface is reduced from 1.12 eV to 0.66 eV, and at a PbS-(111)/CdS-(111) interface it is reduced from 1.25 eV to 0.89 eV. These barrier reductions are able to increase the probability of the Pb hopping by 4∼5 orders of magnitude at 500 K.

After a Pb ion moves away, a Pb vacancy is created. This Pb vacancy can be occupied by a nearby Cd or Pb ion. A Pb ion at a PbS-(111) facet needs to overcome a considerably large energy barrier of about 1.8 eV to occupy the Pb vacancy (Fig. 6.9c), thus this motion is unlikely to take place. An exchanged Cd ion on a PbS-(111) facet, however, only needs to overcome a barrier of about 0.38 eV to occupy the Pb vacancy (Fig. 6.9). The barrier to a Pb ion on a PbS-(100) facet migrating to the Pb vacancy is 0.93 eV, and that to a Cd ion is only 0.37 eV (Fig. 6.9). The low barriers for Cd ion migrating at the PbS/CdS interfaces indicate exchanged Cd ions have high mobility and that they are able to jump between adjoining cation sites. Figure 6.10a shows typical MD snapshots of a PbS-(100)/CdS-(111) interface, at which an exchanged Cd ions (magenta) moved across a few adjacent cation sites. Such highly mobile Cd ions at the PbS-(100)/CdS-(111) interfaces could have very long-distance in-plane migration, thus affecting Pb ions in the central area of the (100) plane. The horizontal in-plane migration of Pb ions at a PbS-(111)/CdS-(111) interface is more difficult and has not been observed in our MD simulations.

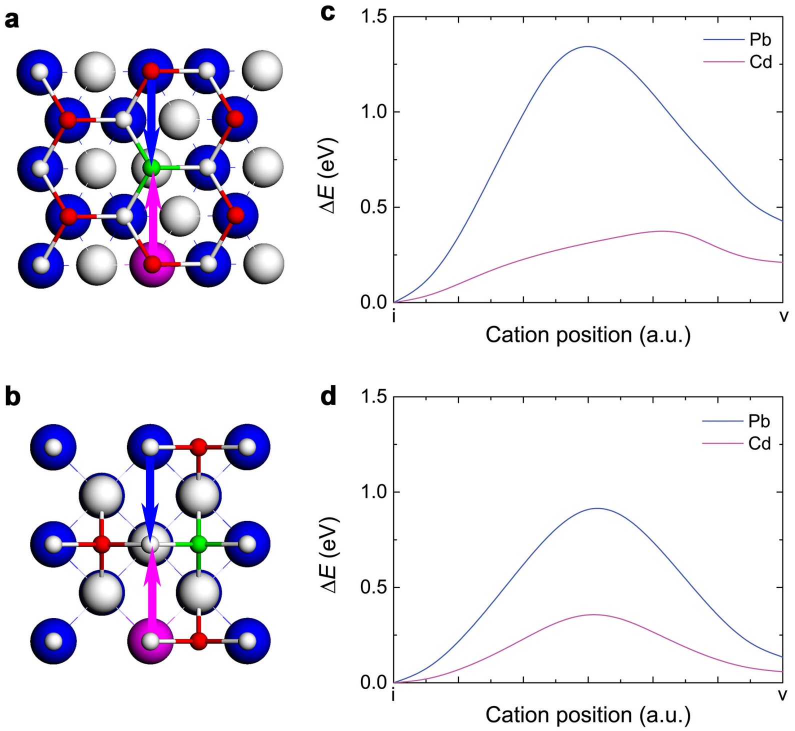

Figure 6.9: Energy barriers for a cation to migrate at different PbS/CdS interfaces at zero temperature. (a-b) Pathways of the migrating cation at different interfaces. (a) The PbS-(111)/CdS-(111) interface shown in a PbS-[111] projection. (b) The PbS-(100)/CdS-(111) interface shown in a PbS-(100) projection. The larger spheres represent the PbS cores while the bonds and the smaller spheres represent the CdS regions. The white, blue and red spheres represent S, Pb, and Cd, respectively. The green spheres are the Pb ions jump out of the PbS cores and left behind a vacancy. The magenta spheres are the Cd impurities on the edge of the PbS cores. The magenta and blue arrows indicate the pathways of the migrating Cd and Pb ions from their initial positions (i) to the vacancy (v), respectively. (c-d) Energy variation (ΔE) as a function of the position of the migrating cations at a PbS-(111)/CdS-(111) (c) and a PbS-(100)/CdS-(111) (d) interface. The blue and magenta lines correspond to the migrating Pb and Cd ions, respectively.

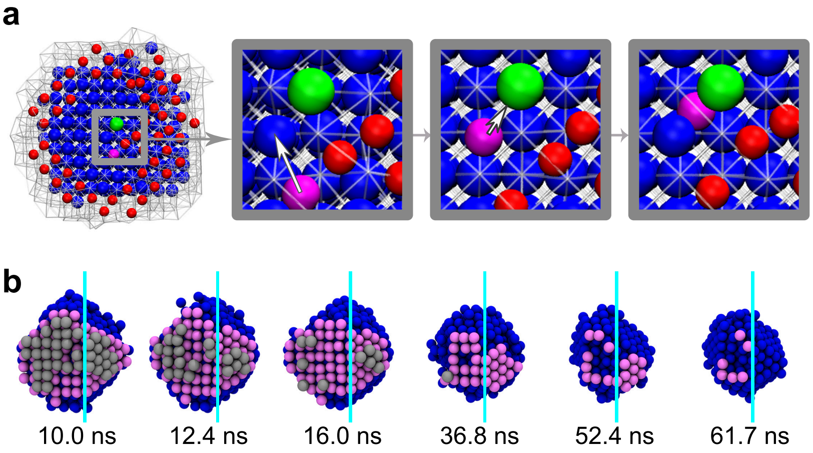

Figure 6.10: In-plane migration of cations at the PbS/CdS interface at 550 K. (a) Typical MD snapshots showing migration of Cd ions at a PbS-(100) facet. The blue and red spheres are Pb and Cd ions, respectively; The anion sublattice is shown with white lines (framework consisting of S-S bonds). The labelled Cd ion (magenta) moved through a few cation sites on the PbS-(100) facet and is able to affect the Pb ion in the center area of the PbS-(100) (the green sphere). The white arrows indicate the migrating directions of the Cd ion. (b) Typical MD snapshots of a shrinking PbS core. Only Pb ions are shown and two atomic layers are distinguished by different colours (grey and pink). The cyan lines indicate the boundary between a RS-(100) surface and a RS-(111) surface.

Consequently, the exchange process is expected to take place in a different manner at the PbS-(100)/CdS-(111) and PbS-(111)/CdS-(111) interfaces. Figure 6.10b shows the time evolution of a Pb sublattice in the NC. Different routes of Pb extraction can be distinguished at the PbS-(111) and (100) facets of the core edges: Pb ions were disappearing in a random pattern at the PbS-(100) interface, whereas, Pb ions at PbS-(111) facets were leaving by a border-to-centre fashion (*i.e.*, Pb on the edge leave first and the outermost PbS-(111) layer gradually shrink to the centre).

6.4 Discussion

The exchange rate in our simulations is faster than that in experiments, and the time scale in our simulations is a few of orders of magnitude shorter. The main reasons for the abnormal fast Pb→Cd CE in our simulations are the higher reaction temperature and higher concentrations of Cd in the solution compared to the experiments. In Pb→Cd CE experiments of PbS NCs, the reaction temperature is typically in the range of 100 to 200 °C (373-473 K). In our simulations, the highest temperature is 600 K in order to accelerate the CE process. Such a high temperature will increase the probability of cation jumps by two to six orders of magnitude. The coarse-grained PSL model was used to mimic the ligand and solvent molecules. The size of a PSL is much smaller than that of actual ligands used in CE experiments. The number of the guest cations (Cd) is set equal to the number of PSLs. Therefore, the concentration of guest cations in the solution in simulations is higher than that in experiments, which is also expected to cause a faster exchange in the simulations. In addition, it should be noted that our simulations are only able to show the initial stages (the first few of hundred nanoseconds) of the CE process. Compared to the exchanged NCs in experiments that has formed CdS shells with a thickness of 1∼2 nm, the exchanged NC at 400 K (within the temperature range used in CE experiments) only has formed an incomplete and thin layer of CdS (thickness of the shell less than 0.3 nm) after 100 ns (Fig. 6.4h), thus the CE took place to a lesser extent. To show a CE process for this

NC in a simulation at 400 K with a similar degree of exchange as those in experiments, the simulation time needs to be extremely long, which is not computationally feasible.

Increasing the temperature is an effective way to accelerate the CE process, however, it has been reported that Ostwald ripening takes place by a direct heating of colloidal PbS NCs at 473 K, damaging the monodispersion of the NCs [37]. A multiple step heating scheme [27, 37] has been used for CE experiments at high temperatures whereby the NCs are protected by CdS shells that form at a lower temperature. We did find significant dissolution of S ions in our simulations at high temperatures, however, Ostwald ripening could not be directly observed in our simulations since a single NC was considered. The dissolved S anions may also recrystallized on the other parts of the same NC with cations in the solution, thus enabling massive migration of anions and reconstruction of PbE/CdE HNCs. This phenomenon becomes more important at high temperatures and/or with active ligands, in some extreme cases PbE NCs or PbE/CdE core/shell HNCs may transform to a Janus-like heterostructure [282, 308, 315].

Besides the multiple step heating scheme, we found that increasing the pressure could be an alternative way to preserve NCs at elevated temperatures in order to accelerate the CE processes and to achieve complete compositional conversions. The Pb→Cd CE process cannot be accelerated by merely applying a hydrostatic pressure to the solution (Fig. 6.11a), however, an increased hydrostatic pressure is able to increase the melting point of ionic semiconductor solids [316] and their stability to high temperatures. For example, only five Pb ions remained in the exchanged NC ($\rho_{\mathrm{Cd}} = 0.997$) in a MD simulation of 100 ns at 750 K and a hydrostatic pressure of 1 GPa (Fig. 6.11b). At standard pressure the NC would have been completed damaged upon reaching a temperature of 700 K, whereas, the exchanged NC remains solid phase and retains a quasi-spherical morphology at high-temperature-high-pressure conditions ($p = 1.0$ GPa, $T \leq 800$ K, Fig. 6.11b). Our simulations therefore predict that a high-pressure-high-temperature approach is a promising method to control the rate and degree of the Pb→Cd CE process.

As CdS and PbS have different crystal structures, a structural transition

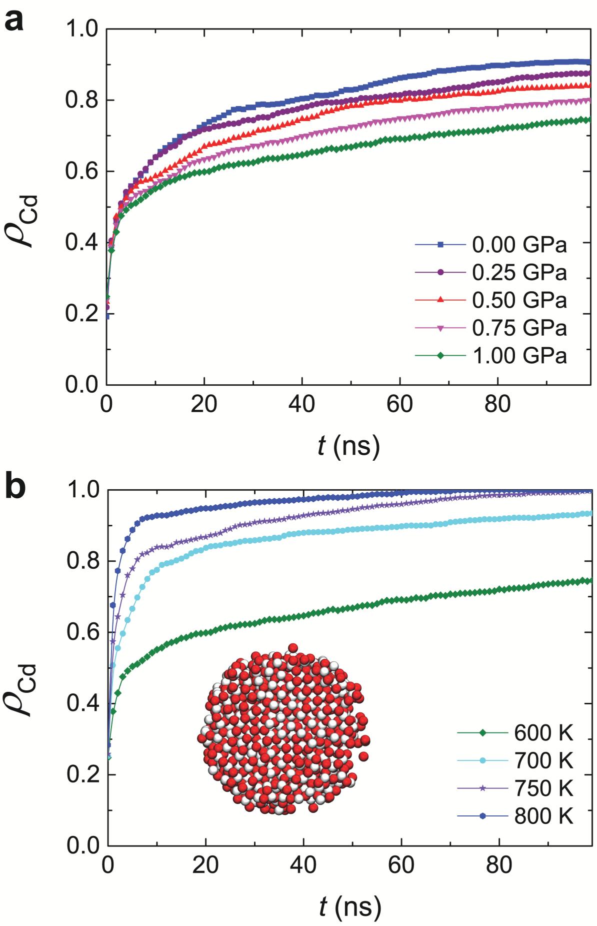

Figure 6.11: Pb→Cd CE at high-temperture-high-pressure conditions. (a) Time evolution of exchange ratio ρ_{Cd} at 600 K and different hydrostatic pressures in the range of 0.00∼1.00 GPa. (b) Time evolution of exchange ratio ρ_{Cd} under at different temperatures of 600, 700, 750 and 800 K and 1.00 GPa. Simulations were performed with Pb-preferential PSLs for 100 ns. The inset in (b) shows the final configuration of an exchanged NC at 800 K and 1.00 GPa in a CdS-[001] pojection. The white and red spheres represent S and Cd, respectively.

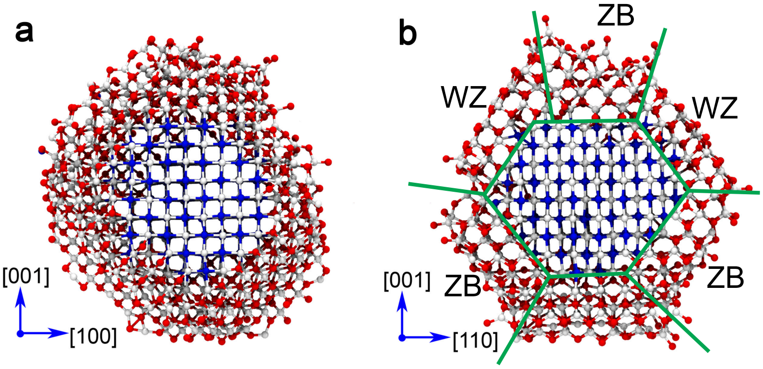

Figure 6.12: Final configurations of a CdS/PbS core/shell HNC. The configuration is from a MD simulation performed at 550 K with Pb-preferred PSLs for 300 ns. The core/shell HNC is shown along PbS-[010] in (a) and along PbS-[011] direction in (b). The green lines in (b) indicate the boundaries between the WZ-CdS, ZB-CdS, and RS-PbS domains.

must take place during a CE process. The most stable phases of CdS, wurtzite (WZ) and ZB, have almost the same cohesive energy (the difference between the cohesive energies of these two CdS polymorphs is about 1 meV/f.u. according to DFT calculations [95]). During the CE process of lead and cadmium chalcogenides nanostructures, however, the RS-to-ZB transition has been more frequently observed experimentally than the RS-to-WZ transition [23, 27, 28, 35, 281] (Fig. 6.12). The latter requires an extra step of anionic sublattice slips [68] as the former only requires slip of the cationic sublattice [95]. Therefore, the RS-to-ZB transition has a lower energy barrier than the RS-to-WZ transition. In our simulations, almost equal amounts of the WZ and ZB domains were found in the CdS shell in an exchanged HNC (Fig. 6.12). This discrepancy between experiments and simulations may be attributed to CdS force field as the stability of ZB phase is slightly underestimated compared to DFT calculations [95]. However, the result of the competition between the RS-to-ZB and RS-to-WZ transitions in the Pb→Cd CE depends on many other factors, including the morphology of initial parent NCs, types of ligand and solvent, temperatures, nucleation energies. For instance, the WZ stacking faults and even direct RS-to-WZ transition have been observed in CE experiments [23, 27, 28, 35, 281]. In our simulations, most of Cd ions were located at the tetrahedral sites (ZB or WZ), and only those at or near the PbS/CdS interfaces may jump between tetrahedral and octahedral sites. It has been reported that CdS shells may remain in a metastable RS phase during CE processes [305], which has not been observed in our simulations.

6.5 Conclusions

Classical MD simulations were used to investigate Pb→Cd CE in colloidal PbS NCs. The cation-ligands solutions were coarse-grained by a PSL model, allowing us to study this large system for long time scales. The main driving force of the Pb→Cd CE process is the competition of the ionic crystal lattice energies and the cations solvent solubility. By adjusting the PSL-cation interatomic interactions (analogous to changing the cation-ligand solutions in experiments) and the temperature, the direction and rate of the CE process can be controlled. Our simulation results reveal that the Pb→Cd CE process is mediated by the Cd vacancies automatically formed at the PbS/CdS interfaces and is assisted by the exchanged Cd impurities. Highly mobile surface Cd ions accelerate the formation of Cd vacancies and interstitials, which enables the transportation of Pb ions by sequential jumps of cations. The energy barrier for exchanged Cd ions migrating in the PbS-(100) and -(111) facets is lower than that for Pb ions, and therefore, Cd ions show higher mobility than other ions at the PbS/CdS interfaces and drive the exchange fronts into the inside of the NCs. Our study provides a profound insight into the physics underlying the Pb→Cd CE at the atomic level. The all-atom/coarse-graining approach is able to effectively reveal both the thermodynamics and kinetics of the Pb→Cd CE, and, more importantly, this model can also be adapted to investigate other types of CE (*e.g.*, Cd→Cu and Zn→Ag) or other synthesis techniques (*e.g.*, hot injection, seed growth, and vapour-liquid-solid growth).

Finally, the simulations also predict that high-pressure-high-temperature conditions can greatly enhance the cation exchange rate. To date, several key questions remain unclear, such as: What is the optimal ligand solution and temperature to yield complete Pb→Cd CE? How can the thickness and uniformity of the CdE shell be completely controlled? Our approach provides opportunities to further address these questions, and we anticipate that the coarse-grained PSL model will be extended and further improved.

References

[1] Feynman, R.P. There's plenty of room at the bottom. *Eng. and Sci.*, 23, 1960: 22–36.

[2] Portney, N.G. and Ozkan, M. Nano-oncology: Drug delivery, imaging, and sensing. *Anal. Bioanal. Chem.*, 384, 2006: 620–630.

[3] Musil, J. Hard and superhard nanocomposite coatings. *Surf. Coat. Technol.*, 125, 2000: 322–330.

[4] Lal, S.; Link, S.; and Halas, N.J. Nano-optics from sensing to waveguiding. *Nature Photon.*, 1, 2007: 641–648.

[5] Katz, D.; Wizansky, T.; Millo, O.; Rothenberg, E.; Mokari, T.; and Banin, U. Size-dependent tunneling and optical spectroscopy of CdSe quantum rods. *Phys. Rev. Lett.*, 89, 2002: 086801.

[6] Sapra, S. and Sarma, D.D. Evolution of the electronic structure with size in II-VI semiconductor nanocrystals. *Phys. Rev. B*, 69, 2004: 125304.

[7] Roucoux, A.; Schulz, J.; and Patin, H. Reduced transition metal colloids: A novel family of reusable catalysts? *Chem. Rev.*, 102, 2002: 3757–3778.

[8] Kruk, M. and Jaroniec, M. Gas adsorption characterization of ordered organic-inorganic nanocomposite materials. *Chem. Mater.*, 13, 2001: 3169–3183.

[9] Son, D.H.; Hughes, S.M.; Yin, Y.; and Alivisatos, A.P. Cation exchange reactions in ionic nanocrystals. *Science*, 306, 2004: 1009–1012.

[10] Yin, Y. and Alivisatos, A.P. Colloidal nanocrystal synthesis and the organic–inorganic interface. *Nature*, 437, 2005: 664–670.

[11] Xia, Y.; Xiong, Y.; Lim, B.; and Skrabalak, S.E. Shape-controlled synthesis of metal nanocrystals: Simple chemistry meets complex physics? *Angew. Chem. Int. Edit.*, 48, 2009: 60–103.

[12] Sau, T.K. and Murphy, C.J. Room temperature, high-yield synthesis of multiple shapes of gold nanoparticles in aqueous solution. *J. Am. Chem. Soc*, 126, 2004: 8648–8649.

[13] MURRAY, C.B.; NORRIS, D.J.; and BAWENDI, M.G. Synthesis and characterization of nearly monodisperse CdE (E= sulfur, selenium, tellurium) semiconductor nanocrystallites. *J. Am. Chem. Soc*, 115, 1993: 8706–8715.

[14] DE MELLO DONEGÁ, C.; LILJEROTH, P.; and VANMAEKELBERGH, D. Physicochemical evaluation of the hot-injection method, a synthesis route for monodisperse nanocrystals. *Small*, 1, 2005: 1152–1162.

[15] MANTHIRAM, K.; BEBERWYCK, B.J.; TALAPIN, D.V.; and ALIVISATOS, A.P. Seeded synthesis of CdSe/CdS rod and tetrapod nanocrystals. *J. Vis. Exp.*, 82, 2013.

[16] NYAMEN, L.D.; PULLABHOTLA, V.S.R.R.; NEJO, A.A.; NDIFON, P.T.; WARNER, J.H.; and REVAPRASADU, N. Synthesis of anisotropic PbS nanoparticles using heterocyclic dithiocarbamate complexes. *Dalton Trans.*, 41, 2012: 8297–8302.

[17] MANNA, L.; SCHER, E.C.; and ALIVISATOS, A.P. Synthesis of soluble and processable rod-, arrow-, teardrop-, and tetrapod-shaped CdSe nanocrystals. *J. Am. Chem. Soc.*, 122(51), 2000: 12700–12706.

[18] KUDERA, S.; CARBONE, L.; CASULA, M.F.; CINGOLANI, R.; FALQUI, A.; SNOECK, E.; PARAK, W.J.; and MANNA, L. Selective growth of PbSe on one or both tips of colloidal semiconductor nanorods. *Nano Lett.*, 5(3), 2005: 445–449.

[19] MILLIRON, D.J.; HUGHES, S.M.; CUI, Y.; MANNA, L.; LI, J.; WANG, L.W.; and ALIVISATOS, A.P. Colloidal nanocrystal heterostructures with linear and branched topology. *Nature*, 430, 2004: 190–195.

[20] DEKA, S.; MISZTA, K.; DORFS, D.; GENOVESE, A.; BERTONI, G.; and MANNA, L. Octapod-shaped colloidal nanocrystals of cadmium chalcogenides via "one-pot" cation exchange and seeded growth. *Nano Lett.*, 10, 2010: 3770–3776.

[21] ARCINIEGAS, M.P.; KIM, M.R.; DE GRAAF, J.; BRESCIA, R.; MARRAS, S.; MISZTA, K.; DIJKSTRA, M.; VAN ROIJ, R.; and MANNA, L. Self-assembly of octapod-shaped colloidal nanocrystals into a hexagonal ballerina network embedded in a thin polymer film. *Nano Lett.*, 14, 2014: 1056–1063.

[22] Sliem, M.A.; Chemseddine, A.; Bloeck, U.; and Fischer, R.A. PbSe nanocrystal shape development: oriented attachment at mild conditions and microwave assisted growth of nanocubes. *Cryst. Eng. Comm.*, 13, 2011: 483–488.

[23] Boneschanscher, M.P.; Evers, W.H.; Geuchies, J.J.; Altantzis, T.; Goris, B.; Rabouw, F.T.; van Rossum, S.A.P.; van der Zant, H.S.J.; Siebbeles, L.D.A.; van Tendeloo, G.; Swart, I.; Hilhorst, J.; Petukhov, A.V.; Bals, S.; and Vanmaekelbergh, D. Long-range orientation and atomic attachment of nanocrystals in 2D honeycomb superlattices. *Science*, 344, 2014: 1377–1380.

[24] Cho, K.S.; Talapin, D.V.; Gaschler, W.; and Murray, C.B. Designing PbSe nanowires and nanorings through oriented attachment of nanoparticles. *J. Am. Chem. Soc*, 127, 2005: 7140–7147.

[25] Jia, G.; Sitt, A.; Hitin, G.B.; Hadar, I.; Bekenstein, Y.; Amit, Y.; Popov, I.; and Banin, U. Couples of colloidal semiconductor nanorods formed by self-limited assembly. *Nature Mater.*, 13, 2014: 301–307.

[26] Sadtler, B.; Demchenko, D.O.; Zheng, H.; Hughes, S.M.; Merkle, M.G.; Dahmen, U.; Wang, L.W.; and Alivisatos, A.P. Selective facet reactivity during cation exchange in cadmium sulfide nanorods. *J. Am. Chem. Soc*, 131, 2009: 5285–5293.

[27] Casavola, M.; van Huis, M.A.; Bals, S.; Lambert, K.; Hens, Z.; and Vanmaekelbergh, D. Anisotropic cation exchange in PbSe/CdSe core/shell nanocrystals of different geometry. *Chem. Mater.*, 24, 2011: 294–302.

[28] Lambert, K.; Geyter, B.D.; Moreels, I.; and Hens, Z. PbTe|CdTe core|shell particles by cation exchange, a HR-TEM study. *Chem. Mater.*, 21, 2009: 778–780.

[29] Zhang, Q.; Liu, S.J.; and Yu, S.H. Recent advances in oriented attachment growth and synthesis of functional materials: Concept, evidence, mechanism, and future. *J. Mater. Chem.*, 19, 2009: 191–207.

[30] Penn, R.L. and Banfield, J.F. Imperfect oriented attachment: dislocation generation in defect-free nanocrystals. *Science*, 281, 1998: 969–971.

[31] Schapotschnikow, P.; van Huis, M.A.; Zandbergen, H.W.; Vanmaekelbergh, D.; and Vlugt, T.J.H. Morphological transformations and fusion of PbSe nanocrystals studied using atomistic simulations. *Nano Lett.*, 10(10), 2010: 3966–3971.

[32] Zherebetskyy, D.; Scheele, M.; Zhang, Y.; Bronstein, N.; Thompson, C.; Britt, D.; Salmeron, M.; Alivisatos, P.; and Wang, L.W. Hydroxylation of the surface of PbS nanocrystals passivated with oleic acid. *Science*, 344, 2014: 1380–1384.

[33] Rivest, J.B. and Jain, P.K. Cation exchange on the nanoscale: An emerging technique for new material synthesis, device fabrication, and chemical sensing. *Chem. Soc. Rev.*, 42, 2013: 89–96.

[34] Beberwyck, B.J.; Surendranath, Y.; and Alivisatos, A.P. Cation exchange: A versatile tool for nanomaterials synthesis. *J. Phys. Chem. C*, 117, 2013: 19759–19770.

[35] Yalcin, A.O.; Fan, Z.; Goris, B.; Li, W.F.; Koster, R.S.; Fang, C.M.; van Blaaderen, A.; Casavola, M.; Tichelaar, F.D.; Bals, S.; Van Tendeloo, G.; Vlugt, T.J.H.; Vanmaekelbergh, D.; Zandbergen, H.W.; and van Huis, M.A. Atomic resolution monitoring of cation exchange in CdSe-PbSe hetero-nanocrystals during epitaxial solid-solid-vapor growth. *Nano Lett.*, 14(6), 2014: 3661–3667.

[36] Pietryga, J.M.; Werder, D.J.; Williams, D.J.; Casson, J.L.; Schaller, R.D.; Klimov, V.I.; and Hollingsworth, J.A. Utilizing the lability of lead selenide to produce heterostructured nanocrystals with bright, stable infrared emission. *J. Am. Chem. Soc*, 130, 2008: 4879–4885.

[37] Zhao, H.; Chaker, M.; Wu, N.; and Ma, D. Towards controlled synthesis and better understanding of highly luminescent PbS/CdS core/shell quantum dots. *J. Mater. Chem.*, 21, 2011: 8898–8904.

[38] Groeneveld, E.; Witteman, L.; Lefferts, M.; Ke, X.; Bals, S.; Van Tendeloo, G.; and de Mello Donega, C. Tailoring ZnSe–CdSe colloidal quantum dots via cation exchange: From core/shell to alloy nanocrystals. *ACS Nano.*, 7, 2013: 7913–7930.

[39] Robinson, R.D.; Sadtler, B.; Demchenko, D.O.; Erdonmez, C.K.; Wang, L.W.; and Alivisatos, A.P. Spontaneous superlattice formation in nanorods through partial cation exchange. *Science*, 317, 2007: 355–358.

[40] Miszta, K.; Dorfs, D.; Genovese, A.; Kim, M.R.; and Manna, L. Cation exchange reactions in colloidal branched nanocrystals. *ACS Nano.*, 5, 2011: 7176–7183.

[41] Jain, P.K.; Amirav, L.; Aloni, S.; and Alivisatos, A.P. Nanoheterostructure cation exchange: Anionic framework conservation. *J. Am. Chem. Soc*, 132, 2010: 9997–9999.

[42] Chan, E.M.; Marcus, M.A.; Fakra, S.; ElNaggar, M.; Mathies, R.A.; and Alivisatos, A.P. Millisecond kinetics of nanocrystal cation exchange using microfluidic X-ray absorption spectroscopy. *J. Phys. Chem. A*, 111, 2007: 12210–12215.

[43] Kisielowski, C.; Freitag, B.; Bischoff, M.; Van Lin, H.; Lazar, S.; Knippels, G.; Tiemeijer, P.; van der Stam, M.; von Harrach, S.; Stekelenburg, M.; Haider, M.; Uhlemann, S.; Müller, H.; Hartel, P.; Kabius, B.; Miller, D.; Petrov, I.; Olson, E.A.; Donchev, T.; Kenik, E.A.; Lupini, A.R.; Bentley, J.; Pennycook, S.J.; Anderson, I.M.; Minor, A.M.; Schmid, A.K.; Duden, T.; Radmilovic, V.; Ramasse, Q.M.; Watanabe, M.; Erni, R.; Stach, E.A.; Denes, P.; and Dahmen, U. Detection of single atoms and buried defects in three dimensions by aberration-corrected electron microscope with 0.5-Å information limit. *Microsc. Microanal.*, 14, 2008: 469–477.

[44] van Huis, M.A.; Young, N.P.; Pandraud, G.; Creemer, J.F.; Vanmaekelbergh, D.; Kirkland, A.I.; and Zandbergen, H.W. Atomic imaging of phase transitions and morphology transformations in nanocrystals. *Adv. Mater.*, 21, 2009: 4992–4995.

[45] Martin, R.M. *Electronic structure: basic theory and practical methods.* Cambridge University Press, Cambridge, 1st edition, 2004.

[46] Hohenberg, P. and Kohn, W. Inhomogeneous electron gas. *Phys. Rev.*, 136, 1964: B864.

[47] Kohn, W. and Sham, L.J. Self-consistent equations including exchange and correlation effects. *Phys. Rev.*, 140, 1965: A1133.

[48] The nobel prize in chemistry 1998. `http://www.nobelprize.org/nobel_prizes/chemistry/laureates/1998/`. Accessed: 2015-09-06.

[49] Bartolotti, L.J. and Flurchick, K. An introduction to density functional theory. *Rev. Comp. Chem.*, 7, 1996: 187–260.

[50] Oganov, A.R.; Chen, J.; Gatti, C.; Ma, Y.; Ma, Y.; Glass, C.W.; Liu, Z.; Yu, T.; Kurakevych, O.O.; and Solozhenko, V.L. Ionic high-pressure form of elemental boron. *Nature*, 457, 2009: 863–867.

[51] Zhang, W.; Oganov, A.R.; Goncharov, A.F.; Zhu, Q.; Boulfelfel, S.E.; Lyakhov, A.O.; Stavrou, E.; Somayazulu, M.; Prakapenka, V.B.; and Konôpková, Z. Unexpected stable stoichiometries of sodium chlorides. *Science*, 342, 2013: 1502–1505.

[52] Parr, R.G.; Ayers, P.W.; and Nalewajski, R.F. What is an atom in a molecule? *J. Phys. Chem. A*, 109, 2005: 3957–3959.

[53] Matta, C.F. and Bader, R.F. An experimentalist's reply to what is an atom in a molecule? *J. Phys. Chem. A*, 110, 2006: 6365–6371.

[54] Fonseca Guerra, C.; Handgraaf, J.W.; Baerends, E.J.; and Bickelhaupt, F.M. Voronoi deformation density (VDD) charges: Assessment of the Mulliken, Bader, Hirshfeld, Weinhold, and VDD methods for charge analysis. *J. Comput. Chem.*, 25, 2004: 189–210.

[55] Bader, R.F. and Matta, C.F. Atomic charges are measurable quantum expectation values: a rebuttal of criticisms of QTAIM charges. *J. Phys. Chem. A*, 108, 2004: 8385–8394.

[56] Bader, R.F.W. *Atoms in Molecules: A Quantum Theory.* Oxford University Press, New York, 1st edition, 1990.

[57] Agrawal, R.; Paci, J.T.; and Espinosa, H.D. Large-scale density functional theory investigation of failure modes in ZnO nanowires. *Nano Lett.*, 10(9), 2010: 3432–3438.

[58] Greenman, L.; Whitley, H.D.; and Whaley, K.B. Large-scale atomistic density functional theory calculations of phosphorus-doped silicon quantum bits. *Phys. Rev. B*, 88, 2013: 165102.

[59] Kresse, G. and Hafner, J. Ab initio molecular dynamics for liquid metals. *Phys. Rev. B*, 47, 1993: 558.

[60] Krack, M. and Parrinello, M. All-electron ab-initio molecular dynamics. *Phys. Chem. Chem. Phys.*, 2, 2000: 2105–2112.

[61] Frenkel, D. and Smit, B. *Understanding Molecular Simulation.* Academic Press, New York, 2nd edition, 2002.

[62] Allen, M.P. and Tildesley, D.J. *Computer Simulation of Liquids.* Oxford University Press, Oxford, 1st edition, 1989.

[63] Martyna, G.J.; Tobias, D.J.; and Klein, M.L. Constant pressure molecular dynamics algorithms. *J. Chem. Phys.*, 101, 1994: 4177–4189.

[64] Rapaport, D.C. *The art of Molecular Dynamics Simulation.* Cambridge University Press, Cambridge, 2nd edition, 2004.

[65] Tuckerman, M. *Statistical Mechanics: Theory and Molecular Simulation.* Oxford University Press, Oxford, 2010.

[66] Vlugt, T.J.; Van der Eerden, J.; Dijkstra, M.; Smit, B.; and Frenkel, D. Introduction to molecular simulation and statistical thermodynamics. 2008. Available from: `http://homepage.tudelft.nl/v9k6y/imsst/index.html`.

[67] Zhao, G.; Perilla, J.R.; Yufenyuy, E.L.; Meng, X.; Chen, B.; Ning, J.; Ahn, J.; Gronenborn, A.M.; Schulten, K.; Aiken, C.; and Zhang, P. Mature hiv-1 capsid structure by cryo-electron microscopy and all-atom molecular dynamics. *Nature*, 497, 2013: 643–646.

[68] Fan, Z.; Yalcin, A.O.; Tichelaar, F.D.; Zandbergen, H.W.; Talgorn, E.; Houtepen, A.J.; Vlugt, T.J.H.; and van Huis, M.A. From sphere to multipod: Thermally induced transitions of CdSe nanocrystals studied by molecular dynamics simulations. *J. Am. Chem. Soc*, 135, 2013: 5869–5876.

[69] Hu, M.; Poulikakos, D.; Grigoropoulos, C.P.; and Pan, H. Recrystallization of picosecond laser-melted ZnO nanoparticles in a liquid: A molecular dynamics study. *J. Chem. Phys.*, 132, 2010: 164504.

[70] PEDONE, A.; MALAVASI, G.; MENZIANI, M.C.; CORMACK, A.N.; and SEGRE, U. A new self-consistent empirical interatomic potential model for oxides, silicates, and silica-based glasses. *J. Phys. Chem. B*, 110, 2006: 11780–11795.

[71] ÖZGÜR, U.; ALIVOV, Y.I.; LIU, C.; TEKE, A.; RESHCHIKOV, M.A.; DOĞAN, S.; AVRUTIN, V.; CHO, S.J.; and MORKOÇ, H. A comprehensive review of ZnO materials and devices. *J. Appl. Phys.*, 98(4), 2005:041301.

[72] DONG, Z.; ZHURAVLEV, K.K.; MORIN, S.A.; LI, L.; JIN, S.; and SONG, Y. Pressure-induced structural transformations of ZnO nanowires probed by X-ray diffraction. *J. Phys. Chem. C*, 116, 2012: 2102–2107.

[73] JIANG, J.; OLSEN, J.; GERWARD, L.; FROST, D.; RUBIE, D.; and PEYRONNEAU, J. Structural stability in nanocrystalline ZnO. *Europhys. Lett.*, 50, 2000: 48.

[74] WANG, J.; KULKARNI, A.J.; SARASAMAK, K.; LIMPIJUMNONG, S.; KE, F.J.; and ZHOU, M. Molecular dynamics and density functional studies of a body-centered-tetragonal polymorph of ZnO. *Phys. Rev. B*, 76, 2007: 172103.

[75] AGRAWAL, R.; PENG, B.; and ESPINOSA, H.D. Experimental-computational investigation of ZnO nanowires strength and fracture. *Nano Lett.*, 9(12), 2009: 4177–4183.

[76] DEMIROGLU, I. and BROMLEY, S.T. Nanofilm versus bulk polymorphism in wurtzite materials. *Phys. Rev. Lett.*, 110, 2013: 245501.

[77] HE, M.R.; YU, R.; and ZHU, J. Reversible wurtzite-tetragonal reconstruction in ZnO($10\bar{1}0$) surfaces. *Angew. Chem.*, 124(31), 2012: 7864–7867.

[78] MORGAN, B.J. Preferential stability of the d-bct phase in ZnO thin films. *Phys. Rev. B*, 80, 2009: 174105.

[79] CARRASCO, J.; ILLAS, F.; and BROMLEY, S.T. Ultralow-density nanocage-based metal-oxide polymorphs. *Phys. Rev. Lett.*, 99, 2007: 235502.

[80] MORGAN, B.J. First-principles study of epitaxial strain as a method of b4→bct stabilization in ZnO, ZnS, and CdS. *Phys. Rev. B*, 82, 2010: 153408.

[81] Binks, D.J. and Grimes, R.W. Incorporation of monovalent ions in ZnO and their influence on varistor degradation. *J. Am. Ceram. Soc.*, 76(9), 1993: 2370–2372.

[82] Wang, S.; Fan, Z.; Koster, R.S.; Fang, C.; van Huis, M.A.; Yalcin, A.O.; Tichelaar, F.D.; Zandbergen, H.W.; and Vlugt, T.J.H. New ab initio based pair potential for accurate simulation of phase transitions in ZnO. *J. Phys. Chem. C*, 118(20), 2014: 11050–11061.

[83] Gale, J.D. Empirical potential derivation for ionic materials. *Philos. Mag. B*, 73(1), 1996: 3–19.

[84] Voter, A.F. Interatomic potentials for atomistic simulations. *MRS Bulletin*, 21, 1996: 17–19.

[85] Stoneham, M.; Harding, J.; and Harker, T. The shell model and interatomic potentials for ceramics. *MRS Bulletin*, 21, 1996: 29–35.

[86] Brenner, D.W. Chemical dynamics and bond-order potentials. *MRS Bulletin*, 21, 1996: 36–41.

[87] Foiles, S.M. Embedded-atom and related methods for modeling metallic systems. *MRS Bulletin*, 21, 1996: 24–28.

[88] Raymand, D.; van Duin, A.C.T.; Baudin, M.; and Hermansson, K. A reactive force field (ReaxFF) for zinc oxide. *Surf. Sci.*, 602(5), 2008: 1020–1031.

[89] Larsson, H.R.; van Duin, A.C.T.; and Hartke, B. Global optimization of parameters in the reactive force field ReaxFF for SiOH. *J. Comput. Chem.*, 34(25), 2013: 2178–2189.

[90] Iype, E.; Hütter, M.; Jansen, A.P.J.; Nedea, S.V.; and Rindt, C.C.M. Parameterization of a reactive force field using a Monte Carlo algorithm. *J. Comput. Chem.*, 34(13), 2013: 1143–1154.

[91] Lewis, G.V. and Catlow, C.R.A. Potential models for ionic oxides. *J. Phys. C: Solid State Phys.*, 18, 1985: 1149.

[92] Rabani, E. An interatomic pair potential for cadmium selenide. *J. Comput. Phys.*, 116(1), 2002: 258–262.

[93] GRÜNWALD, M.; RABANI, E.; and DELLAGO, C. Mechanisms of the wurtzite to rocksalt transformation in CdSe nanocrystals. *Phys. Rev. Lett.*, 96, 2006: 255701.

[94] GRÜNWALD, M.; ZAYAK, A.; NEATON, J.B.; GEISSLER, P.L.; and RABANI, E. Transferable pair potentials for CdS and ZnS crystals. *J. Comput. Phys.*, 136(23), 2012: 234111.

[95] FAN, Z.; KOSTER, R.S.; WANG, S.; FANG, C.; YALCIN, A.O.; TICHELAAR, F.D.; ZANDBERGEN, H.W.; VAN HUIS, M.A.; and VLUGT, T.J.H. A transferable force field for CdS-CdSe-PbS-PbSe solid systems. *J. Chem. Phys.*, 141, 2014: 244503.

[96] VEGA, C. Water: one molecule, two surfaces, one mistake. *Mol. Phys.*, 113, 2015: 1–19.

[97] NORD, J.; ALBE, K.; ERHART, P.; and NORDLUND, K. Modelling of compound semiconductors: analytical bond-order potential for gallium, nitrogen and gallium nitride. *J. Phys.: Condens. Matter*, 15, 2003: 5649.

[98] XIAO, H.; JIANG, X.; DUAN, G.; GAO, F.; ZU, X.; and WEBER, W. First-principles calculations of pressure-induced phase transformation in AlN and GaN. *Comput. Mater. Sci.*, 48, 2010: 768–772.

[99] ZHOU, X.; AUBRY, S.; JONES, R.; GREENSTEIN, A.; and SCHELLING, P. Towards more accurate molecular dynamics calculation of thermal conductivity: Case study of GaN bulk crystals. *Phys. Rev. B*, 79, 2009: 115201.

[100] NORD, J.; NORDLUND, K.; and KEINONEN, J. Molecular dynamics study of damage accumulation in GaN during ion beam irradiation. *Phys. Rev. B*, 68, 2003: 184104.

[101] HARAFUJI, K.; TSUCHIYA, T.; and KAWAMURA, K. Molecular dynamics simulation for evaluating melting point of wurtzite-type GaN crystal. *J. Appl. Phys.*, 96, 2004: 2501–2512.

[102] SBORGI, L.; VERMA, A.; PIANA, S.; LINDORFF-LARSEN, K.; CERMINARA, M.; SANTIVERI, C.M.; SHAW, D.E.; DE ALBA, E.; and MUNOZ, V. Interaction networks in protein folding via atomic-resolution experiments and long-timescale molecular dynamics simulations. *J. Am. Chem. Soc*, 2015.

[103] Klingshirn, C. ZnO: From basics towards applications. *Phys. Status Solidi B*, 244(9), 2007: 3027–3073.

[104] Baruah, S. and Dutta, J. Hydrothermal growth of ZnO nanostructures. *Sci. Technol. Adv. Mater.*, 10, 2009: 013001.

[105] Heo, Y.W.; Norton, D.P.; Tien, L.C.; Kwon, Y.; Kang, B.S.; Ren, F.; Pearton, S.J.; and LaRoche, J.R. ZnO nanowire growth and devices. *Mat. Sci. Eng. R*, 47, 2004: 1–47.

[106] Xu, S. and Wang, Z.L. One-dimensional ZnO nanostructures: Solution growth and functional properties. *Nano Res.*, 4, 2011: 1013–1098.

[107] Lu, J.G.; Chang, P.; and Fan, Z. Quasi-one-dimensional metal oxide materials-synthesis, properties and applications. *Mat. Sci. Eng. R*, 52, 2006: 49–91.

[108] Sekiguchi, T.; Miyashita, S.; Obara, K.; Shishido, T.; and Sakagami, N. Hydrothermal growth of ZnO single crystals and their optical characterization. *J. Cryst. Growth*, 214-215(0), 2000: 72–76.

[109] Matsumoto, K. and Noda, K. Crystal growth of ZnO by chemical transport using $HgCl_2$ as a transport agent. *J. Cryst. Growth*, 102(1-2), 1990: 137–140.

[110] Hachigo, A.; Nakahata, H.; Higaki, K.; Fujii, S.; and Shikata, S. Heteroepitaxial growth of ZnO films on diamond (111) plane by magnetron sputtering. *Appl. Phys. Lett.*, 65(20), 1994: 2556–2558.

[111] Jaffe, J.E.; Snyder, J.A.; Lin, Z.; and Hess, A.C. LDA and GGA calculations for high-pressure phase transitions in ZnO and MgO. *Phys. Rev. B*, 62, 2000: 1660–1665.

[112] M., A.A.A.B.; Ueta, A.; Avramescu, A.; Kumano, H.; Suemune, I.; Ok, Y.W.; and Seong, T.Y. Growth and characterization of hypothetical zinc-blende ZnO films on GaAs(001) substrates with ZnS buffer layers. *Appl. Phys. Lett.*, 76(5), 2000: 550–552.

[113] Kim, S.K.; Jeong, S.Y.; and Cho, C.R. Structural reconstruction of hexagonal to cubic ZnO films on Pt/Ti/SiO_2/Si substrate by annealing. *Appl. Phys. Lett.*, 82(4), 2003: 562–564.

[114] BATES, C.H.; WHITE, W.B.; and ROY, R. New high-pressure polymorph of zinc oxide. *Science*, 137(3534), 1962: 993.

[115] GERWARD, L. and STAUN OLSEN, J. The High-Pressure Phase of Zincite. *J. Synchrotron Rad.*, 2(5), 1995: 233–235.

[116] DESGRENIERS, S. High-density phases of ZnO: Structural and compressive parameters. *Phys. Rev. B*, 58, 1998: 14102–14105.

[117] KARZEL, H.; POTZEL, W.; KÖFFERLEIN, M.; SCHIESSL, W.; STEINER, M.; HILLER, U.; KALVIUS, G.M.; MITCHELL, D.W.; DAS, T.P.; and BLAHA, P. ET AL. Lattice dynamics and hyperfine interactions in ZnO and ZnSe at high external pressures. *Phys. Rev. B*, 53, 1996: 11425–11438.

[118] MEULENKAMP, E.A. Synthesis and growth of ZnO nanoparticles. *J. Phys. Chem. B*, 102(29), 1998: 5566–5572.

[119] PARK, W.I.; KIM, D.H.; JUNG, S.W.; and YI, G.C. Metalorganic vapor-phase epitaxial growth of vertically well-aligned ZnO nanorods. *Appl. Phys. Lett.*, 80(22), 2002: 4232–4234.

[120] HUANG, M.H.; MAO, S.; FEICK, H.; YAN, H.; WU, Y.; KIND, H.; WEBER, E.; RUSSO, R.; and YANG, P. Room-temperature ultraviolet nanowire nanolasers. *Science*, 292(5523), 2001: 1897–1899.

[121] PAN, Z.W.; DAI, Z.R.; and WANG, Z.L. Nanobelts of semiconducting oxides. *Science*, 291(5510), 2001: 1947–1949.

[122] GAO, P.X.; DING, Y.; MAI, W.; HUGHES, W.L.; LAO, C.; and WANG, Z.L. Conversion of zinc oxide nanobelts into superlattice-structured nanohelices. *Science*, 309(5741), 2005: 1700–1704.

[123] SUN, Y.; FUGE, G.M.; FOX, N.A.; RILEY, D.J.; and ASHFOLD, M.N.R. Synthesis of aligned arrays of ultrathin ZnO nanotubes on a Si wafer coated with a thin ZnO film. *Adv. Mater.*, 17(20), 2005: 2477–2481.

[124] JUNG, S.; CHO, W.; LEE, H.J.; and OH, M. Self-template-directed formation of coordination-polymer hexagonal tubes and rings, and their calcination to ZnO rings. *Angew. Chem. Int. Edit.*, 48(8), 2009: 1459–1462.

[125] Yu, W.D.; Li, X.M.; and Gao, X.D. Self-catalytic synthesis and photoluminescence of ZnO nanostructures on ZnO nanocrystal substrates. *Appl. Phys. Lett.*, 84(14), 2004: 2658–2660.

[126] Djurišić, A.B.; Leung, Y.H.; Choy, W.C.H.; Cheah, K.W.; and Chan, W.K. Visible photoluminescence in ZnO tetrapod and multipod structures. *Appl. Phys. Lett.*, 84(14), 2004: 2635–2637.

[127] Zhang, H.; Yang, D.; Ji, Y.; Ma, X.; Xu, J.; and Que, D. Low temperature synthesis of flowerlike ZnO nanostructures by cetyltrimethylammonium bromide-assisted hydrothermal process. *J. Phys. Chem. B*, 108(13), 2004: 3955–3958.

[128] Wang, Z.L. and Song, J. Piezoelectric nanogenerators based on zinc oxide nanowire arrays. *Science*, 312(5771), 2006: 242–246.

[129] Sarasamak, K.; Limpijumnong, S.; and Lambrecht, W.R.L. Pressure-dependent elastic constants and sound velocities of wurtzite SiC, GaN, InN, ZnO, and CdSe, and their relation to the high-pressure phase transition: A first-principles study. *Phys. Rev. B*, 82, 2010: 035201.

[130] Wu, X.; Vanderbilt, D.; and Hamann, D.R. Systematic treatment of displacements, strains, and electric fields in density-functional perturbation theory. *Phys. Rev. B*, 72, 2005: 035105.

[131] Schröer, P.; Krüger, P.; and Pollmann, J. First-principles calculation of the electronic structure of the wurtzite semiconductors ZnO and ZnS. *Phys. Rev. B*, 47, 1993: 6971–6980.

[132] Erhart, P.; Albe, K.; and Klein, A. First-principles study of intrinsic point defects in ZnO: Role of band structure, volume relaxation, and finite-size effects. *Phys. Rev. B*, 73, 2006: 205203.

[133] Seko, A.; Oba, F.; Kuwabara, A.; and Tanaka, I. Pressure-induced phase transition in ZnO and ZnO-MgO pseudobinary system: A first-principles lattice dynamics study. *Phys. Rev. B*, 72, 2005: 024107.

[134] Serrano, J.; Manjón, F.J.; Romero, A.H.; Ivanov, A.; Cardona, M.; Lauck, R.; Bosak, A.; and Krisch, M. Phonon dispersion relations of zinc oxide: Inelastic neutron scattering and calculations. *Phys. Rev. B*, 81, 2010: 174304.

[135] SERRANO, J.; ROMERO, A.H.; MANJÓN, F.J.; LAUCK, R.; CARDONA, M.; and RUBIO, A. Pressure dependence of the lattice dynamics of ZnO: An *Ab Initio* approach. *Phys. Rev. B*, 69, 2004: 094306.

[136] CAI, J. and CHEN, N. First-principles study of the wurtzite-to-rocksalt phase transition in zinc oxide. *J. Phys.: Condens. Matter*, 19, 2007: 266207.

[137] ZWIJNENBURG, M.A.; ILLAS, F.; and BROMLEY, S.T. Apparent scarcity of low-density polymorphs of inorganic solids. *Phys. Rev. Lett.*, 104, 2010: 175503.

[138] SCHLEIFE, A.; FUCHS, F.; FURTHMÜLLER, J.; and BECHSTEDT, F. First-principles study of ground- and excited-state properties of MgO, ZnO, and CdO polymorphs. *Phys. Rev. B*, 73, 2006: 245212.

[139] LIMPIJUMNONG, S. and JUNGTHAWAN, S. First-principles study of the wurtzite-to-rocksalt homogeneous transformation in ZnO: A case of a low-transformation barrier. *Phys. Rev. B*, 70, 2004: 054104.

[140] LI, C.; GUO, W.; KONG, Y.; and GAO, H. First-principles study of the dependence of ground-state structural properties on the dimensionality and size of ZnO nanostructures. *Phys. Rev. B*, 76, 2007: 035322.

[141] TOPSAKAL, M.; CAHANGIROV, S.; BEKAROGLU, E.; and CIRACI, S. First-principles study of zinc oxide honeycomb structures. *Phys. Rev. B*, 80, 2009: 235119.

[142] LI, Z.; XU, Y.; GAO, G.; CUI, T.; and MA, Y. Tetragonal high-pressure phase of ZnO predicted from first principles. *Phys. Rev. B*, 79, 2009: 193201.

[143] BOULFELFEL, S.E. and LEONI, S. Competing intermediates in the pressure-induced wurtzite to rocksalt phase transition in ZnO. *Phys. Rev. B*, 78, 2008: 125204.

[144] KUBO, M.; OUMI, Y.; TAKABA, H.; CHATTERJEE, A.; MIYAMOTO, A.; KAWASAKI, M.; YOSHIMOTO, M.; and KOINUMA, H. Homoepitaxial growth mechanism of ZnO(0001): Molecular-dynamics simulations. *Phys. Rev. B*, 61, 2000: 16187–16192.

[145] KULKARNI, A.J.; ZHOU, M.; SARASAMAK, K.; and LIMPIJUMNONG, S. Novel phase transformation in ZnO nanowires under tensile loading. *Phys. Rev. Lett.*, 97, 2006: 105502.

[146] Combe, N.; Chassaing, P.M.; and Demangeot, F. Surface effects in zinc oxide nanoparticles. *Phys. Rev. B*, 79, 2009: 045408.

[147] Raymand, D.; van Duin, A.C.T.; Spångberg, D.; Goddard III, W.A.; and Hermansson, K. Water adsorption on stepped ZnO surfaces from MD simulation. *Surf. Sci.*, 604, 2010: 741 – 752.

[148] Raymand, D.; Jacobsson, T.J.; Hermansson, K.; and Edvinsson, T. Investigation of vibrational modes and phonon density of states in ZnO quantum dots. *J. Phys. Chem. C*, 116(12), 2012: 6893–6901.

[149] Momeni, K.; Odegard, G.M.; and Yassar, R.S. Finite size effect on the piezoelectric properties of ZnO nanobelts: A molecular dynamics approach. *Acta Mater.*, 60(13-14), 2012: 5117–5124.

[150] Kulkarni, A.J.; Zhou, M.; and Ke, F.J. Orientation and size dependence of the elastic properties of zinc oxide nanobelts. *Nanotechnology*, 16, 2005: 2749.

[151] Dai, L.; Cheong, W.C.D.; Sow, C.H.; Lim, C.T.; and Tan, V.B.C. Molecular dynamics simulation of ZnO nanowires: Size effects, defects, and super ductility. *Langmuir*, 26(2), 2010: 1165–1171.

[152] Dong, X.; Liu, F.; Xie, Y.; Shi, W.; Ye, X.; and Jiang, J.Z. Pressure-induced structural transition of ZnO nanocrystals studied with molecular dynamics. *Comput. Mater. Sci.*, 65(0), 2012: 450–455.

[153] Whitmore, L.; Sokol, A.A.; and Catlow, C.R.A. Surface structure of zinc oxide (1010), using an atomistic, semi-infinite treatment. *Surf. Sci.*, 498, 2002: 135–146.

[154] Al-Sunaidi, A.A.; Sokol, A.A.; Catlow, C.R.A.; and Woodley, S.M. Structures of zinc oxide nanoclusters: as found by revolutionary algorithm techniques. *J. Phys. Chem. C*, 112, 2008: 18860–18875.

[155] Catlow, C.R.A.; French, S.A.; Sokol, A.A.; Al-Sunaidi, A.A.; and Woodley, S.M. Zinc oxide: A case study in contemporary computational solid state chemistry. *J. Comput. Chem.*, 29(13), 2008: 2234–2249.

[156] Agrawal, R.; Peng, B.; Gdoutos, E.E.; and Espinosa, H.D. Elasticity size effects in ZnO nanowires-a combined experimental-computational approach. *Nano Lett.*, 8(11), 2008: 3668–3674.

[157] ERHART, P.; JUSLIN, N.; GOY, O.; NORDLUND, K.; MÜLLER, R.; and ALBE, K. Analytic bond-order potential for atomistic simulations of zinc oxide. *J. Phys.: Condens. Matter*, 18, 2006: 6585.

[158] CHEN, N.X. Modified Möbius inverse formula and its applications in physics. *Phys. Rev. Lett.*, 64, 1990: 1193–1195.

[159] YUAN, X.; CHEN, N.; SHEN, J.; and HU, W. Embedded-atom-method interatomic potentials from lattice inversion. *J. Phys.: Condens. Matter*, 22, 2010: 375503.

[160] KANG, Y. and CHEN, N. Site preference and vibrational properties of sccu_xal_12-x. *J. Alloys Compd.*, 349, 2003: 41–48.

[161] ZHANG, S. and CHEN, N. *Ab Initio* interionic potentials for NaCl by multiple lattice inversion. *Phys. Rev. B*, 66, 2002: 064106.

[162] ZHANG, S. and CHEN, N. Lattice inversion for interatomic potentials in AlN, GaN and InN. *Chem. Phys.*, 309, 2005: 309–321.

[163] TSUNEYUKI, S.; TSUKADA, M.; AOKI, H.; and MATSUI, Y. First-principles interatomic potential of silica applied to molecular dynamics. *Phys. Rev. Lett.*, 61, 1988: 869–872.

[164] KRESSE, G. and FURTHMÜLLER, J. Efficiency of ab-initio yotal energy calculations for metals and semiconductors using a plane-wave basis set. *Comput. Mater. Sci.*, 6(1), 1996: 15–50.

[165] BLÖCHL, P.E. Projector augmented-wave method. *Phys. Rev. B*, 50, 1994: 17953–17979.

[166] PERDEW, J.P.; BURKE, K.; and ERNZERHOF, M. Generalized gradient approximation made simple. *Phys. Rev. Lett.*, 77, 1996: 3865–3868.

[167] MONKHORST, H.J. and PACK, J.D. Special points for brillouin-zone integrations. *Phys. Rev. B*, 13, 1976: 5188–5192.

[168] TANG, W.; SANVILLE, E.; and HENKELMAN, G. A grid-based bader analysis algorithm without lattice bias. *J. Phys.: Condens. Matter*, 21, 2009: 08420.

[169] Sanville, E.; Kenny, S.D.; Smith, R.; and Henkelman, G. Improved grid-based algorithm for Bader charge allocation. *J. Comput. Chem.*, 28(5), 2007: 899–908.

[170] Henkelman, G.; Arnaldsson, A.; and Jónsson, H. A fast and robust algorithm for Bader decomposition of charge density. *Comput. Mater. Sci.*, 36(3), 2006: 354–360.

[171] Wilson, M. and Madden, P.A. Transformations between tetrahedrally and octahedrally coordinated crystals. *J. Phys.: Condens. Matter*, 14, 2002: 4629.

[172] Born, M. and E., M.J. Zur gittertheorie der ionenkristalle. *Z. Phys.*, 75, 1932: 1–18.

[173] Morse, P.M. Diatomic molecules according to the wave mechanics. II. vibrational levels. *Phys. Rev.*, 34, 1929: 57–64.

[174] Ewald, P.P. Die berechnung optischer und elektrostatischer gitterpotentiale. *Ann. Phys*, 369(3), 1921: 253–287.

[175] Albertsson, J.; Abrahams, S.C.; and Kvick, A. Atomic displacement, anharmonic thermal vibration, expansivity and pyroelectric coefficient thermal dependences in ZnO. *Acta Cryst. B*, 45(1), 1989: 34–40.

[176] Kobiakov, I.B. Elastic, piezoelectric and dielectric properties of ZnO and CdS single crystals in a wide range of temperatures. *Solid State Commun.*, 35(3), 1980: 305–310.

[177] Gale, J.D. and Rohl, A.L. The general utility lattice program (gulp). *Mol. Simul.*, 29(5), 2003: 291–341.

[178] Plimpton, S. Fast parallel algorithms for short-range molecular dynamics. *J. Chem. Phys.*, 117(1), 1995: 1–19.

[179] Steinle-Neumann, G.; Stixrude, L.; and Cohen, R.E. First-principles elastic constants for the hcp transition metals Fe, Co, and Re at high pressure. *Phys. Rev. B*, 60, 1999: 791–799.

[180] Iwanaga, H.; Kunishige, A.; and Takeuchi, S. Anisotropic thermal expansion in wurtzite-type crystals. *J. Mater. Sci.*, 35, 2000: 2451–2454.

[181] LAMOREAUX, R.H.; HILDENBRAND, D.L.; and BREWER, L. High-temperature vaporization behavior of oxides II. oxides of Be, Mg, Ca, Sr, Ba, B, Al, Ga, In, Tl, Si, Ge, Sn, Pb, Zn, Cd, and Hg. *J. Phys. Chem. Ref. Data*, 16(3), 1987: 419–443.

[182] MORRIS, J.R.; WANG, C.Z.; HO, K.M.; and CHAN, C.T. Melting line of aluminum from simulations of coexisting phases. *Phys. Rev. B*, 49, 1994: 3109–3115.

[183] STARIKOV, S.V. and STEGAILOV, V.V. Atomistic simulation of the premelting of iron and aluminum: Implications for high-pressure melting-curve measurements. *Phys. Rev. B*, 80, 2009: 220104.

[184] ZAHN, D.; GRIN, Y.; and LEONI, S. Mechanism of the pressure-induced wurtzite to rocksalt transition of CdSe. *Phys. Rev. B*, 72, 2005: 064110.

[185] KNUDSON, M.D.; GUPTA, Y.M.; and KUNZ, A.B. Transformation mechanism for the pressure-induced phase transition in shocked CdS. *Phys. Rev. B*, 59, 1999: 11704–11715.

[186] LIMPIJUMNONG, S. and LAMBRECHT, W.R.L. Homogeneous strain deformation path for the wurtzite to rocksalt high-pressure phase transition in GaN. *Phys. Rev. Lett.*, 86, 2001: 91–94.

[187] TUSCHE, C.; MEYERHEIM, H.L.; and KIRSCHNER, J. Observation of depolarized ZnO(0001) monolayers: Formation of unreconstructed planar sheets. *Phys. Rev. Lett.*, 99, 2007: 026102.

[188] MARANA, N.L.; LONGO, V.M.; LONGO, E.; MARTINS, J.B.L.; and SAMBRANO, J.R. Electronic and structural properties of the (1010) and (1120) ZnO surfaces. *J. Phys. Chem. A*, 112(38), 2008: 8958–8963.

[189] SPENCER, M.J.S.; WONG, K.W.J.; and YAROVSKY, I. Density functional theory modelling of ZnO($10\bar{1}0$) and ZnO($2\bar{1}\bar{1}0$) surfaces: Structure, properties and adsorption of N_2O. *Mater. Chem. Phys.*, 119(3), 2010: 505–514.

[190] WANDER, A.; SCHEDIN, F.; STEADMAN, P.; NORRIS, A.; MCGRATH, R.; TURNER, T.S.; THORNTON, G.; and HARRISON, N.M. Stability of polar oxide surfaces. *Phys. Rev. Lett.*, 86, 2001: 3811–3814.

[191] Lauritsen, J.V.; Porsgaard, S.; Rasmussen, M.K.; Jensen, M.C.R.; Bechstein, R.; Meinander, K.; Clausen, B.S.; Helveg, S.; Wahl, R.; Kresse, G.; and Besenbacher, F. Stabilization principles for polar surfaces of ZnO. *ACS Nano*, 5(7), 2011: 5987–5994.

[192] Dulub, O.; Diebold, U.; and Kresse, G. Novel stabilization mechanism on polar surfaces: ZnO(0001)-Zn. *Phys. Rev. Lett.*, 90, 2003: 016102.

[193] Kresse, G.; Dulub, O.; and Diebold, U. Competing stabilization mechanism for the polar ZnO(0001)-Zn surface. *Phys. Rev. B*, 68, 2003: 245409.

[194] Kunat, M.; Girol, S.G.; Becker, T.; Burghaus, U.; and Wöll, C. Stability of the polar surfaces of ZnO: A reinvestigation using He-atom scattering. *Phys. Rev. B*, 66, 2002: 081402.

[195] Hamad, S.; Cristol, S.; and Catlow, C.R.A. Surface structures and crystal morphology of ZnS:a computational study. *J. Phys. Chem. B*, 106(42), 2002: 11002–11008.

[196] Nyberg, M.; Nygren, M.A.; Pettersson, L.G.M.; Gay, D.H.; and Rohl, A.L. Hydrogen dissociation on reconstructed ZnO surfaces. *J. Phys. Chem.*, 100(21), 1996: 9054–9063.

[197] Peng, X.; Manna, L.; Yang, W.; Wickham, J.; Scher, E.; Kadavanich, A.; and Alivisatos, A.P. Shape control of CdSe nanocrystals. *Nature*, 404, 2000: 59–61.

[198] Peng, Z.A. and Peng, X. Formation of high-quality cdte, CdSe, and CdS nanocrystals using CdO as precursor. *J. Am. Chem. Soc*, 123, 2001: 183–184.

[199] Schaller, R.D. and Klimov, V.I. High efficiency carrier multiplication in PbSe nanocrystals: Implications for solar energy conversion. *Phys. Rev. Lett.*, 92, 2004: 186601.

[200] Ellingson, R.J.; Beard, M.C.; Johnson, J.C.; Yu, P.; Micic, O.I.; Nozik, A.J.; Shabaev, A.; and Efros, A.L. Highly efficient multiple exciton generation in colloidal PbSe and PbS quantum dots. *Nano Lett.*, 5(5), 2005: 865–871.

[201] Sadao, A. *Properties of Group-IV, III-V and II-VI Semiconductors.* Wiley, New York, 1st edition, 2005.

[202] ALIVISATOS, A.P. Semiconductor clusters, nanocrystals, and quantum dots. *Science*, 271, 1996: 933–937.

[203] MADELUNG, O.; RÖSSLER, U.; and SCHULZ, M. *Landolt-Börnstein III/41C: Non-Tetrahedrally Bonded Elements and Binary Compounds I.* Springer-Verlag, Berlin, Germany, 1st edition, 1998.

[204] FARDY, M.; HOCHBAUM, A.I.; GOLDBERGER, J.; ZHANG, M.M.; and YANG, P. Synthesis and thermoelectrical characterization of lead chalcogenide nanowires. *Adv. Mater.*, 19, 2007: 3047–3051.

[205] WANG, R.Y.; FESER, J.P.; LEE, J.S.; TALAPIN, D.V.; SEGALMAN, R.; and MAJUMDAR, A. Enhanced thermopower in PbSe nanocrystal quantum dot superlattices. *Nano Lett.*, 8(8), 2008: 2283–2288.

[206] YONG, K.T.; SAHOO, Y.; SWIHART, M.T.; and PRASAD, P.N. Shape control of CdS nanocrystals in one-pot synthesis. *J. Phys. Chem. C*, 111(6), 2007: 2447–2458.

[207] RICE, K.P.; SAUNDERS, A.E.; and STOYKOVICH, M.P. Seed-mediated growth of shape-controlled wurtzite CdSe nanocrystals: Platelets, cubes, and rods. *J. Am. Chem. Soc*, 135(17), 2013: 6669–6676.

[208] YU, W.W.; WANG, Y.A.; and PENG, X. Formation and stability of size-, shape-, and structure-controlled CdTe nanocrystals: A ligand effects on monomers and nanocrystals. *Chem. Mater.*, 15(22), 2003: 4300–4308.

[209] ZHOU, G.; LU, M.; XIU, Z.; WANG, S.; ZHANG, H.; ZHOU, Y.; and WANG, S. Controlled synthesis of high-quality PbS star-shaped dendrites, multipods, truncated nanocubes, and nanocubes and their shape evolution process. *J. Phys. Chem. B*, 110(13), 2006: 6543–6548.

[210] LIFSHITZ, E.; BASHOUTI, M.; KLOPER, V.; KIGEL, A.; EISEN, M.S.; and BERGER, S. Synthesis and characterization of PbSe quantum wires, multipods, quantum rods, and cubes. *Nano Lett.*, 3(6), 2003: 857–862.

[211] MOKARI, T.; ZHANG, M.; and YANG, P. Shape, size, and assembly control of PbTe nanocrystals. *J. Am. Chem. Soc*, 129(32), 2007: 9864–9865.

[212] GUPTA, S.; KERSHAW, S.V.; and ROGACH, A.L. 25th anniversary article: Ion exchange in colloidal nanocrystals. *Adv. Mater.*, 25(48), 2013: 6923–6944.

[213] Lv, W.; He, W.; Wang, X.; Niu, Y.; Cao, H.; Dickerson, J.H.; and Wang, Z. Understanding the oriented-attachment growth of nanocrystals from an energy point of view: A review. *Nanoscale*, 6, 2014: 2531–2547.

[214] Schliehe, C.; Juarez, B.H.; Pelletier, M.; Jander, S.; Greshnykh, D.; Nagel, M.; Meyer, A.; Foerster, S.; Kornowski, A.; Klinke, C.; and Weller, H. Ultrathin PbS sheets by two-dimensional oriented attachment. *Science*, 329, 2010: 550–553.

[215] Luther, J.M.; Zheng, H.; Sadtler, B.; and Alivisatos, A.P. Synthesis of PbS nanorods and other ionic nanocrystals of complex morphology by sequential cation exchange reactions. *J. Am. Chem. Soc*, 131, 2009: 16851–16857.

[216] Saruyama, M.; So, Y.G.; Kimoto, K.; Taguchi, S.; Kanemitsu, Y.; and Teranishi, T. Spontaneous formation of wurzite-CdS/zinc blende-CdTe heterodimers through a partial anion exchange reaction. *J. Am. Chem. Soc*, 133(44), 2011: 17598–17601.

[217] Kim, H. and Kaviany, M. Effect of thermal disorder on high figure of merit in PbTe. *Phys. Rev. B*, 86, 2012: 045213.

[218] Sarasamak, K.; Kulkarni, A.J.; Zhou, M.; and Limpijumnong, S. Stability of wurtzite, unbuckled wurtzite, and rocksalt phases of SiC, GaN, InN, ZnO, and CdSe under loading of different triaxialities. *Phys. Rev. B*, 77, 2008: 024104.

[219] Fang, C.; van Huis, M.A.; Vanmaekelbergh, D.; and Zandbergen, H.W. Energetics of polar and nonpolar facets of PbSe nanocrystals from theory and experiment. *ACS Nano*, 4(1), 2010: 211–218.

[220] Wright, K. and Gale, J.D. Interatomic potentials for the simulation of the zinc-blende and wurtzite forms of zns and CdS: Bulk structure, properties, and phase stability. *Phys. Rev. B*, 70, 2004: 035211.

[221] Dick, B.G. and Overhauser, A.W. Theory of the dielectric constants of alkali halide crystals. *Phys. Rev.*, 112, 1958: 90–103.

[222] Phillips, J.C. Covalent bond in crystals. i. elements of a structural theory. *Phys. Rev.*, 166, 1968: 832–838.

[223] CATLOW, C.R.A. and STONEHAM, A.M. Ionicity in solids. *J. Phys. C*, 16, 1983: 4321.

[224] VAN BEEST, B.W.H.; KRAMER, G.J.; and VAN SANTEN, R.A. Force fields for silicas and aluminophosphates based on ab initio calculations. *Phys. Rev. Lett.*, 64, 1990: 1955–1958.

[225] BINKS, D.J. and GRIMES, R.W. Incorporation of monovalent ions in ZnO and their influence on varistor degradation. *J. Am. Ceram. Soc.*, 76(9), 1993: 2370–2372.

[226] SANDERS, M.J.; LESLIE, M.; and CATLOW, C.R.A. Interatomic potentials for SiO_2. *J. Chem. Soc., Chem. Commun.*, 1984: 1271–1273.

[227] ZHOU, X.W.; WARD, D.K.; MARTIN, J.E.; VAN SWOL, F.B.; CRUZ-CAMPA, J.L.; and ZUBIA, D. Stillinger-weber potential for the II-VI elements Zn-Cd-Hg-S-Se-Te. *Phys. Rev. B*, 88, 2013: 085309.

[228] WARD, D.K.; ZHOU, X.W.; WONG, B.M.; DOTY, F.P.; and ZIMMERMAN, J.A. Analytical bond-order potential for the Cd-Zn-Te ternary system. *Phys. Rev. B*, 86, 2012: 245203.

[229] GRÜNWALD, M.; LUTKER, K.; ALIVISATOS, A.P.; RABANI, E.; and GEISSLER, P.L. Metastability in pressure-induced structural transformations of CdSe/ZnS core/shell nanocrystals. *Nano Lett.*, 13, 2012: 1367–1372.

[230] QIU, B.; BAO, H.; ZHANG, G.; WU, Y.; and RUAN, X. Molecular dynamics simulations of lattice thermal conductivity and spectral phonon mean free path of PbTe: Bulk and nanostructures. *Comput. Mater. Sci.*, 53(1), 2012: 278–285.

[231] MARTYNA, G.J.; TOBIAS, D.J.; and KLEIN, M.L. Constant pressure molecular dynamics algorithms. *J. Chem. Phys.*, 101, 1994: 4177–4189.

[232] ARESTI, A.; GARBATO, L.; and RUCCI, A. Some cohesive energy features of tetrahedral semiconductors. *J. Phys. Chem. Solid*, 45(3), 1984: 361–365.

[233] SHIMOJO, F.; KODIYALAM, S.; EBBSJÖ, I.; KALIA, R.K.; NAKANO, A.; and VASHISHTA, P. Atomistic mechanisms for wurtzite-to-rocksalt structural transformation in cadmium selenide under pressure. *Phys. Rev. B*, 70, 2004: 184111.

[234] Li, Y.; Zhang, X.; Li, H.; Li, X.; Lin, C.; Xiao, W.; and Liu, J. High pressure-induced phase transitions in CdS up to 1 Mbar. *J. Appl. Phys.*, 113(8), 2013: 083509.

[235] Li, Y.; Lin, C.; Li, G.; Xu, J.; Li, X.; and Liu, J. Structure determination of the high-pressure phase of CdSe. *J. Appl. Phys.*, 115(22), 2014: 223507.

[236] Spagnoli, D. and Gale, J.D. Atomistic theory and simulation of the morphology and structure of ionic nanoparticles. *Nanoscale*, 4, 2012: 1051–1067.

[237] Chattopadhyay, T.; von Schnering, H.G.; Grosshans, W.A.; and Holzapfel, W.B. High pressure x-ray diffraction study on the structural phase transitions in PbS, PbSe and PbTe with synchrotron radiation. *Physica B+C*, 139-140, 1986: 356–360.

[238] Zapol, P.; Pandey, R.; and Gale, J.D. An interatomic potential study of the properties of gallium nitride. *J. Phys.: Condens. Matter*, 9, 1997: 9517.

[239] Ahuja, R. High pressure structural phase transitions in IV-VI semiconductors. *Phys. Status Solidi B*, 235(2), 2003: 341–347.

[240] Ovsyannikov, S.V.; Shchennikov, V.V.; Manakov, A.Y.; Likhacheva, A.Y.; Ponosov, Y.S.; Mogilenskikh, V.E.; Vokhmyanin, A.P.; Ancharov, A.I.; and Skipetrov, E.P. Unusual b1-b2 transition in PbSe under high pressure: Evidence for two intermediate phases; transport, structural, and optical properties. *Phys. Status Solidi B*, 246(3), 2009: 615–621.

[241] Debernardi, A.; Pyka, N.M.; Göbel, A.; Ruf, T.; Lauck, R.; Kramp, S.; and Cardona, M. Lattice dynamics of wurtzite CdS: Neutron scattering and ab-initio calculations. *Solid State Commun.*, 103(5), 1997: 297–301.

[242] Mohr, M. and Thomsen, C. Phonons in bulk CdSe and CdSe nanowires. *Nanotechnology*, 20, 2009: 115707.

[243] Deligoz, E.; Colakoglu, K.; and Ciftci, Y. Elastic, electronic, and lattice dynamical properties of CdS, CdSe, and CdTe. *Physica B*, 373(1), 2006: 124–130.

[244] KILIAN, O.; ALLAN, G.; and WIRTZ, L. Near kohn anomalies in the phonon dispersion relations of lead chalcogenides. *Phys. Rev. B*, 80, 2009: 245208.

[245] WIDULLE, F.; KRAMP, S.; PYKA, N.M.; GÖBEL, A.; RUF, T.; DEBERNARDI, A.; LAUCK, R.; and CARDONA, M. The phonon dispersion of wurtzite CdSe. *Physica B*, 263–264, 1999: 448–451.

[246] ELCOMBE, M.M. The crystal dynamics of lead sulphide. *Proc. R. Soc. A*, 300, 1967: 210–217.

[247] HOTJE, U.; ROSE, C.; and BINNEWIES, M. Lattice constants and molar volume in the system zns, ZnSe, CdS, CdSe. *Solid State Sci.*, 5(9), 2003: 1259–1262.

[248] LIU, H. and CHANG, L.L.Y. Phase relations in the system PbS-PbSe-PbTe. *Mineral. Mag.*, 58, 1994: 567–578.

[249] BARNARD, A.S. and XU, H. First principles and thermodynamic modeling of CdS surfaces and nanorods. *J. Phys. Chem. C*, 111(49), 2007: 18112–18117.

[250] MANNA, L.; WANG, L.; CINGOLANI, R.; and ALIVISATOS, A.P. First-principles modeling of unpassivated and surfactant-passivated bulk facets of wurtzite CdSe: A model system for studying the anisotropic growth of CdSe nanocrystals. *J. Phys. Chem. B*, 109(13), 2005: 6183–6192.

[251] ZHANG, L.; SONG, Q.; and ZHANG, S.B. Exceptionally strong hydrogen bonds affect the surface energy of colloidal nanocrystals: Methylamine and water adsorption on PbS. *Phys. Rev. Lett.*, 104, 2010: 116101.

[252] CSIK, I.; RUSSO, S.P.; and MULVANEY, P. Density functional study of non-polar surfaces of wurtzite CdSe. *Chem. Phys. Lett.*, 414(4-6), 2005: 322–325.

[253] WEI, S.H. and ZHANG, S.B. Structure stability and carrier localization in CdX (X=S,Se,Te) semiconductors. *Phys. Rev. B*, 62, 2000: 6944–6947.

[254] LAWRENCE, M.F.; DU, N.; PHILIPPE, R.; and DODELET, J.P. Preferential growth of the sphalerite or wurtzite type structure of CdSe thin films by the gas-solid process. *J. Cryst. Growth*, 84(1), 1987: 133–144.

[255] de Mello Donegá, C.; Bode, M.; and Meijerink, A. Size- and temperature-dependence of exciton lifetimes in CdSe quantum dots. *Phys. Rev. B*, 74, 2006: 085320.

[256] Shieh, F.; Saunders, A.E.; and Korgel, B.A. General shape control of colloidal CdS, CdSe, CdTe quantum rods and quantum rod heterostructures. *J. Phys. Chem. B*, 109(18), 2005: 8538–8542.

[257] Kumar, S. and Nann, T. Shape control of II–VI semiconductor nanomaterials. *Small*, 2(3), 2006: 316–329.

[258] de Mello Donegá, C. Synthesis and properties of colloidal heteronanocrystals. *Chem. Soc. Rev.*, 40, 2011: 1512–1546.

[259] Manna, L.; Milliron, D.J.; Meisel, A.; Scher, E.C.; and Alivisatos, A.P. Controlled growth of tetrapod-branched inorganic nanocrystals. *Nat. Mater.*, 2, 2003: 382–385.

[260] Asokan, S.; Krueger, K.M.; Colvin, V.L.; and Wong, M.S. Shape-controlled synthesis of CdSe tetrapods using cationic surfactant ligands. *Small*, 3(7), 2007: 1164–1169.

[261] Xu, H.; Liang, Y.; Liu, Z.; Zhang, X.; and Hark, S. Synthesis and optical properties of tetrapod-like ZnSSe alloy nanostructures. *Adv. Mater.*, 20(17), 2008: 3294–3297.

[262] Fiore, A.; Mastria, R.; Lupo, M.G.; Lanzani, G.; Giannini, C.; Carlino, E.; Morello, G.; De Giorgi, M.; Li, Y.; Cingolani, R.; and Manna, L. Tetrapod-shaped colloidal nanocrystals of II–VI semiconductors prepared by seeded growth. *J. Am. Chem. Soc.*, 131(6), 2009: 2274–2282.

[263] He, X. and Gao, L. Morphology and phase evolution of hierarchical architectures of cadmium sulfide. *J. Phys. Chem. C*, 113(25), 2009: 10981–10989.

[264] Cao, X.; Zhao, C.; Lan, X.; Yao, D.; and Shen, W. Rapid phosphine-free growth of diverse CdSe multipods via microwave irradiation route. *J. Alloy. Compd.*, 474(1-2), 2009: 61–67.

[265] Bashouti, M. and Lifshitz, E. PbS sub-micrometer structures with anisotropic shape: Ribbons, wires, octapods, and hollowed cubes. *Inorg. Chem.*, 47(2), 2008: 678–682.

[266] WANG, X.; XI, G.; LIU, Y.; and QIAN, Y. Controllable synthesis of PbSe nanostructures and growth mechanisms. *Cryst. Growth Des.*, 8(4), 2008: 1406–1411.

[267] PUZDER, A.; WILLIAMSON, A.J.; GYGI, F.; and GALLI, G. Self-healing of CdSe nanocrystals: First-principles calculations. *Phys. Rev. Lett.*, 92, 2004: 217401.

[268] TAN, J.J.; CHENG, Y.; ZHU, W.J.; and GOU, Q.Q. Elastic and thermodynamic properties of CdSe from first-principles calculations. *Commun. Theor. Phys.*, 50, 2008: 220.

[269] WANG, Y.R. and DUKE, C.B. Cleavage faces of wurtzite CdS and CdSe: Surface relaxation and electronic structure. *Phys. Rev. B*, 37, 1988: 6417–6424.

[270] SCHAPOTSCHNIKOW, P.; HOMMERSOM, B.; and VLUGT, T.J.H. Adsorption and binding of ligands to CdSe nanocrystals. *J. Phys. Chem. C*, 113(29), 2009: 12690–12698.

[271] YE, X.; SUN, D.Y.; and GONG, X.G. Pressure-induced structural transformation of CdSe nanocrystals studied with molecular dynamics. *Phys. Rev. B*, 77, 2008: 094108.

[272] GRÜNWALD, M. and DELLAGO, C. Transition state analysis of solid-solid transformations in nanocrystals. *J. Chem. Phys.*, 131(16), 2009: 164116.

[273] MEKIS, I.; TALAPIN, D.V.; KORNOWSKI, A.; HAASE, M.; and WELLER, H. One-pot synthesis of highly luminescent CdSe/CdS core/shell nanocrystals via organometallic and greener? chemical approaches. *J. Phys. Chem. B*, 107(30), 2003: 7454–7462.

[274] MORGAN, B.J. and MADDEN, P.A. A molecular dynamics study of structural relaxation in tetrahedrally coordinated nanocrystals. *Phys. Chem. Chem. Phys.*, 9, 2007: 2355–2361.

[275] HAMAD, S.; RICHARD, C.; and CATLOW, A. Computational study of the relative stabilities of ZnS clusters, for sizes between 1 and 4 nm. *J. Cryst. Growth*, 294(1), 2006: 2–8.

[276] Steinhardt, P.J.; Nelson, D.R.; and Ronchetti, M. Bond-orientational order in liquids and glasses. *Phys. Rev. B*, 28, 1983: 784–805.

[277] Moroni, D.; ten Wolde, P.R.; and Bolhuis, P.G. Interplay between structure and size in a critical crystal nucleus. *Phys. Rev. Lett.*, 94, 2005: 235703.

[278] Coasne, B.; Jain, S.K.; Naamar, L.; and Gubbins, K.E. Freezing of argon in ordered and disordered porous carbon. *Phys. Rev. B*, 76, 2007: 085416.

[279] Mohamed, M.B.; Tonti, D.; Al-Salman, A.; Chemseddine, A.; and Chergui, M. Synthesis of high quality zinc blende CdSe nanocrystals. *J. Phys. Chem. B*, 109(21), 2005: 10533–10537.

[280] Li, H.; Zanella, M.; Genovese, A.; Povia, M.; Falqui, A.; Giannini, C.; and Manna, L. Sequential cation exchange in nanocrystals: Preservation of crystal phase and formation of metastable phases. *Nano Lett.*, 11, 2011: 4964–4970.

[281] Bals, S.; Casavola, M.; van Huis, M.A.; Van Aert, S.; Batenburg, K.J.; Van Tendeloo, G.; and Vanmaekelbergh, D. Three-dimensional atomic imaging of colloidal core-shell nanocrystals. *Nano Lett.*, 11, 2011: 3420–3424.

[282] Grodzińska, D.; Pietra, F.; van Huis, M.A.; Vanmaekelbergh, D.; and de Mello Donegá, C. Thermally induced atomic reconstruction of PbSe/CdSe core/shell quantum dots into PbSe/CdSe bi-hemisphere hetero-nanocrystals. *J. Mater. Chem.*, 21, 2011: 11556–11565.

[283] Zhang, Y.; Dai, Q.; Li, X.; Cui, Q.; Gu, Z.; Zou, B.; Wang, Y.; and William, W.Y. Formation of PbSe/CdSe core/shell nanocrystals for stable near-infrared high photoluminescence emission. *Nanoscale Research Lett.*, 5, 2010: 1279–1283.

[284] Overgaag, K.; Evers, W.; de Nijs, B.; Koole, R.; Meeldijk, J.; and Vanmaekelbergh, D. Binary superlattices of PbSe and CdSe nanocrystals. *J. Am. Chem. Soc*, 130, 2008: 7833–7835.

[285] GRODZIŃSKA, D.; EVERS, W.H.; DORLAND, R.; VAN RIJSSEL, J.; VAN HUIS, M.A.; MEIJERINK, A.; DE MELLO DONEGÁ, C.; and VANMAEKELBERGH, D. Two-fold emission from the S-shell of PbSe/CdSe core/shell quantum dots. *Small*, 7, 2011: 3493–3501.

[286] VAN HUIS, M.A.; FIGUEROLA, A.; FANG, C.; BÉCHÉ, A.; ZANDBERGEN, H.W.; and MANNA, L. Chemical transformation of Au-tipped CdS nanorods into AuS/Cd core/shell particles by electron beam irradiation. *Nano Lett.*, 11, 2011: 4555–4561.

[287] FIGUEROLA, A.; HUIS, M.V.; ZANELLA, M.; GENOVESE, A.; MARRAS, S.; FALQUI, A.; ZANDBERGEN, H.W.; CINGOLANI, R.; and MANNA, L. Epitaxial CdSe-Au nanocrystal heterostructures by thermal annealing. *Nano Lett.*, 10, 2010: 3028–3036.

[288] DE TRIZIO, L.; DE DONATO, F.; CASU, A.; GENOVESE, A.; FALQUI, A.; POVIA, M.; and MANNA, L. Colloidal CdSe/Cu_3P/CdSe nanocrystal heterostructures and their evolution upon thermal annealing. *ACS nano*, 7, 2013: 3997–4005.

[289] YALCIN, A.O.; DE NIJS, B.; FAN, Z.; TICHELAAR, F.D.; VANMAEKELBERGH, D.; VAN BLAADEREN, A.; VLUGT, T.J.; VAN HUIS, M.A.; and ZANDBERGEN, H.W. Core–shell reconfiguration through thermal annealing in $Fe_xO/CoFe_2O_4$ ordered 2D nanocrystal arrays. *Nanotechnology*, 25, 2014: 055601.

[290] WAGNER, R.S. and ELLIS, W.C. Vapor-liquid-solid mechanism of single crystal growth. *Appl. Phys. Lett.*, 1964: 89–90.

[291] GUDIKSEN, M.S.; LAUHON, L.J.; WANG, J.; SMITH, D.C.; and LIEBER, C.M. Growth of nanowire superlattice structures for nanoscale photonics and electronics. *Nature*, 415, 2002: 617–620.

[292] WANG, H.; ZEPEDA-RUIZ, L.A.; GILMER, G.H.; and UPMANYU, M. Atomistics of vapour–liquid–solid nanowire growth. *Nature Commun.*, 4, 2013: 1956.

[293] PERSSON, A.I.; LARSSON, M.W.; STENSTRÖM, S.; OHLSSON, B.J.; SAMUELSON, L.; and WALLENBERG, L.R. Solid-phase diffusion mechanism for GaAs nanowire growth. *Nature Mater.*, 3, 2004: 677–681.

[294] Campos, L.C.; Tonezzer, M.; Ferlauto, A.S.; Grillo, V.; Magalhães-Paniago, R.; Oliveira, S.; Ladeira, L.O.; and Lacerda, R.G. Vapor–solid–solid growth mechanism driven by epitaxial match between solid auzn alloy catalyst particles and ZnO nanowires at low temperatures. *Adv. Mater.*, 20, 2008: 1499–1504.

[295] Kresse, G. and Joubert, D. From ultrasoft pseudopotentials to the projector augmented-wave method. *Phys. Rev. B*, 59, 1999: 1758.

[296] van Huis, M.A.; Kunneman, L.T.; Overgaag, K.; Xu, Q.; Pandraud, G.; Zandbergen, H.W.; and Vanmaekelbergh, D. Low–temperature nanocrystal unification through rotations and relaxations probed by in situ transmission electron microscopy. *Nano Lett.*, 8, 2008: 3959–3963.

[297] Moreels, I.; Lambert, K.; De Muynck, D.; Vanhaecke, F.; Poelman, D.; Martins, J.C.; Allan, G.; and Hens, Z. Composition and size-dependent extinction coefficient of colloidal PbSe quantum dots. *Chem. Mater.*, 19, 2007: 6101–6106.

[298] Moreels, I.; Fritzinger, B.; Martins, J.C.; and Hens, Z. Surface chemistry of colloidal PbSe nanocrystals. *J. Am. Chem. Soc*, 130, 2008: 15081–15086.

[299] Petkov, V.; Moreels, I.; Hens, Z.; and Ren, Y. PbSe quantum dots: Finite, off-stoichiometric, and structurally distorted. *Phys. Rev. B*, 81, 2010: 241304.

[300] Zhang, B.; Jung, Y.; Chung, H.S.; Vugt, L.V.; and Agarwal, R. Nanowire transformation by size-dependent cation exchange reactions. *Nano Lett.*, 10, 2009: 149–155.

[301] Wark, S.E.; Hsia, C.H.; and Son, D.H. Effects of ion solvation and volume change of reaction on the equilibrium and morphology in cation-exchange reaction of nanocrystals. *J. Am. Chem. Soc*, 130, 2008: 9550–9555.

[302] Justo, Y.; Sagar, L.K.; Flamee, S.; Zhao, Q.; Vantomme, A.; and Hens, Z. Less is more. cation exchange and the chemistry of the nanocrystal surface. *ACS Nano.*, 8, 2014: 7948–7957.

[303] Plimpton, S. Fast parallel algorithms for short-range molecular dynamics. *J. Comput. Phys.*, 117, 1995: 1–19.

[304] DARDEN, T.; YORK, D.; and PEDERSEN, L. Particle mesh ewald: An Nlog(N) method for Ewald sums in large systems. *J. Chem. Phys.*, 98, 1993: 10089–10092.

[305] LECHNER, R.T.; FRITZ-POPOVSKI, G.; YAREMA, M.; HEISS, W.; HOELL, A.; SCHUÜLLI, T.U.; PRIMETZHOFER, D.; EIBELHUBER, M.; and PARIS, O. Crystal phase transitions in the shell of PbS/CdS core/shell nanocrystals influences photoluminescence intensity. *Chem. Mater.*, 26, 2014: 5914–5922.

[306] ZHOU, H.S.; HONMA, I.; KOMIYAMA, H.; and HAUS, J.W. Coated semiconductor nanoparticles; the CdS/PbS system's synthesis and properties. *J. Phys. Chem.*, 97, 1993: 895–901.

[307] ZHANG, J.; GAO, J.; CHURCH, C.P.; MILLER, E.M.; LUTHER, J.M.; KLIMOV, V.I.; and BEARD, M.C. Pbse quantum dot solar cells with more than 6% efficiency fabricated in ambient atmosphere. *Nano Lett.*, 14, 2014: 6010–6015.

[308] ZHANG, J.; CHERNOMORDIK, B.D.; CRISP, R.W.; KROUPA, D.M.; LUTHER, J.M.; MILLER, E.M.; GAO, J.; and BEARD, M.C. Preparation of Cd/Pb chalcogenide heterostructured janus particles via controllable cation exchange. *ACS Nano.*, 9, 2015: 7151–7163.

[309] LEE, D.; KIM, W.D.; LEE, S.; BAE, W.K.; LEE, S.; and LEE, D.C. Direct cd-to-pb exchange of cdse nanorods into pbse/cdse axial heterojunction nanorods. *Chem. Mater.*, 27, 2015: 5295–5304.

[310] YALCIN, A.O.; GORIS, B.; VAN DIJK-MOES, R.J.A.; FAN, Z.; ERDAMAR, A.K.; TICHELAAR, F.D.; VLUGT, T.J.H.; VAN TENDELOO, G.; BALS, S.; VANMAEKELBERGH, D.; ZANDBERGEN, H.W.; and VAN HUIS, M.A. Heat-induced transformation of CdSe–CdS–ZnS core–multishell quantum dots by Zn diffusion into inner layers. *Chem. Commun.*, 51, 2015: 3320–3323.

[311] LESNYAK, V.; BRESCIA, R.; MESSINA, G.C.; and MANNA, L. Cu vacancies boost cation exchange reactions in copper selenide nanocrystals. *J. Am. Chem. Soc*, 137, 2015: 9315–9323.

[312] DE TRIZIO, L.; DE DONATO, F.; CASU, A.; GENOVESE, A.; FALQUI, A.; POVIA, M.; and MANNA, L. Colloidal CdSe/Cu_3P/CdSe nanocrystal heterostructures and their evolution upon thermal annealing. *ACS Nano*, 7, 2013: 3997–4005.

[313] White, S.L.; Smith, J.G.; Behl, M.; and Jain, P.K. Co-operativity in a nanocrystalline solid-state transition. *Nature Commun.*, 4, 2013: 2933.

[314] Ott, F.D.; Spiegel, L.L.; Norris, D.J.; and Erwin, S.C. Microscopic theory of cation exchange in CdSe nanocrystals. *Phys. Rev. Lett.*, 113, 2014: 156803.

[315] Habinshuti, J.; Capiod, P.; Nguyen, T.H.; Justo, Y.; Avila, F.J.; Asensio, M.C.; Bournel, F.; Gallet, J.J.; Vobornik, I.; Fujii, J.; Addad, A.; Lambert, K.; Nys, J.P.; Lambert, Y.; Hens, Z.; Osherov, A.; Golan, Y.; Robbe, O.; Turrell, S.; and Grandidier, B. Phase transformation of PbSe/CdSe nanocrystals from core-shell to janus structure studied by photoemission spectroscopy. *Phys. Rev. B*, 87, 2013: 184102.

[316] Li, D.; Zhang, P.; and Yan, J. Ab initio molecular dynamics study of high-pressure melting of beryllium oxide. *Sci. Rep.*, 4, 2014.

Summary

The aim of the study described in this thesis is to obtain a profound understanding of transformations in NCs at the atomic level, by performing molecular simulations for such transformations, and by comparing the simulation results with available experimental high-resolution transmission electron microscopy (HRTEM) data to validate the simulations and to reveal underlying physical mechanisms. These transformations include structural and morphological transitions and cation exchange processes in ionic nanocrystals (II-VI and IV-VI semiconductors). The main simulation method used is classical Molecular Dynamics (MD) simulation. First principles density functional theory (DFT) calculations were used to develop empirical force fields that are able to accurately reproduce phase transitions. Using these newly developed force fields, large scaled classical MD simulations were carried out and linked to HRTEM experiments. The partially charged rigid ion model (PCRIM) was chosen for the force fields. This PCRIM approach has a simple functional form with a few number of parameters and has a clear physical meaning for ionic crystals. To simulate cation exchange in colloidal NC systems at the NC/solution interface, we used a combination of all-atom force fields and a coarse-grained model.

In Chapter 2, an ab-initio based force field for ZnO is developed within the framework of the PCRIM approach. The values of the partial charges were determined by Bader charge analysis of DFT calculations on various ZnO phases. Beside Coulombic interactions, only short-ranged pairwise interatomic interactions were included. An initial guess of the parameters of the short-ranged pair potentials were first obtained by the lattice

inversion method. The parameters were further adjusted by an ab-initio potential surface fitting procedure. The new ZnO force field has a very simple functional form is able to accurately reproduce several important physical properties of ZnO materials. These physical properties include the lattice parameters and phase stability of several ZnO polymorphs, as well as the elastic constants, bulk moduli, phonon dispersion, and melting points of wurtzite ZnO. The transition pressure of the wurtzite-to-rocksalt transition calculated with the force field equals 12.3 GPa, in agreement with experimental measurements and DFT calculations. A wurtzite-to-honeycomb phase transition is predicted at an uniaxial pressure of 8.8 GPa. We found a rational and effective way to derive force fields with simple functional forms for accurate simulations of phase transitions in ionic crystals.

In Chapter 3, we developed a transferable force field for CdS-CdSe-PbS-PbSe solid systems. The selection of the force field and the fitting procedure are similar to that of the ZnO force field in Chapter 2. The challenges when developing this force field were to maintain the transferability of this force field for four materials (CdS, CdSe, PbS, and PbSe) and to describe their mixed phases. This was solved by assuming that different cations/anions have the same values of the partial charges, and that short-ranged interatomic interactions between two cations/anions are the same in different materials. For the mixed phases, DFT calculations of the mixed phases were included in both the training and validation sets. This work is the first step for further simulation studies of these II-VI and IV-VI semiconductor NCs and heteronanocrystals (HNCs).

In Chapter 4, a thermally induced morphological and structural transition of CdSe NCs was investigated using MD simulations. In MD simulations, a CdSe nanosphere with the ZB structure transforms into a tetrapod-like morphology at 800 K. In a CdSe tetrapod, four WZ legs attach to the $\{111\}$ facets of a tetrahedral ZB core. This transformation is achieved by a layer-by-layer slip of the ZB-$\{111\}$ bilayer. Simulations show that the slips are mediated by the formation of Cd vacancies on the surface of the NCs to overcome the potentially large energy barriers associated with slip. The morphology of the annealed NCs is found to be temperature- and size-dependent. An octapod-like morphology is found in NCs with a relatively large NC size and in a certain range of the heating temperature. Surprisingly, nanoscale transformations of CdSe NCs have been directly observed in HRTEM *in situ* heating experiments. Our findings provide a simple method to modify the morphology of ionic NCs and can potentially be used in the synthesis of branched NCs.

The cation exchange process of PbSe/CdSe HNCs has been investigated by HRTEM *in situ* heating experiments in combination with MD simulations and DFT calculations in Chapter 5. In the HRTEM experiments, we observed that Cd atoms in PbSe/CdSe nanodumbbells (CdSe rods with one or two PbSe tip(s)) are replaced by Pb atoms. The exchange rate depends on the heating temperature and the amount of Pb atoms present in the system. Sometimes, fully converted PbSe nanodumbells can be observed. MD simulations were performed to investigate the mechanism of this cation exchange process. It was found that the the CdSe domains near the PbSe/CdSe interfaces have significant structural disorder. These findings are in line with the experimental observation that the exchange process proceeds in a layer-by-layer fashion along the WZ-<0001>direction. We concluded that cation exchange in PbSe/CdSe HNCs is mediated by the local structural disorder which enables the formation of vacancies and accelerated the motion of cations.

In Chapter 6, a coarse-grained psuedoligand model was introduced to simulate cation exchange in PbS colloidal NCs taking into account the cation-solvent interactions. Modelling colloidal NC systems including interactions with the solvent has long been a challenge due to the large system size and long time scales. Here, we incorporated the effects of ligands and solvents into negatively charged large spherical coarse-grained psuedoligands. MD simulations combining coarse-grained and all-atom models can successfully reproduce the cation exchange process in PbS colloidal NCs. Simulations show that the exchange rate and system equilibrium can be controlled by the temperature and by changing ligands. The exchange process is directly related to vacancy formation and the high mobility of Cd ions at the PbS/CdS interface. Our simulations also predict that high-pressure conditions will be beneficial for achieving fast exchange at elevated temperatures. Our coarse-grained model can be easily extended to other systems for the computational investigation of transformations in nanostructures.

Samenvatting

Het doel van dit onderzoek is het verkrijgen van een beter inzicht in de transformaties van nanokristallen (NCs) op atomisch niveau. Hiervoor zijn moleculaire simulaties voor dergelijke transformaties uitgevoerd. Door het vergelijken van de resultaten van de simulaties met beschikbare experimentele high-resolution transmission electron microscopy (HRTEM) data is het mogelijk om de simulaties te valideren en de onderliggende fysische mechanismen te begrijpen. De transformaties van NCs omvatten structurele en morfologische transities en kation uitwisselingsprocessen in ionische nanokristallen (II-VI en IV-VI halfgeleiders). De klassieke Moleculaire Dynamica (MD) methode is hoofdzakelijk gebruikt voor de simulaties in dit onderzoek. Berekeningen gebaseerd op density functional theory (DFT) zijn gebruikt om een empirisch force field te ontwikkelen welke in staat is om fase overgangen te reproduceren. Klassieke MD simulaties met dit nieuw ontwikkelde force field zijn op grote schaal uitgevoerd en vervolgens vergeleken met HRTEM experimenten. Het partially charged rigid ion (PCRIM) model was gekozen voor de parameterizering van de force fields. De PCRIM benadering heeft een eenvoudige functionele vorm en een gering aantal parameters. De parameters hebben een duidelijke fysische betekenis voor ionische kristallen. Om de kation uitwisseling in collodale NC systemen aan het NC/oplosmiddel oppervlak te simuleren hebben we een combinatie van een all-atom force field en een coarsed-grained model gebruikt.

In hoofdstuk 2 is een op ab-initio gebaseerd force fieldvoor ZnO ontwikkeld. De waardes van de atomaire ladingen zijn verkregen door een Bader lading analyse van DFT berekeningen van verschillende ZnO fases. Naast de electrostatische interacties werden uitsluitend de short-ranged paarsgewijze interatomische interacties meegenomen. Een initile inschatting van de parameters van de short-ranged paar potentialen werd verkregen met behulp van de lattice inversion methode. De parameters zijn verder gecorrigeerd door te fitten aan een ab-initio potentiaal oppervlakken. Het nieuwe ZnO force field heeft een simpele functionele vorm en is instaat om belangrijke fysische eigenschappen van ZnO materialen accuraat te reproduceren. Deze fysische eigenschappen zijn de lattice inversie parameters en de fase stabiliteit van verschillende ZnO polymorfen, eveneens als de elastische constanten, bulk moduli, phonon dispersie en het smeltpunt van wurtzite ZnO. De transitie druk van de wurtzite-to-rocksalt transitie berekend met het force field is gelijk aan 12.3 GPa, welke goed overeenkomt met experimentele metingen en DFT berekeningen. Een wurtzite-to-honeycomb fase transitie is voorspeld bij een druk van 8.8 GPa. Wij hebben een effectieve manier gevonden om force fields met een eenvoudige functionele vorm (die fase transities in ionische kristallen accuraat kunnen simuleren) te parameterizeren.

In hoofdstuk 3 hebben we een transferable force field voor CdS-CdSe-PbS-PbSe vaste systemen ontwikkeld. De selectie van het force field en de procedure van het fitten van de parameters is hetzelfde als die van het ZnO force field in hoofdstuk 2. De uitdaging tijdens het ontwikkelen van dit force field was om de transferability voor de vier materialen (CdS-CdSe-PbS-PbSe) te behouden en om de gemengde fases te beschrijven. Dit is ondervangen door de aanname dat de verschillende kationen/anionen dezelfde waarde voor de partile lading hebben en dat short-ranged interatomische interacties tussen twee kationen/anionen hetzelfde zijn in verschillende materialen. Voor de gemengde fases werden DFT berekeningen van zowel de oefen als de validatie set gebruikt. Dit werk is de eerste stap voor verdere simulatie studies van de II-VI en VI halfgeleider NCs en hetero nanokristallen (HNCs).

In hoofdstuk 4 is een thermisch genduceerd morfologische en structurele transitie van CdSe NCs door middel van MD simulaties onderzocht. In MD simulaties transformeert een CdSe nanosphere met een ZB structuur in een tetrapod-achtige morfologie bij 800 K. In een CdSe tetrapod zitten vier WZ benen vastgehecht aan de 111 facetten van de tetrahedral ZB kern. Deze transformatie is bereikt door een laag voor laag slip van de ZB-111 dubbellaag. Simulaties laten zien dat de slip bevordert wordt door de vorming van Cd vacancies op het oppervlak van de NCs om potentiele grote energie barrires geassocieerd met de slip te overbruggen. De morfologie van de annealed NCs zijn temperatuur en grootte afhankelijk. Een octapod-achtige morfologie is gevonden in NCs met een relatief grote NC formaat en voor bepaalde verhittingstemperaturen. Het is verrassend dat transformaties van CdSe NCs op nanoschaal in HRTEM in situ verhittingsexperimenten zijn geobserveerd. Onze bevindingen verschaffen een simpele methode om de morfologie van ionische NCs te modificeren. De methode kan eventueel gebruikt worden voor de synthese van vertakte NCs

Het kation uitwisselingsproces van PbSe/CdSe HNCs is onderzocht door middel van HRTEM in situ verhittingsexperimenten in combinatie met MD simulaties en DFT berekeningen (hoofdstuk 5). In het HRTEM experiment hebben we geobserveerd dat Cd atomen in PbSe/CdSe nanodumbells (CdSe staven met een of twee PbSe punt(en)) zijn vervangen door Pb atomen. De mate van uitwisseling hangt af van de verhittingstemperatuur en de hoeveelheid Pb atomen aanwezig in het systeem. In sommige gevallen kunnen volledig omgezette PbSe nanodumbells worden waargenomen. MD simulaties werden uitgevoerd om het mechanisme van dit kation uitwisselingsproces te onderzoeken. Er werd gevonden dat de CdSe domeinen dichtbij de PbSe/CdSe interfaces een significante structuur afwijking hebben. Deze bevindingen komen overeen met de experimentele observaties dat het uitwisselingsproces plaatsvindt op een laag-bij-laag wijze in de WZ¡0001¿ richting. Wij hebben geconcludeerd dat de kation uitwisseling in PbSe/CdSe HNCs bevordert wordt door lokale structuur afwijking welke de vorming van vacancies mogelijk maakt en de beweging van kationen versnelt.

In hoofdstuk 6 is een coarse-grained pseudoligand model gentroduceerd om de kation uitwisseling in PbS collodaal NCs te simuleren, rekening houdend met de kation-oplosmiddel interacties. Modelleren van collodale NCs systemen inclusief de interacties met het oplosmiddel is een uitdaging vanwege de grootte van het systeem en lange tijdsduur van de simulaties. In onze studie hebben we de effecten van liganden en oplosmiddelen als negatief geladen bolvormig coarse-grained pseudoliganden gentegreerd. MD simulaties die coarse-grained en all-atom modellen combineren kunnen het uitwisselingsproces in PbS collodaal NCs succesvol reproduceren. Simulaties laten zien dat de uitwisselingssnelheid en het evenwicht van het systeem gecontroleerd kan worden door de temperatuur en het type liganden. Het uitwisselingsproces is direct gerelateerd aan de vorming van vacancies en de hoge bewegelijkheid van Cd ionen in de Pbs/CdS interface. Onze simulaties voorspellen eveneens dat een hoge druk bevorderlijk is voor het bereiken van snelle uitwisseling bij hoge temperaturen. Ons coarse-grained model kan gemakkelijk uitgebreid worden naar andere systemen voor het bestuderen van transformaties in nanostructuren.

Curriculum Vitae

The author was born on July 27, 1985 in Beijing, China. Since 2003, he began to study physics at Nankai University in Tianjin, China, where he received his Bachelor of Science degree in 2007 and Master of Science degree in 2011. In August 2011, the author moved to the Netherlands and started his Ph.D. project in Delft University of Technology under the supervision of Prof. Thijs J. H. Vlugt and Dr. Marijn A. van Huis. The focus of the project has been investigating transformations in nanocrystals using molecular simulation.

Publications by the Author

1. Z. Fan, L-C. Lin, W. Buijs, T.J.H. Vlugt, M.A. van Huis; Atomistic Understanding of Cation Exchange in PbS Nanocrystals Using Pseudoligands. submitted to *Nature Commun.*

2. C. Fang, X. Lu, W. Buijs, Z. Fan, E. Genceli, M.A. van Huis, G.J. Witkamp, T.J.H. Vlugt; Crystal Structure, Stability, and Electronic Properties of Hydrated Metal Sulfates $\mathrm{MSO_4(H_2O)}_n$ (M=Ni,Mg; n=6,7) and their mixed phases: A first principles study. *Chem. Eng. Sci.*, 121 (2015) 77–86.

3. A.O. Yalcin, B. Goris, R.J.A. van Dijk-Moes, Z. Fan, A.K. Erdamar, F.D. Tichelaar, T.J.H. Vlugt, G. van Tendeloo, S. Bals, D. Vanmaekelbergh, H.W. Zandbergen, M.A. van Huis; Heat-Induced Transformation of CdSe–CdS–ZnS Core–Multishell Quantum Dots by Zn Diffusion into Inner Layers. *Chem. Commun.*, 51 (2015) 3320–3323.

4. Z. Fan, R.S. Koster, S. Wang, C. Fang, A.O. Yalcin, F.D. Tichelaar, H.W. Zandbergen, M.A. van Huis, T.J.H. Vlugt; Transferable Force Field for CdS-CdSe-PbS-PbSe Solid Systems. *J. Chem. Phys.*, 141 (2014) 244503.

5. S. Wang, Z. Fan, R.S. Koster, C. Fang, M.A. van Huis, A.O. Yalcin, F.D. Tichelaar, H.W. Zandbergen, T.J.H. Vlugt; New Ab-Initio-Based Pair Potential for Accurate Simulation of Phase Transitions in ZnO. *J. Phys. Chem. C*, 118 (2014) 1150–11061.

6. A.O. Yalcin, Z. Fan, B. Goris, W.F. Li, R.S. Koster, C.M. Fang, A. van Blaaderen, M. Casavola, F.D. Tichelaar, S. Bals, G. van Tendeloo, T.J.H. Vlugt, D. Vanmaekelbergh, H.W. Zandbergen, M.A. van Huis; Atomic Resolution Monitoring of Cation Exchange in CdSe-PbSe Hetero-Nanocrystals during Epitaxial Solid-Solid-Vapor Growth. *Nano Lett.*, 14 (2014) 3661–3667.

7. A.O. Yalcin, B. de Nijs, Z. Fan, F.D. Tichelaar, D. Vanmaekelbergh, A. van Blaaderen, T.J.H. Vlugt, M.A. van Huis, H.W. Zandbergen; Core–Shell Reconfiguration through Thermal Annealing in $Fe_xO/CoFe_2O_4$ ordered 2D Nanocrystal Arrays. *Nanotechnology*, 25 (2014) 055601.

8. Z. Fan, A.O. Yalcin, F.D. Tichelaar, H.W. Zandbergen, E. Talgorn, A.J. Houtepen, T.J.H. Vlugt, M. A. van Huis; From Sphere to Multipod: Thermally Induced Transitions of CdSe Nanocrystals Studied by Molecular Dynamics Simulations. *J. Am. Chem. Soc.*, 135 (2013) 5869-5876.

Acknowledgement

My four-year Ph.D. education in Delft, the Netherlands, is a joyful and memorable journey in my life. I would like to thank some of the many people who helped and accompanied me through this journey. First, I would like to express my deep gratitude to my promoter, Prof. Thijs Vlugt, who offered me the position of the Ph.D. project and guided me through it. Besides his intelligence and broad knowledge on theoretical chemistry, I also admire him for his attractive personality and his open minds and positive attitude towards research and other wonderful traits. There are several unforgettable memories shared between us. Thijs is a very kind and down-to-earth person. On the first day I arrive in the Netherlands, Thijs drove a car himself and picked me up at the Schiphol airport. He is also very patient and willing to help. My English was awful when I just started my Ph.D.. I remembered my first paper went through more than ten iterations between me and Thijs. I am grateful that he did not give up on me due to my poor English but rather helped me to improve. He is always open to new ideas and provide helpful guidance which I benefited greatly by improving my creativity and independence on my research. Conducting research sometimes can be very difficult, but Thijs never let me get bored with science.

I would like to thank my co-promotor, Dr. Marijn van Huis. Marijn is an excellent theoretical and experimental physicist, who has exquisite skills on transmission electron microscopy experiments and solid knowledge on condensed matter physics and nanoscience. Every time I asked him questions or we discussed science, his answers and views are always very

clear and informative. His insights made me feel more confident on my research. I would like to offer my speacial thanks Dr. Anil Yalcin, Dr. Frans Tichelaar, and Prof. Henny Zandburgen from TNW for their extraordinary experimental works in our collaborative project. Many of the studies were initially inspired by Anil's interesting experimental observations and could not be done without their accurate experimental analyses.

I would like to thank my colleagues in Engineering Thermodynamics (ETh). I had an incredible time working with them. Prof. Buijs and Dr. Lin provided me with very useful discussions and many helps on my last paper during my Ph.D. work. I am also very grateful to our little Chinese community in the P&E building. Having a pleasant lunch and chat with all of them always made me very productive in the afternoon. I would also like to thank the people from Utrecht University and Shuaiwei Wang from Huanghe Institute of Science and Technology who helped me immensely with my research. I acknowledge the Foundation for Fundamental Research on Matter (FOM) for sponsoring my Ph.D. project, and the Stichting Nationale Computerfaciliteiten (National Computing Facilities Foundation, NCF) for the use of supercomputing facilities.

I am very grateful that I have made several good friends in the Netherlands, especially my dearest board game group (Hua, Yufei, Yunlong, Guanliang, and Haidong). My life in Delft would be much duller and incomplete without their companionships. I would like to extend my special thanks to Jun for designing the cover of this thesis; Tommy, Mahinder, and Dion for translating the propositions and Summary section into Dutch; and Xiaopeng for polishing the language. Last but not least, I would like to thank my dearest mother and father. Four years ago, if they have not managed to persuade me to do a Ph.D. in the Netherlands with the aim of having me as a tour guide when they were travelling in Europe, I would not have had such a wonderful four-year journey.